Elise Tajet Høigård

On-line Condition Assessment of 420 kV Terminations – design and development of PD sensors

Preliminary design of a capacitive copper mesh PD sensor and PD testing of a spherical void embedded in cable insulation

Master's thesis

◻ **NTNU**
Norwegian University of
Science and Technology

Elise Tajet Høigård

On-line Condition Assessment of 420 kV Terminations – design and development of PD sensors

Preliminary design of a capacitive copper mesh PD sensor and PD testing of a spherical void embedded in cable insulation

NTNU
Norwegian University of
Science and Technology

Preface

This thesis is the final master thesis of the 2-year master's program Energy and the Environment at the Department of Electrical power Engineering at the Norwegian University of Science and Technology (NTNU). The thesis account for 30 credits which corresponds to the workload for a semester.

The project is a part of the *SmartACT - Smart on-line health Assessment of Cable Terminations*, an ongoing innovation project for the industrial sector, and a collaboration between Statnett, Nexans Norway, SINTEF and NTNU. This thesis investigates if a high-frequency copper mesh capacitive coupler can be used to detect PD activity in high voltage cable terminations. Experiments regarding this sensor proposal have been performed by conducting frequency response analysis, sensitivity analysis and PD measurements.

I would like to thank my supervisor, associate professor Frank Mauseth at NTNU and my co-supervisor, research scientist Hans Kristian Hygen Meyer at SINTEF, for valuable help and guidance during the project and laboratory experiments. They have been creative and easily accessible yet professional.

I would also like to thank research scientist Hans Sæternes at SINTEF for guidance at the casting lab and senior research scientist Sverre Hvidsten at SINTEF for ideas for defect implementation and sensor principles. Lastly, I would like to thank the people at the electrical workshop and the service lab for help with the construction of equipment and parts related to the laboratory experiments. I am also grateful for my fellow students at the master office F452. Thank you for a fun and eventful semester.

Trondheim June 7, 2022

Elise Tajet Høigård

Abstract

Terminations are considered a weak point in the transmission grid, and utilities experience that poor termination is a major cause of cable system failures. Partial discharges caused by void formation at the intersection between the field regulating stress cone of the termination and the cable are one of the significant causes of breakdown. The SmartACT project aims to develop a novel hardware based on sensors placed inside 420 kV oil-filled terminations for on-line condition assessment to increase the security of supply. This hardware shall, among other factors, measure partial discharge activity. A PD measurement is a well-established criterion for condition assessment and often follows the conventional measuring technique as established by IEC. However, PD detection has also been investigated by employing non-conventional electrical coupling methods.

This project examines if a capacitive coupler can be constructed by screen copper mesh to measure PD activity in a HV termination. Five preliminary sensor proposals have been analysed in terms of frequency response analysis (FRA). Further, it was chosen to focus on one of the sensor proposals. This sensing method has been examined in terms of sensitivity analysis and analysis in LtSpice. This thesis also addresses how a micro-glass sphere can be utilised to create an artificial void defect with reproducible PD characteristics to test the sensitivity of the sensor proposal relevant to a defect. PDIV calculations, testing, and field simulations in Comsol have been conducted to examine the breakdown field of one micro-glass sphere cast into the cable insulation.

The results indicate that the frequency response gain of the five sensor proposals, except case 5, increases with increasing frequency. The highest gain is achieved at frequencies ranging from 10 MHZ to 100 MHz. Simulations in LtSpice indicate that C_s should be as low as possible and R_s as high as possible. The sensitivity analysis illustrate that the copper mesh sensor can measure charges down to 5 pC. The PDIV tests of the micro-glass spheres resulted in a breakdown field of the spheres equal to 5.64 kV/mm, which corresponds well to the simulated field in Comsol. During the PD sensor test of the implemented void defect, the copper mesh sensor captured 2.84% more apparent charge values than the conventional measuring technique. Meanwhile, the PDIV of the implemented micro-glass sphere was measured lower than expected, and the measured signals were not reproducible.

It is uncertain how the sensor proposals will perform at frequencies above 10^8 Hz. Changes of C_s and R_s may not be achieved without additional adjustments to the measuring circuit. A better sensitivity of the copper mesh sensor during the PD sensor test could have been achieved by utilising a bandwidth in accordance with the FRA measurements. The measured PD signals during the PD-sensor test may not stem from the micro-glass sphere. In addition, the field simulations of the stress cone may indicate that the calculated expected PDIV is lower than the actual PDIV.

The copper mesh sensor has proven adequate sensitivity based on the sensitivity analysis and the PD sensor test. Nevertheless, the measured void discharges do not stem from the implemented micro-glass sphere. The measured discharges are probably due to an unsymmetrical void in the silicone grease. Consequently, the generation of an artificial void defect is not successful. The experiments in this thesis can be used as a proof of concept of the copper mesh sensor. Several tests and experiments are necessary to obtain a full-functioning PD sensor.

Sammendrag

Termineringer er ansett som et svakt punkt i transmisjonsnettet, og industrien erfarer at dårlig terminering er en av hovedgrunnene til feil i kabelsystemer. Partielle utladninger som en konsekvens av hulromsdannelse i overgangen mellom den feltregulerende spenningskonusen til termineringen og kabelen er en av de største årsakene til havari. SmartACT-prosjektet har som mål å utvikle en ny maskinvare basert på sensorer plassert inne i 420 kV oljefylte termineringer for online tilstandsvurdering for å øke forsyningssikkerheten. Dette utstyret skal, blant annet, måle partielle utladninger (PD). PD måling er et veletablert kriterium for tilstandsvurdering og følger ofte den konvensjonelle prosedyren beskrevet av IEC. PD måling har også blitt undersøkt ved å bruke ukonvensjonelle elektriske målemetoder.

Denne oppgaven undersøker om en kapasitiv sensor kan bli konstruert av kobbernetting for å måle PD aktivitet i høyspent termineringer. Frekvensresponsen til fem preliminære sensorforslag har blitt undersøkt. Videre ble det valgt å fokusere på et av disse forslagene. For denne målemetoden har det blitt gjennomført sensitivitetsanalyse og analyser i LtSpice. Denne oppgaven tar også for seg hvordan et kunstig hulrom kan dannes av en mikroglass-sfære med reproduserbare signaler for å teste sensitiviteten til sensoren relatert til en defekt. Beregninger og testing av tennspenning, samt feltsimuleringer i Comsol har blitt utført for å undersøke sammenbrudds-feltet til sfæren.

Resultatene indikerer at forsterkningen til de fem sensorforslagene, unntatt forslag nummer 5, øker med økende frekvens. Høyest forsterkning er oppnådd på en frekvens mellom 10 MHz og 100 MHz. Simuleringer i LtSpice viser at C_s burde være så lav som mulig og R_s så høy som mulig. Kobbernettingssensoren klarer å måle ladningsverdier ned til 5 pC. Tennspenningstesten resulterte i et sammenbrudds-felt på 5.64 kV/mm, som korresponderer godt med det simulerte feltet i Comsol. Kobbernettingssensoren målte 2.84% flere utladninger enn den konvensjonelle målemetoden under PD-sensortesten. Samtidig er den målte tennspenningen til sfæren lavere enn forventet, og signalene er ikke reproduserbare.

Det er usikkert hvordan forsterkningen til sensorforslagene vil være på frekvenser over 10^8 Hz. Endringer av C_s og R_s kan være vanskelig å få til uten ytterligere endringer av målekretsen. Sensitiviteten til kobbernettingssensoren kunne vært bedre om båndbredden under PD-sensortesten var justert i henhold til resultatene i frekvensrespons analysen. Det er usikker om de målte PD signalene fra PD-sensortesten stammer fra den implementerte mikroglass sfæren. I tillegg, viser feltsimuleringer av konusen at forventet tennspenning er lavere en faktisk tennspenning.

Kobbernettingssensoren har vist tilstrekkelig følsomhet basert på sensitivitetsanalysen og PD-sensortesten. Likevel, de målte utladningene fra sensortesten stammer ikke fra den implementerte glasskulen. De målte utladningene er mest sannsynlig fra et usymmetrisk hulrom i silikonfettet. Som en konsekvens, er ikke forsøket med å lage en kunstig hulromsdefekt vellykket. Eksperimentene i denne oppgaven kan benyttes som et konseptbevis av kobbernettingssensoren. Flere tester og forsøk er nødvendig for å oppnå en fullt fungerende PD sensor.

List of Symbols

ω	Angular frequency [rad/s]
ε_0	Vacuum permittivity [8.85 pF]
ε_r	Relative permittivity
C	Capacitance [pF]
C_k	Coupling capacitor [pF]
d	Thickness [m]
E	Electric field [kV/mm]
e	Induced voltage [kV]
f	Frequency [Hz]
f_c	Center frequency [Hz]
i	Current [A]
L	Inductance [H]
l	Length [m]
M	Mutal inductance [H]
p	Pressure [bar]
q	Charge [C]
$Q_{apparent}$	Apparent charge [C]
R	Resistance [Ω]
R	Resistance [Ω]
r_i	Inner radius [mm]
r_y	Outer radius [mm]
U_i	Input voltage [kV]
U_o	Output voltage [kV]
U_{bd}	Breakdown voltage [kV]
V	Voltage [kV]
x	Length [m]
Z	Impedance [Ω]
Z_m	Measuring impedance [Ω]

List of abbreviations

AC .... Alternating Current

CPL .... External measuring impedance

DGA .... Dissolved Gas Analysis

DUT .... Device Under Test

EPDM .... Ethylene propylene diene monomor

FRA .... Frequency Response Analysis

GIS .... Gas Insulated Switch-gear

GND .... Ground

HF .... High frequency

HFCT .... High Frequency Current Transformer

HV .... High-Voltage

IEC .... International Electrotechnical Commission

MCU .... Fiber optical bus controller

MF .... Medium frequency

MPD .... Partial discharge detector

MPP .... Chargeable lithium-ion battery

PET .... Polyethylene terephthalate

PEX .... Cross-linked polyethylene

PD .... Partial discharge

PDIV .... Partial discharge inception voltage

S-parameter .... Scattering-parameters

SPICE .... Simulation Program with Integrated Circuit Emphasis

UHF .... Ultra High Frequency

VHF .... Very High Frequency

VNA .... Network Analyzer

Table of contents

List of Figures

List of Tables

1   Introduction

The transmission of power in Norway is performed by overhead transmission lines and cables. The highest voltage level in Norway is 420 kV. All cables at these levels must be terminated, and at high voltage levels, such terminations are critical[1]. Terminations are used to ensure a secure transition between, for instance, overground and underground electricity transmission. An illustration of this connection principle is shown in Figure 1.1. In Norway, it is common to use oil-filled high voltage cable terminations. The Norwegian transmission system operator (TSO) Statnett experiences that a system for condition assessment is not included in such terminations, as the component is implicit assumed maintenance-free. However, failures related to such terminations may have great impacts.
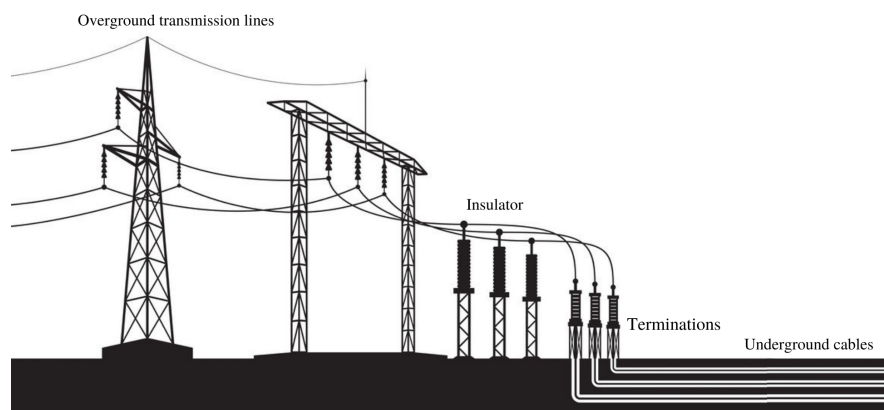
Figure 1.1: *Typical location of a termination in the high voltage grid. In the intersection between overground and underground electricity transmission a termination has to be used to ensure a secure transition from air to ground.*

A power cable network must be capable of supplying electric power without interruption. If a failure does occur, utility experience shows that poor termination and jointing are the significant causes. In contrast to the cable itself, these components have a more complex structure, sometimes with several dielectrics and high field gradients. In addition, they are installed and assembled under on-site conditions and thus exposed to a higher risk of defects and contamination. If a failure occurs, it can result in long outage periods with unacceptable societal impacts and negative economic consequences, including high not-delivered-energy costs and significant loss of industrial production[2, 3]. Summarised failure statistics show that cable and cable termination systems ranging from 220 - 500 kV have a failure rate equal to 0.050 fail./yr. 100 comp. where internal origin failures constitute the highest cause of failure[4, 5].

Most termination failures are caused by a breakdown of the insulation. A breakdown is often the consequence of gradually and cumulatively damaging effects of partial discharges (PD) on the insulation. Therefore, it is essential to monitor the condition of insulation materials through PD measurements. Partial discharges are indicative of some defects within the insulation. Thus, early detection can facilitate appropriate repair and prevent costly breakdowns[6].

A PD measurement is a well-established criterion for condition assessment and quality control of high voltage electrical insulation. The PD measuring principle often follows the conventional measuring procedure as described by IEC. As partial discharges are early indicators of incipient faults, their on-line observation is of significant interest[7].

PD detection for cables, and in particular cable joints, has been investigated by employing non-conventional electrical coupling approaches that are designed to detect the high-frequency characteristics (electromagnetic waves) of a discharge pulse[8]. These methods include inductive and capacitive coupling. Coupling methods may facilitate on-line condition assessment, which cannot be applied by the conventional PD measuring technique.

1.1   Condition assessment

A system for condition assessment on the termination can give an early warning that "something is about to happen". There are two different types of diagnostics: on-line and off-line. If the object is in operation, an on-line condition assessment is performed. For off-line condition assessment, the component must be de-energised. The overall purpose of condition assessment is to maintain a reliable power supply at a minimum cost. However, in general, assessing the condition of high voltage apparatus is a complex task. It requires detailed knowledge and statistics on the causes of failure and measurable indicators. The indicators can be of an optical, mechanical, electrical, or chemical nature depending on the functionality and construction of the individual components of the apparatus to be tested[1].

The indicators can be revealed by performing several types of diagnostic tests, which are defined by Cigre as *employment of equipment and methods on power equipment to evaluate and localise malfunctions that may cause operational faults*[9]. The assessment gives a status of the equipment and an overview of ageing mechanisms in the high voltage equipment. Ageing is defined as an irreversible deleterious change to the serviceability of insulation systems. Such changes are characterised by a failure rate that increases with time[9].

Today condition assessment is performed periodically on the most valuable high voltage equipment and on old equipment to assess the current condition. For outdoor high voltage oil-filled terminations, it is common to perform a Dissolved Gas Analysis (DGA). The key parameters in this regard are moisture content, dielectric properties, and dissolved gases. Dissolved gases can be extracted from an oil sample to reveal PD activity. The type of gases that have emerged in the oil can indicate the energy level of the PD activity[10]. However, this type of condition assessment is performed off-line and may fail to localise the source of PD inside a termination.

1.2   SmartACT

Smart on-line health Assessment of Cable Terminations, SmartACT, aims to develop a novel hardware based on sensors placed inside terminations. This innovative and non-invasive long-life sensor system for on-line condition assessment and monitoring will be developed and tested for installation inside 420 kV oil-filled cable terminations. This equipment can give a pre-warning and is expected to increase the security of energy supply by assessing temperature, humidity, pressure, and partial discharges.

The signals are to be detected inside the termination and transmitted wirelessly. In addition, the electronics inside the termination are to be supplied with wireless energy. The project is an innovation project for the industrial sector and a collaboration between Statnett, Nexans Norway, SINTEF and NTNU (Norwegian University of Science and Technology), financed by the Research Council of Norway[1, 3].

The lifetime of the sensor and electronics must be as long as the lifetime of the termination. Artificial intelligence (AI) will process and interpret the collected data. The project succeeds if the sensor system enables exposure of starting error over the whole lifetime of the termination, thereby contributing to a more robust and reliable power system in the future[1].

1.3   Scope of thesis

Based on the SmartACT project, this thesis addresses the design and development of a partial discharge sensor system that will be placed within the housing of 420 kV oil-filled terminations. The planned PD-sensor is to be placed in the same region as the stress cone in the termination, an area most prominent to failure. Several aspects when designing a PD sensor are essential:

- Design and positioning.
- Sensitivity relevant to defects such as corona and voids.
- Ability to withstand service stresses such as lightning and switching impulses.

Earlier work has been performed to investigate different types of PD measuring techniques that may be suited for on-line condition assessment of HV cable terminations[11]. That project compared a high-frequency current transformer (HFCT), an acoustic sensor and an ultra-high frequency antenna (UHF antenna) to the conventional measuring technique provided by Omicron MPD 600. The results showed that the HFCT has the best sensitivity compared to Omicron MPD 600. The acoustic measuring technique is simple to use but is limited to the placement of the sensor and reflected wave signals. The UHF measuring principle is beneficial as it provides a frequency sweep during testing, by that a suitable bandwidth for PD measurements could be achieved. However, the antenna utilised for the measurements is designed for liquid-filled transformers, which affected the results. Omicron MPD 600 (the conventional measuring principle) has the best sensitivity and is one of the best technologies existing on the market. However, this technology is not suitable for on-line PD measurements.

Based on results from previous work, it was decided to focus on the high-frequency PD measuring principles — both inductive and capacitive coupling. A capacitive sensor can be a suitable alternative to on-line PD measurements in a cable termination. To avoid changes to a high voltage termination design, it has been investigated if screen copper mesh can function as a capacitive coupler to detect partial discharge activity. Different sensor proposals have been tested using the copper mesh as an electrode. Inductive coupling may also be a suitable alternative for PD measurements. This measuring technique does not require considerable changes to the design of the termination.

This project also addresses how to replicate a void defect embedded inside the cable insulation. Materials that do not change because of PD activity can be used for this to obtain reproducible PD signals. The sensitivity of the sensor proposal relevant to this void defect has been tested. Replicating PD measurement on a test object with the presence of a void within the insulation may also facilitate a better understanding of PD characteristics.

To summarise, this thesis investigates the following:

- Capacitive copper mesh sensor for partial discharge measurement in a high voltage termination - preliminary design proposals, gain analysis, detection sensitivity and PD measurements.

- Creation of a spherical void defect, embedded in the cable insulation, with reproducible PD characteristics - procedure, implementation, field simulations and PD testing.

The thesis can mainly be divided into two main parts; a thorough theoretical part consisting of relevant literature and background knowledge and an experimental part combining the theory with actual laboratory experiments and proposals for PD sensor design. Some parts of the theory are reused from the project thesis, [11], written on the same topic. The method is divided into several subsections, which add up to the PD sensor testing. The results of the experimental part will be presented in the results section introducing the most important findings. In the discussion, the findings are evaluated and linked to the provided theory. Finally, conclusions are drawn based on the assessed results. It is expected that the reader of this project has background knowledge in electrical engineering.

2 Theory

To design and test different measuring principles for partial discharge (PD) for high voltage terminations, thorough theoretical knowledge is necessary. Firstly, the concept of cable terminations will be presented with the aim of understanding the technology and its purpose. Secondly, the mechanisms of PD will be explained by focusing on void discharges. How to measure PD will be described by introducing the conventional measuring technique and two high-frequency coupling methods. Challenges related to PD measurements will also shortly be presented. The PD part of the theory will be rounded off by explaining different methods to interpret the results with the main focus on Phase Resolved Partial Discharge Analysis (PRPDA). Lastly, theory regarding frequency response analysis will be presented based on a capacitive coupler strip.

2.1 Cable termination technology and principles

A cable termination is the physical and electrical connection of a cable end that connects to another cable or to the terminal of some voltage apparatus. In such cases, the cable conductor must be exposed to ensure a good contact surface between the conducting parts. In addition, the grounded screen of the cable must be removed a bit further to ensure sufficient creeping distance[12].

A cable with uncovered and bare conductor insulation represents a creepage configuration with extremely low partial discharge inception voltage. The creepage configuration can be explained as the shortest distance measured along an insulating interface between conducting components at high and low voltage[4]. An illustration of the equipotential lines at the end of a cable with exposed insulation is shown in Figure 2.1. As can be seen, the equipotential lines are distributed in the air surrounding the insulation but compressed around the outer semi-conductor. The field strength is high at the end of the outer semi-conductor, which is undesirable because it increases the risk of partial discharges (and eventually flashover) on the surface of the insulation.
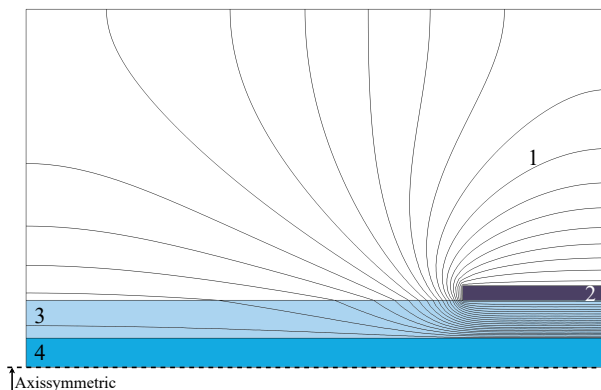
Figure 2.1: *The distribution of equipotential lines at the end of a cable with exposed cable insulation. The equipotential lines are compressed around the outer semi-conductor, increasing the risk of partial discharges. The geometry is axissymmetric. 1) Equipotential lines, 2) semi-conductor, 3) cable insulation, 4) cable conductor.*

Because of the risk of partial discharge activity, it is necessary to provide field grading at the edge of the outer conductor to increase the dielectric strength in the environment of the bare cable insulation. There are different techniques to provide this, including geometrical, capacitive, refractive, resistive, and non-linear field grading or potential grading. Mainly, geometrical field grading is applied for cable accessories[13]. Geometrical field grading can be accomplished by a stress cone, which can be explained as a semi-conductive electrode made of silicone rubber or EPDM (ethylene propylene diene monomer)[10]. Figure 2.2 illustrates a simplified stress-cone with equipotential lines.
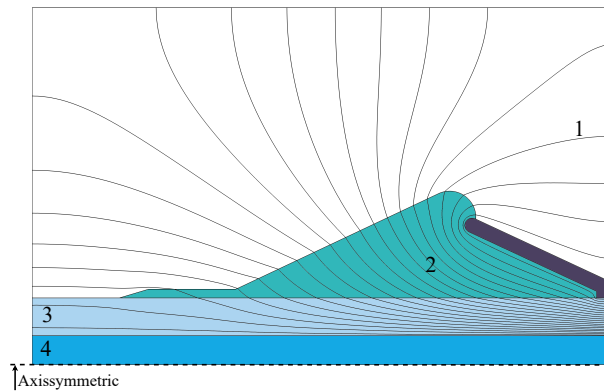
Figure 2.2: *The distribution of equipotential lines in a stress cone, commonly used for field regulation inside a high voltage termination. 1) Equipotential lines, 2) stress cone, 3) cable insulation, 4) cable conductor.*

This geometrical field grading provides a more even distribution of the equipotential lines along the boundary between the insulation and the surrounding air compared to Figure 2.1. The cone is designed to keep the field strengths within acceptable limits during operation and stress. Stress can be caused by impacts such as the field strength component along the boundary surface between the cable and the stress cone, the field strength in the stress cone insulation and the field strength in air[14].

It is common to use such a stress cone for outdoor cable terminations for high voltage XLPE cables to control the electric field. An example of the design and dimensions of a 420 kV oil-filled cable termination is given in Figure 2.3. A high voltage termination of a lower voltage rating is also shown to illustrate the physical structure inside the termination housing.
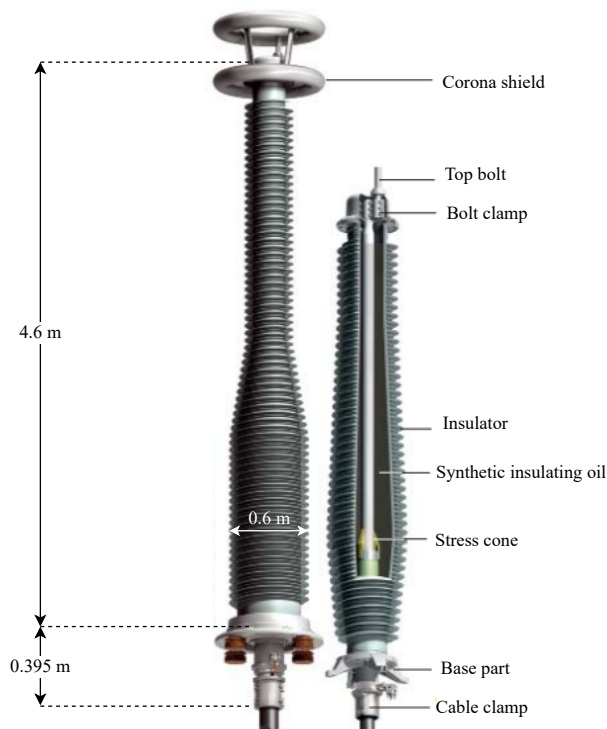
Figure 2.3: *The physical structure and dimensions of an oil-filled high voltage termination. This design is typically used for outdoor terminations in the voltage range from 84 - 420 kV[4].*

The stress cone is placed on the bare cable insulation and contacted with the outer semi-conductive layer (insulation screen) of the cable. At high voltage levels, the cone is situated in a housing insulator. The housing is typically made of porcelain or composite glass-fibre-reinforced plastic and silicone sheds, containing a high insulating medium such as SF6-gas or oil-type filling mass. The purpose of this construction is to increase the creeping current path by spreading the equipotential lines. In addition, the termination housing protects against weather, wind, and pollution. By this, unwanted discharges will be eliminated as the voltage stresses do not exceed the insulation capability at any point[13, 14].

Silicone oil as an insulating medium is widely used for fluid-filled high voltage cable terminations. Silicone oil is non-toxic and has excellent electric properties. In addition, its low flammability causes it to be safer than most other dielectric fluids. However, this insulation fluid is costly, not biodegradable, and not self-healing. During partial discharge activity, cross-linked polymeric siloxanes may form, which will damage the breakdown strength[15].

Below the termination housing, the base part often consists of a steel bottom plate. The base plate is a metal support plate to which the insulator of a cable termination is rigidly bolted. Often it is connected to earth potential either directly by a local connection or by connection to the insulation screen, metallic sheath, or shield wires of the cable[4].

The structure and type of field grading of outdoor terminations vary according to the voltage level. *Accessories for HV and EHV Extruded Cables*, [4], presents and summarises the design of various types of terminations (and joints). The design requirements are, however, common for each type of termination. These are listed below[4]:

- A high current connection from the cable conductor to an external busbar.

- Insulation to the same performance standard as the cable.

- Support provision for the cable.

- Ability to withstand thermomechanical loads and external forces such as wind, ice and busbar loading.

- A high current connection to permit the flow of short circuit current from the cable metallic sheath or shield wires which is electrically insulated from earth potential to match the insulating integrity of the cable over-sheath.

- Protection to the cable insulation and sheath against the ingress of atmospheric water and ingress of pressurised dielectric liquid or gas from adjacent metal-clad busbar trunking.

High voltage cable terminations are complex structures, and one of the special problems related to cable terminations is the possible creation of faults at the interface between the cable insulation and the electric stress-relieving material or semi-conducting cone connected to the earth screen. This is the most challenging aspect to control during installation. For instance, voids can be generated in the cable and stress cone interface due to wrong inserting position or poor surface of the semi-conducting layer. Voids in the insulation system can lead to partial discharge activity[16].

2.2 Partial discharge

According to IEC 60270, partial discharge, PD, is defined as a *localised electrical discharge that only partially bridges the insulation between conductors and which can or cannot occur adjacent to a conductor*[17]. PDs affect only a part of the insulation and can occur in all types of insulation systems. The phenomenon gradually degrades and erodes the polymeric material. Yet, the discharges do not immediately lead to breakdown as it often do not affect the short-term electric strength. However, in the case of organic insulating materials, erosion due to PD, mainly in the case of frequent and repetitive discharge impulses at AC voltage and repetitive impulse voltages, leads to usually drastically reduced service life[13].

Two factors are required to produce a PD. Firstly, the electric field must be high enough to start a local electron avalanche, typically common at a tip, such as a sharp electrode or a metallic particle, that produces field enhancement. To initiate an avalanche, a start-electron is needed, which occurs at even intervals because of background radiation. Secondly, the local electric field must be higher than the dielectric strength. For instance, in a gas-filled void in a cable, the withstand ability will be far lower than the surrounding polymer material[7].

The behaviour of discharge events is influenced by many factors, such as the electrode configuration, applied voltage type and insulation type. It is common to distinguish between external discharges and internal discharges. Discharges occurring on the outside of the power apparatus, such as corona, relate to external PD. Internal PDs are discharges occurring inside the insulation material, such as void discharges[7]. Void discharges will be closer examined in this section, including an explanation of how to calculate the partial discharge inception voltage. Lastly, other types of discharge sources, both external and internal, will be presented.

2.2.1 Void discharges

Voids in insulation materials can lead to PD activity. It can arise during casting, extrusion, impregnation or installation of a insulation system. If a cavity is present inside a dielectric insulation material, PD can lead to deterioration of the solid material at the cavity surface. This deterioration will make the cavity grow bigger and bigger, generally in the length of the applied field. A sphere-shaped cavity tends to develop as illustrated in Figure 2.4. After some time, pointy pits develop, leading to a local substantial field enhancement that can lead to treeing. The narrow treeing channels can, over time, penetrate the entire insulation leading to breakdown[12].
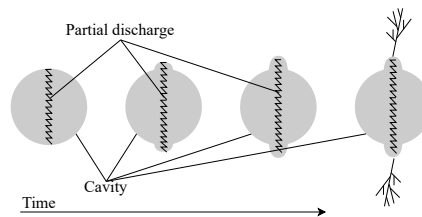
Figure 2.4: *The development of a spherical cavity as a consequence of PD activity. The spherical cavity can over time grow bigger and bigger in size in the length of the applied field. Pointy pits will develop, which may cause narrow treeing channels that can penetrate the entire insulation leading to breakdown[12].*

To explain the occurrence of discharge activity in a void, the voltage across a void encapsulated in a dielectric, U_s, can be modelled as an equivalent circuit, the so-called abc-equivalent[18]. In the equivalent, illustrated in Figure 2.5, the components are modelled as pure capacitances. C_a is the capacitance of the test object, C_b is the capacitance in series with the void, and the C_c is the capacitance of the void.
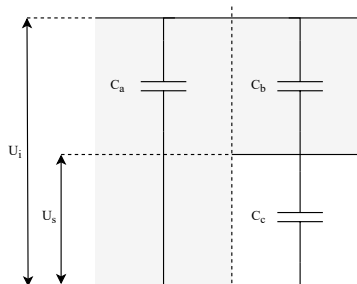
Figure 2.5: *The voltage across a void in a dielectric, U_s, can be modelled as the abc-equivalent, modelling the components of a cavity inside a dielectric as pure capacitances[18]. C_a=capacitance of the test object, C_b=capacitance in series with the void, C_c=capacitance of the void.*

The voltage over the void will follow the applied voltage, U_i, but be reduced by a factor $C_a/(C_c + C_b)$. If the voltage over the void, U_s, exceeds the withstand ability of the void, a local breakdown will occur. In other words, there is a transient current that transfers a charge from one wall of the void to the other wall. The voltage over the void becomes zero or close to zero. If the AC voltage at the terminals continues to rise, U_s will increase again from zero. As a consequence, a discharge will happen each time the voltage over the void exceeds the threshold value, U_{BD}[7].

When the voltage is reduced, a reversed voltage over the void occurs before the voltage at the terminals is reversed. This is because the surface charge in the void has changed the initial value for the voltage over the void, meaning that one always starts from zero after a discharge has happened. However, the voltage over the void will continue to follow the terminal voltage with a changing offset determined by the preceding discharge. The charge transfer and the small voltage collapses will produce small immediate transient voltage drops, ΔU, on the terminals or the electrodes. A sketch of the applied voltage, U_i, the voltage over the void, U_s, and the voltage drops at the terminal, ΔU, is given in Figure 2.6[7].
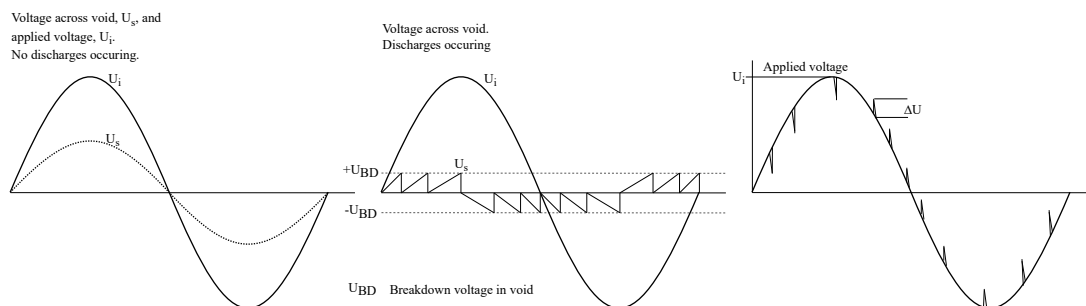
Figure 2.6: *Sketches of applied voltage, U_i, and the voltage over the void, U_s, before discharges occur and when discharges occur. If U_s exceed the withstand ability of the void, U_{BD}, a local breakdown will occur[7].*

2.2.2 Partial discharge inception voltage

Partial discharge inception voltage, PDIV, is the lowest voltage at which partial discharges occur in a circuit when the test voltage is gradually increased from a lower value. As mentioned, the abc-equivalent assumes that a discharge occurs when the voltage across the void exceeds the withstand strength of the void. In the case of a homogeneous electric field in the void, the withstand strength of the air-filled void follows the Paschen law for air, empirically given in Equation 2.1. This approximation is based on experimental data for air gaps valid in the range where pressure, p, times distance, d, is 10^{-2} to $5 \cdot 10^2$ (bar cm)[18].

$$U_{BD} = 6.72\sqrt{pd} + 24.36(pd) + \frac{0.00411}{\sqrt{pd}} \, [kV_{peak}] \tag{2.1}$$

Paschen's law describes the relationship between the breakdown voltage, U_{BD}, and the product of the pressure, p, and gap length, d, in a gas. The criteria are that the Townsend mechanisms are fulfilled, including uniform field and negligible space charges. The Paschen curve is characterised by high breakdown voltages at very low and at very high $p \cdot d$ values. At low $p \cdot d$ values, the number of molecules available for collisions decreases; hence the breakdown voltage increases. Long distances and high pressures give high $p \cdot d$ values. A long distance, d, corresponds to a reduction of the field strength, E, while the high pressure, p, reduces the free path length that is available for the acceleration of electrons[13]. The Paschen's curve for air is illustrated in Figure 2.7.
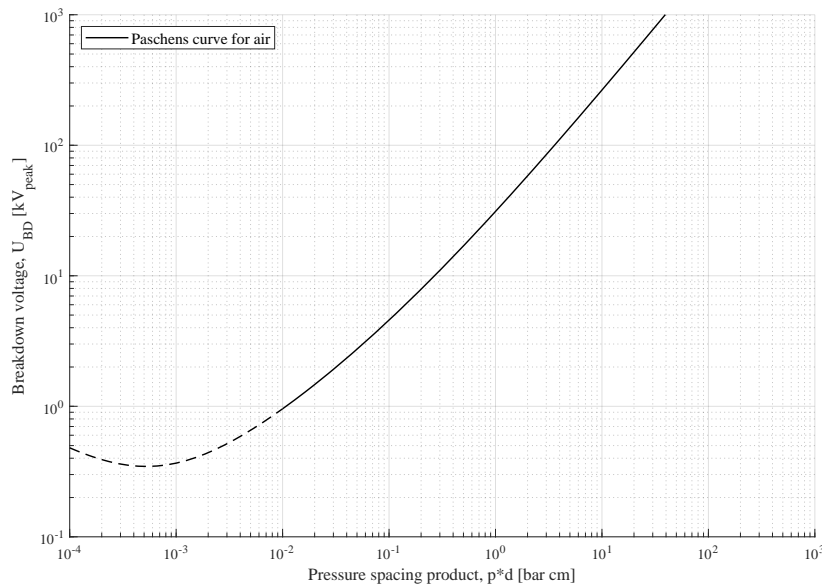
Figure 2.7: *Paschen's curve illustrates the relationship between the breakdown voltage, U_{BD}, and the product of pressure, p, and gap length, d. The empirical approximation is valid in the range where $p \cdot d$ is 10^{-2} to $5 \cdot 10^{2}$ [13], hence the graph is annotated as a dotted line for $p \cdot d < 10^{-2}$.*

On the basis of the Paschen law the PDIV of air-filled cavities can be calculated. A cavity inside a dielectric material with a relative permittivity, ε_r, can be modelled as illustrated in Figure 2.8.
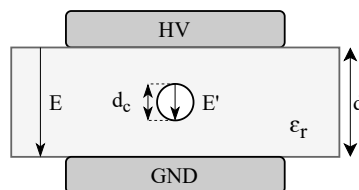
Figure 2.8: *Model of a spherical cavity in a dielectric material with a relative permittivity, ε_r, between a electrode-configuration. The maximum electric stress, E', of the cavity depends on the electric field, E, inside the dielectric material and the ε_r.*

In a spherical gas-filled cavity of a diameter much smaller than the insulation thickness, the maximum electric stress, E', can be calculated as shown in Equation 2.2. E is the electric field in the solid dielectric in the absence of cavities, and ε_r is the relative permittivity (dielectric constant) of the solid insulating material[12].

$$E' = \frac{3\epsilon_r}{1 + 2\epsilon_r} \cdot E \, [kV/mm] \tag{2.2}$$

The maximum field strength increases with increasing relative permittivity with an upper limit of 1.5 times the field strength in the surrounding solid dielectric. If the gas-filled cavity is flat and perpendicular to the electric field Equation 2.3 can be used to calculate the maximum electric field[12].

$$E' = \epsilon_r \cdot E \, [kV/mm] \tag{2.3}$$

Both the spherical and the flat cavity will have a higher electric field compared to that in the solid insulation[12]. The inception voltage, $PDIV$, can be calculated by multiplying E with the thickness of the dielectric material. This relation is given in Equation 2.4, corresponding to the voltage that needs to be applied to the dielectric material for PD inception.

$$PDIV = E \cdot d \, [kV] \tag{2.4}$$

If the cavity is situated in the insulation of a cylindrical conductor (such as a cable) the voltage of which PD activity will first occur, U_{PDIV}, can be calculated as given in Equation 2.5[12]. Both the outer radius, r_y, and the inner radius, r_i, of the cable insulation will affect the inception voltage.

$$U_{PDIV} = E \cdot r_y \cdot \ln(\frac{r_y}{r_i}) \, [kV] \tag{2.5}$$

2.2.3 Other types of discharges

The main focus of this thesis will be on void discharges. However, it is important to mention that other types of discharges can occur in high voltage insulation systems. Knowledge about other types is important, and may facilitate a more accurate interpretation of PD measurements by, for instance, defect recognition. An overview of other types of discharges, in addition to void discharges, are given in Figure 2.9.
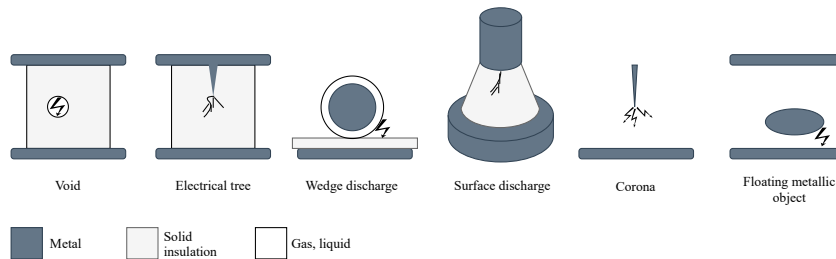
Figure 2.9: *In addition to void discharges, several discharge types can occur in high voltage insulation systems. Knowledge about the types is important, and may facilitate a more accurate interpretation of PD measurements[7].*

A defect that is closely related to void defects is electrical treeing. The trees are often filled with gas, but their shape differs from a void. Normally the trees are elongated along the field direction with sharp tips, growing from sharp metallic points in solid insulation, or from cavities. Electrical treeing may be regarded as an ageing phenomena that develops from a defect. With time they will grow in length[7].

Another type of partial discharge is wedge type discharge. In contrast to void discharges, these discharges are open towards exterior gas/fluid volumes. Such discharges lead to a replacement of the gas/liquid over time. PD tracking across the insulation, called surface discharges, may occur in cases where there is an interface parallel with the electric field between the solid insulation and gas/liquid insulation. Such discharges can be identified through irregular and intensive streamer discharges at high voltages[7].

Corona partial discharge can occur from a sharp electrode into gas or from edges and points pointing out in the insulation where the electric field is high enough to ionise the insulating medium around the electrode. Corona discharges can appear both in liquid and gaseous insulation. It is normally easily identified by Trichel pulses, which are impulses of a constant amplitude close to the AC voltage peaks at the negative point electrode. Thus, it can be distinguished whether the discharges originate from the high voltage side or on the ground side. The frequency of the impulses increases with increasing voltage[7, 13].

Electrical "floating" metallic objects can also lead to PD activity. This can be due to electrostatic screens, other conducting parts that have lost electric contact to earth, or to high voltage, where the distance is so small that full breakdown may occur towards the floating object. High energy discharges are produced in such instances because the energy stored in the capacitance between the floating part and the electrode is released at each local breakdown. Floating objects produce discharges in the steepest part of the AC voltage. In addition, impulses of constant amplitude occur at constant intervals[7].

2.3   Partial discharge measurement

There will be stored electric (potential) field energy in a dielectrically stressed insulation. At the point of a partial discharge, the locally stored energy will be released and transformed into other forms of energy which is illustrated in Figure 2.10. PD dissipate energy in the form of current pulses, heat, light, and sound. In addition, chemical changes in SF6-gas or oil-insulation may occur due to discharge energy. Since the discharges are extremely fast, typically lasting in the range of nanoseconds, electromagnetic waves will be emitted[7, 19].
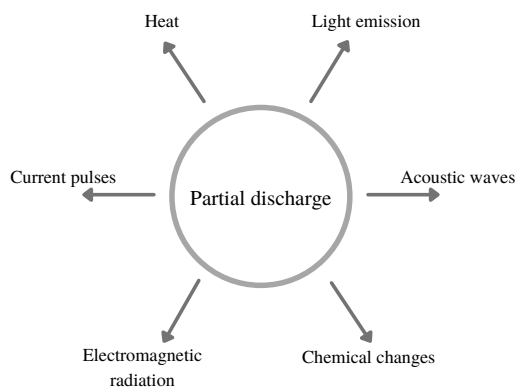
Figure 2.10: *A PD dissipates energy that at the point of discharge will be transformed to other forms of energy. These detectable signals form the basis of different technologies for PD measurement[7]*

The released local energy produces both ageing and detectable signals. These detectable signals form the basis of different technologies and methods used to measure and detect partial discharges. Consequently, PD detection can generally be categorised into electrical, acoustic, optical and chemical methods. Several techniques have been developed, and every brand of PD sensor works in various parts of the frequency spectrum. Since a typical PD pulse has a rise time of less than one nanosecond and a pulse width of several nanoseconds, implying in a frequency-domain a bandwidth of MHz, PD can be detected in a vast range of frequencies[7, 20].

The difference of the PD sensors relates to which frequency characteristics the measuring impedance has. If PD in cable terminations has a certain frequency content, starting failures can be detected using different sensor technologies or antennas sensitive to different frequencies. The frequency ranges can be split into conventional, medium/high frequency (MF/HF), very high frequency (VHF) and ultra-high frequency (UHF) according to the frequency range [20]. The different ranges are presented in Table 2.1.

Table 2.1: *Different frequency ranges used for PD detection.*

Conventional (In accordance with IEC 60270)	MF/HF	VHF	UHF
0.1 - 1 MHz	0.2 - 30 MHz	30 - 300 MHz	300 - 1000 MHz

The energy dissipation in the defect and the discharge frequency are responsible for the eroding effect of partial discharges. However, the energy can only be measured externally at the test object terminals, considering that the energy dissipation is equal to the capacitive energy stored in the cavity capacitance before the partial discharge event[13]. Further in this section, three methods to externally measure PD will be explained. This includes the conventional method described by the IEC, and two unconventional HF coupling methods. Lastly, challenges related to PD measurements will be presented, as PD are both victims of stochastic variables and noise signals.

2.3.1 Conventional detection method

Based on the abc-equivalent, the conventional PD measuring principle can be illustrated as shown in Figure 2.11. The conventional detection method utilises a coupling capacitor, C_k, and a measuring impedance (measuring shunt), Z_M, to measure partial discharge activity. The coupling capacitor is connected in parallel with the test object. By that current, i, will be supplied from the coupling capacitor into the test object each time a discharge occurs to compensate for the voltage drop, ΔU, in the test object. This means that a transient current will circulate in the capacitive measuring circuit. A measuring impedance can be inserted in the circuit to measure this current[7].
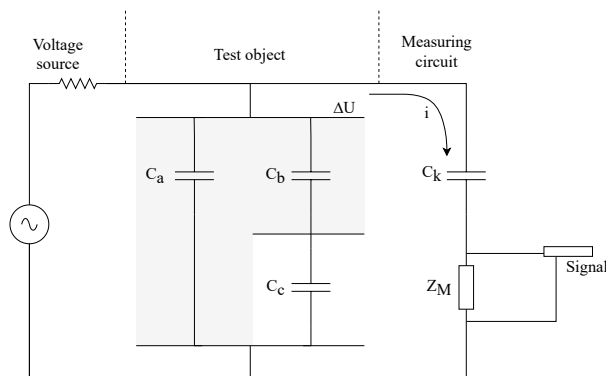
Figure 2.11: *The theoretical principle of conventional PD measurements. A coupling capacitor, C_k, will supply a current, i, each time a discharge occurs to compensate for the voltage drop, ΔU, in the test object. A measuring impedance, Z_m, can be inserted into the circuit to measure this current[7].*

Such an approach is a common coupling method when performing a PD measurement described by the IEC 60270 standard. However, it is important to notice that the measured charge is not the real charge in the PD but only the induced charge in the measuring circuit[7]. This is called the apparent charge, $Q_{apparent}$. The voltage drop on the terminals, ΔU, gives a current, i, in the external circuit that integrated up gives a charge, as shown in Equation 2.6.

$$Q_{apparent} = \int \Delta i dt = \Delta U \cdot C_b [C] \tag{2.6}$$

The magnitude of the apparent charge depends on the internal capacitances in the test object but not on the capacitances in the external circuit. The voltage drop over the test object determines the voltage over the measuring impedance. Therefore, the sensitivity (the smallest detectable signal) in a PD measurement will be reduced by increasing the capacitance of the test object and by reducing the capacitance of the

coupling capacitor. According to IEC 60270 $C_k \gg C_a$ to achieve highest sensitivity. Acceptable sensitivity is usually achieved if C_k is about one nanofarad or higher[7, 17].

A data acquisition unit can be used to detect the voltage drop across the known effective resistor of the measuring impedance in the test circuit. Since the charge is calculated by integral current over time, the correlation between the resistance, R, of the measuring impedance and the charge, q, can be calculated as given in Equation 2.7[21].

$$q = \int_{t_1}^{t_2} i(t)dt = \frac{1}{R} \int_{t_1}^{t_2} u(t)dt \, [C] \tag{2.7}$$

Modern PD measurement systems pre-amplify and digitise the input signal by an analog/digital converter, including the PD pulse. Further processing is done by digital filters, digital detection, and a computer. This process is shown in Figure 2.12. It should be noted that the resulting current will have a short duration as the voltage collapse may be regarded as instantaneous, and the circuit is purely capacitive. As a rule, the current will be small relative to the capacitive AC charging current that flows in the circuit. An important property of the measuring impedance is that it suppresses the 50 Hz voltage over the measuring impedance but detects the discharge currents. Hence, the impedance must function as a high pass filter[7].
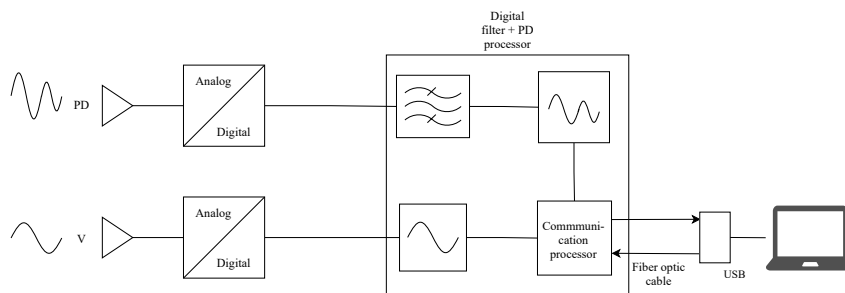
Figure 2.12: *In modern PD measurement equipment the PD signal gets amplified and digitised, before the signal is processed trough a digital filter[21].*

Such an approach is beneficial as it provides data about the test voltage needed for a phase-related partial discharge measurement. However, the conventional PD measuring technique can only be performed off-line, meaning that the equipment to be tested has to be de-energised and put out of service. In addition, it can be challenging to interpret the results from this type of PD measuring technique as PD measurements are usually made in industrial facilities where high levels of electrical noise are present[22].

2.3.2 Inductive couplers

Inductive couplers, also called High-Frequency Current Transformers, HFCT, can be utilised to couple the magnetic component of the field using the same principle as an instrument transformer. The sensor consists of an induction coil with a ferromagnetic core suitable for measurement signals such as PD. HFCT sensors can be clamped around grounding conductors of the earthing network, which is generally done for on-line PD measurements. For this operation, the sensor can be modelled as a system in which the input is the current of the PD pulses flowing through it, and the output is the induced voltage. The induced voltage is measured over the input impedance of the measuring instrument, usually at a value of 50 Ω. The sensor principles are shown in Figure 2.13[23].
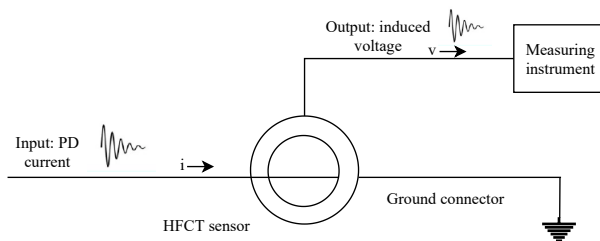
Figure 2.13: *HFCT sensor clamped around a ground conductor for PD measurement. The sensor can be modelled as a system in which the input is the current generated from a PD pulse, and the output is the induced voltage[23].*

The grounding conductor becomes a one-turn primary winding by clamping the probe around it. The secondary winding is terminated with a low-inductance sense resistor. A current pulse of high frequency flowing through the grounding conductor, or the primary winding, causes the occurrence of a time-varying magnetic field. This magnetic field passes through the secondary winding and induces a voltage across the sense resistor. This voltage is proportional to the derivative of the current in the primary conductor[24].

This concept follows Faraday's Law of induction, and the transfer function of a HFCT can be expressed as shown in Equation 2.8. The induced voltage, e, is proportional to the product of the mutual inductance, M, by the ratio between the current variation in the primary[25].

$$e = M \cdot \frac{di}{dt} \, [kV] \tag{2.8}$$

HFCT sensors are advantageous as they enable a high safety level during measurements since they do not require a direct high voltage connection. High sensitivity can be obtained independent of the distance to the PD source. Even though the propagating signal is filtered, the pulse can be measured at distances exceeding one kilometer. Previous work, [11], has shown that this measuring principle has a high sensitivity compared to the conventional measuring technique. In addition, the signal to noise ratio can be improved by analysing the obtained data in specific frequency bands. However, the sensor cannot be applied for non-insulated active parts, such as power lines or live clamps, without additional modifications. Moreover, different voltage supply phase occurred PD sources discrimination is impeded while a single HFCT grounding measurement is used[23, 26].

2.3.3 Capacitive couplers

Capacitive couplers utilise the electric component of the transient field to measure PD activity by forming a capacitive voltage divider between the capacitance of the insulation and the stray capacitance of the sensor. Only sensors suitable for transformers and GIS exist on the commercial market. However, placing a capacitive coupler inside the cable termination can be an attractive PD monitoring option. The sensor can be simple in physical structure. It can, for instance, be in the form of an aluminium or copper tape placed outside of the semi-conductor[2].

To explain the theoretical aspect of a capacitive coupler an example will be presented. This example shows a metallic foil electrode in contact with the semi-conducting screen of a cable which functions as the capacitive coupler. The principles are illustrated in Figure 2.14. Because PD can be considered as electromagnetic pulses, the coaxial structure of the cable acts as a wave-guide for the PD signal. Part of this propagated wave is coupled into the capacitive coupler giving rise to an electrical signal[27].
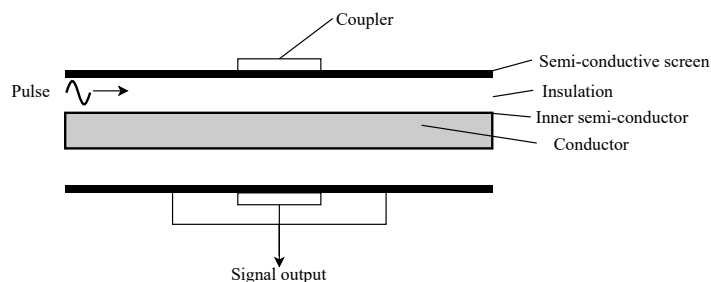
Figure 2.14: *Schematic diagram of the capacitive coupler around a cable. Propagating waves from a PD pulse is coupled into the capacitive coupler, which forms an electric signal.*

This type of capacitive coupling generally depends on the dimensions of the sensor electrode, distance to the test object and the electric field strength of the emitted waves[2]. It is essential that the monitoring equipment does not affect the ability of the main insulation and current handling ability. Furthermore, the system should be robust, have a high sensitivity and, to some extent, be immune to noise interference.

Several papers have explored the possibilities of utilising capacitive couplers for PD detection, for instance [8], [27] and [28]. These papers investigate the possibility of using the measuring principle for joints and HV cables. Common for all papers found on this topic is the utilisation of an external copper strip sensor to detect partial discharge activity, where the main focus is to analyse the effect of changing the coupler capacitance and stray capacitance. Conclusions drawn from experimental testing of these capacitive strip sensors show that PD-signals down to 3 pC can be measured.

Although the cited capacitive couplers have different implementations, the capacitive coupler is always based on a RC topology or a RLC topology for tuned sensors. As mentioned, the coupler functions as a capacitive voltage divider, which can be modelled as the circuit shown in Figure 2.15. Such a topology can be characterised as a high-pass filter. Such filters attenuate frequency components below a particular frequency(the cutoff frequency), allowing high-frequency components to pass through. The coupler capacitance, C, is dependent on the dimensions of the coupler, the semi-conducting screen and the dielectric material. R_s is the surface resistance of the semi-conducting layer, and C_s is the stray capacitance between the coupler and the ground. The output signals, which in this case is U_o, can be measured at the measuring impedance, R_m.
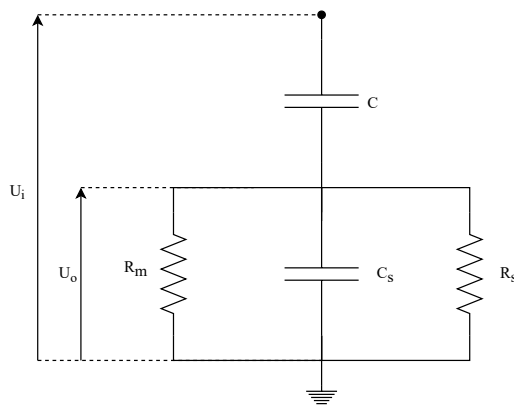
Figure 2.15: *A capacitive coupler can be modelled as a RC topology where the output signals, U_o, is measured over the measuring impedance R_m. The same principle as a capacitive voltage divider applies for this topology. U_i=input voltage, C=coupler capacitance, C_s=stray capacitance between the coupler and the ground, R_s=stray resistance of the coupler.*

Basically, there are three requirements for a high-performance capacitive coupler: high input impedance, high bandwidth and low 50 Hz signal at the measuring point. A low 50 Hz signal at the measuring point is desirable because it makes the trigger adjusting easier[8]. High sensitivity can be achieved with as large as possible resistance in the semi-conductive layer and as low as possible stray capacitance between the sensor and ground shield. High sensitivity can thus be obtained by increasing the distance between the sensor and the grounding shield. It is also beneficial with a low permittivity material between the sensor and the ground shield[27].

Capacitive couplers are beneficial as they may not cause intrusive changes to a high voltage apparatus. Cable accessories such as joints and terminations are the most likely source of PD in a cable system. A capacitive coupler can be placed inside or close to the cable accessory to detect this activity, which can be an attractive PD monitoring option.

2.3.4 Challenges related to PD measurement

The biggest challenge for all PD measurement methods is the stochastic nature of a PD phenomenon. Most of the physical quantity values obtained during a measurement are highly dependent on the nature of the PD source in addition to environmental conditions. Modifications to the environment or the PD source radically affect the final measurement results. An objective comparison of the achieved data with a representative database needs to be supported to provide an adequate measurement result interpretation. In addition, one individual relative measurement is not adequate in most cases. Therefore, interpretation may differ concerning different apparatus or environment conditions[26].

Choosing the correct bandwidth for PD detection can be a challenge. The bandwidth may influence the results of the PD measurement. IEC has set standards for bandwidths to be used for PD measurement. The center frequency, f_c, should be between 50 Hz and 1 MHz and the Δf should be between 9 kHz and 30 kHz for narrow-band measurements. For broadband measurements, the upper cut-off frequency, f_2, should be at 500 Hz, Δf should be between 100 kHz and 400 kHz, and the lower cut-off frequency, f_1, between 30 kHz and 100 kHz[17].

Noise from various sources will often be a limiting factor for obtaining good results during field measurements. Noise signals may intrude via the power grid and may be induced in the measuring circuit. Radio signals are a common source of noise. Such signals will act like a continuous noise, which may drown the discharge signals. Several techniques to filter such noise exist, often in the form of a filter that automatically adjusts itself correctly. Another source of noise signals is corona interference. A good design of the high voltage circuit may reduce this type of noise, for instance, by designing all connections with sufficiently large diameters resulting in a field strength in the high voltage circuit sufficiently low to avoid corona[7].

The use of non-conventional PD measurement techniques have introduced challenges related to calibration of the measuring circuit. The transfer function between the PD and the change in charge on the electrodes may vary by many orders of magnitude, depending on the test object and the defect geometry[29]. Therefore, calibration is an important part of PD measurements, determining the scale factor of the PD measuring system. The technical requirements of calibration, as stated by IEC 60270, is by injecting a known charge (current pulse) across the terminals of the test object in advance of the PD test[30]. However, this procedure cannot be applied for some non-conventional PD measuring techniques. In previous work, [11], a summary of some technologies which cannot be calibrated by this approach is given. This includes the UHF detection by the use of an antenna sensor, the acoustic detection method, optical detection and DGA. As a consequence a precise magnitude of the PD quantity cannot be achieved.

2.4 Partial discharge interpretation

As mentioned before, partial discharges lead to ageing and failures in the equipment. However, interpretation of the measurements and quantitative assessment of remaining service life or reduction in functionality is not straightforward based on test results. There are several approaches to assess the results. One way to assess the results is to utilise the absolute limits stated in the IEC standards. Absolute criteria are simple to relate to, but the approval criteria are often based on measurable quantities rather than a scientifically based evaluation of a failure probability. Another method is to perform an assessment based on long-term trends. This could be a good alternative to diagnostics of equipment in service following the development of the discharge level over time. A sudden shift in the increase may be a criterion to reveal that something has changed[7].

To quantitatively describe the degradation of the insulation because of PD-activity, three main measurements are commonly used[31]:

1. Discharge pulse magnitude trend, indicating the rate of dielectric deterioration.

2. Discharge pulse repetition rate, indicating the defect severity. Sustained PD activity is considered more damaging than periods of intermittent activity.

3. Discharge pulse phase angle, indicating the ignition and extinction conditions of the defect in relation to the electric field.

These three measurements can be used for defect recognition by performing an assessment based on Phase Resolved Partial Discharge Analysis (PRPDA)[7]. A PRPD measurement shows the amplitude of each discharge event at the y-axis plotted against their phase angle on the x-axis relative to the 360 degrees of an AC cycle. In addition, the pulse number of PDs can be plotted over a defined time, indicating the intensity of the captured PD activity. The obtained pattern can be interpreted as a fingerprint of the defect, and different defects will have different fingerprints[31].

Void discharges do often appear as a band in the rising slope of the voltage, and the magnitude of the discharges increases simultaneously as the voltage. The PRPD pattern is also dependent on the shape of the void. Phase symmetry of the discharges can be expected if the void is symmetrical (spherical). Corona discharges have a different appearance, often occurring as discharges of a constant amplitude at the voltage crest. PRPD patterns provide a good basis for the correlation between discharges, amplitude, and phase position. By that, it is possible to distinguish the defects present in high voltage equipment[31].

PRPD interpretation systems can support on-line condition assessment in cable terminations. In addition, defect diagnosis can be obtained by presenting a comprehensive diagnosis of detected PD activity and classification of the defect source[31]. However, it may fail to meet the complexity of the PD activity in many cases. For instance, the clearness of the partial discharge pattern can be lost due to superimposition of the events from different defects. Multiple defects are hardly kept apart without additional methods. In addition, the interpretation often reflects subjective experiences and feelings. Moreover, false conclusions can be drawn from the phase position of the impulses. Phase positions can be shifted owing to the build-up of space charges[13].

2.5 Frequency response

PD measurements are dependent on the generated energy of the PD. Therefore, PD sensors with high sensitivity (the smallest detectable signal) are preferable to cover the vast frequency ranges PD pulses can occur. Theoretically, the minimum measurable PD is 0.023 pC [29]. The conventional measuring technique and the HFCT can measure PD pulses lower than 1 pC and down to 1 pC, respectively. In addition, as mentioned, capacitive couplers have proven to be efficient down to 3 pC. However, it is important to mention that the sensitivity is difficult to quantify, as it will vary according to the type of component to be tested, type of defect and background noise.

Frequency response can be utilised to determine the sensitivity of a PD sensor. In electronics, frequency response is the quantitative measure of the output spectrum of a system or device in response to a signal. The objective of frequency analysis is to break down a complex signal into its components at various frequencies. For instance, a systems frequency response expresses how sinusoidal signals applied at the gate of the system change through the system. Both the amplitude and the phase position of the signal will be changed[32].

If end effects in the cable are neglected, and the cable is assumed to be a loss-less transmission line, the capacitive coupler as explained in section 2.3.3 can be used to explain the mathematical principles of finding the gain of the sensor in terms of frequency response analysis. A similar equivalent circuit to the one shown in Figure 2.15, is illustrated in Figure 2.16. The circuit has been extended to include the characteristic impedance, Z_0, related to the capacitance and inductance of the cable. C is the coupler capacitance, R_s is the surface resistance of the semi-conducting layer, and C_s is the stray capacitance between the coupler and the sheath. R_m is the internal impedance of the oscilloscope or the impedance of another measuring shunt[27].
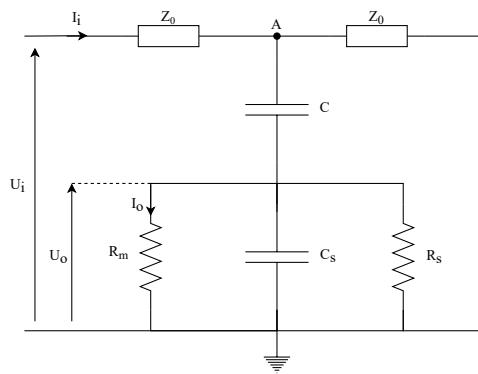
Figure 2.16: *Equivalent circuit of the coupling capacitor around the cable. Z_0 is the characteristic impedance of the cable, C is the coupler capacitance, R_s is the surface resistance of the semi-conducting layer, and C_s is the stray capacitance between the coupler and the sheath. The internal impedance of the measuring shunt is noted as R_m.*

The frequency response of the coupler can be achieved using conventional circuit analysis under steady-state sinusoidal conditions. The impedance of the capacitive coupler, Z_1, can be expressed as given in Equation 2.9.

$$Z_1 = \frac{1}{j\omega C} \tag{2.9}$$

The impedance for the parallel branch, consisting of R_m, R_s and C_s, in the equivalent can be expressed as given in Equation 2.10.

$$Z_2 = R_m || R_s || C_s \tag{2.10}$$

The voltage in point A, U_A, can thus be obtained as given in Equation 2.11.

$$U_A = \frac{2Z_L}{Z_0 + Z_L} U_i \tag{2.11}$$

The total impedance of the circuit, Z_L, in Equation 2.11 can be expressed as given in Equation 2.12.

$$Z_L = \frac{Z_0(Z_1 + Z_2)}{Z_0 + Z_1 + Z_2} \tag{2.12}$$

The output voltage across R_m can easily be found by voltage division as given in Equation 2.13.

$$U_o = \frac{Z_2}{Z_1 + Z_2} \cdot U_A \tag{2.13}$$

The gain of the sensor is found by the ratio between the output voltage to the input voltage, as given in Equation 2.14.

$$Gain = \frac{U_{out}}{U_{in}} = \frac{U_o}{U_i} \tag{2.14}$$

Based on these equations, the frequency response of the coupler can be determined, and the effect of the coupler parameters on the gain (and phase displacement) can be examined. Frequency response can also form the basis of determining the detection bandwidth of a PD measuring system. Ideally, the response of a system should be as flat as possible in the frequency area of interest. This means that peaks in the amplitude profile, or resonant peaks, are unwanted. PD measuring systems, however, are often resonant RLC-circuits and resonant peaks may not affect the output of the coupler.

3 Method

The following chapter will describe the experimental setup used in this thesis. Several experiments have been conducted, therefore, and for simplicity, the experimental part can be presented as illustrated in the flowchart in Figure 3.1. Three main activities, test circuit setup, sensor proposals and the generation of a spherical cavity defect, will be described further.
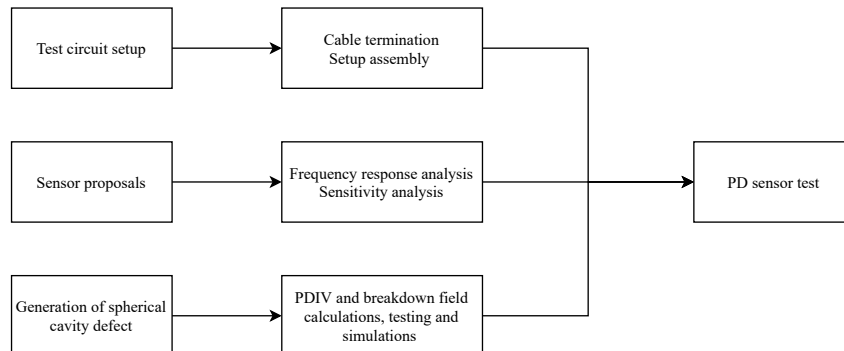
Figure 3.1: *For simplicity the method can be modelled as a flow chart. The flow chart illustrates the main activities separated into categories, leading to the PD sensor test.*

The assembly of the test circuit includes the preparation of a 12 kV cable, termination procedure, and a circuit setup model dimensioned close to an actual high voltage termination. The sensor proposal section will explain five PD measuring proposals, including illustrations and equivalent circuits. The frequency response section describes how the sensor setups were analysed in terms of frequency response. An artificial spherical cavity defect was implemented inside the cable insulation to create a void with reproducible PD characteristics. This procedure is described, including field simulations, PDIV- calculations and testing. All this boils down to the PD sensor test, where the sensitivity of one of the five sensor proposals has been analysed in terms of corona discharges and the void defect embedded inside the cable insulation. A complete list of the equipment utilised for the experimental part is given in Appendix A.

3.1 Test circuit setup

Five meters of 12 kV PEX cable with a copper conductor were prepared for termination. The cable rating and the dimensions of the cable can be seen in Table 3.1. Approximately 50 cm of the outer semi-conductor was peeled off from each end before termination utilising a cable peeler. Both ends of the cable were carefully cleaned with isopropanol before peeling.

Table 3.1: *Cable dimensions of a 12 kV PEX cable with copper conductor utilised in the test circuit setup.*

Cable rating	Diameter [mm]			
U_m	Conductor	Conductor screen	Insulation	Insulation screen
12 kV	13.0	15.0	22.8	24.8

3.1.1 Termination of cable

One end of the cable was terminated utilising a field control pad and termination tape. Approximately 10 cm of the field control pad was fitted around the cable, with two cm overlapping the intersection of the inner semi-conductor. Four overlaps of termination tape were then bundled around the field control pad. A cross-section of the termination on the cable can be seen in Figure 3.2.
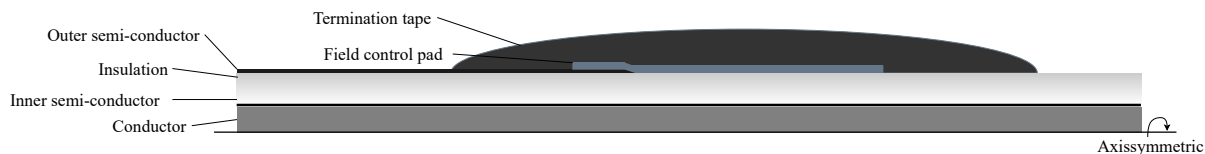
Figure 3.2: *Construction of a cable termination utilising field control padding and termination tape.*

An AIN-Indoor-slip-on termination from Nexans was fitted on the other end of the cable. An illustration of the slip-on termination is given in Figure 3.3. The slip-on termination was cut to a third (marked with a red line) only to utilise the cone with the semi-conducting layer for testing. The slip-on cone on the cable is fitted such that the outer semi-conducting layer of the cable ends where the semi-conducting layer of the cone ends to prevent additional partial discharge activity. Silicone grease was used to lubricate the cable to slide the stress cone onto the cable easily. The silicone grease will also function as sealing when the stress cone is fitted on the cable, filling potential slits or gaps in the insulation.
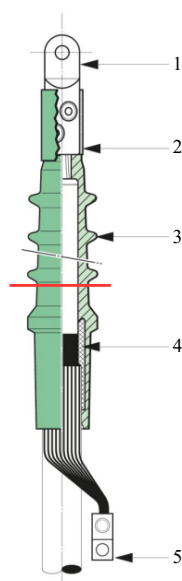
Figure 3.3: *Design of the AIN-inddor slip on termination when installed on a cable. The slip on termination was cut to a third (marked with a red line) before it was installed. 1) Logitudinally sealed mechanical or compression cable lug, 2) silicone tube or cap as additional sealing at the transition of cable lug to the termination housing when using mechanical cable lugs, 3) high flexibility silicone rubber housing, ensuring a perfect fit to the cable even during load changes, 4) Integrated conductive rubber insert, 5) earth cable lug [33].*

3.1.2   Setup assembly

Applying the principles of the design of a high-voltage termination, a test setup with similar dimensions as a termination was made. Figure 3.4 illustrate a sketch and a photo of this. The cable end with the stress cone was fastened to a wooden stand. One meter below the stress cone, a steel bottom plate of 55x55 cm was installed to simulate the bottom steel plate in a real size termination. The cable was led through a track in the steel bottom plate. Copper mesh was installed around the cable below the stress cone, acting as the earth screen of the cable. The copper mesh was further connected to the steel bottom plate for grounding. It is assumed that the behaviour of this air-insulated system will differ insignificantly from an oil-insulated system.

(a) *Explanatory drawing.*
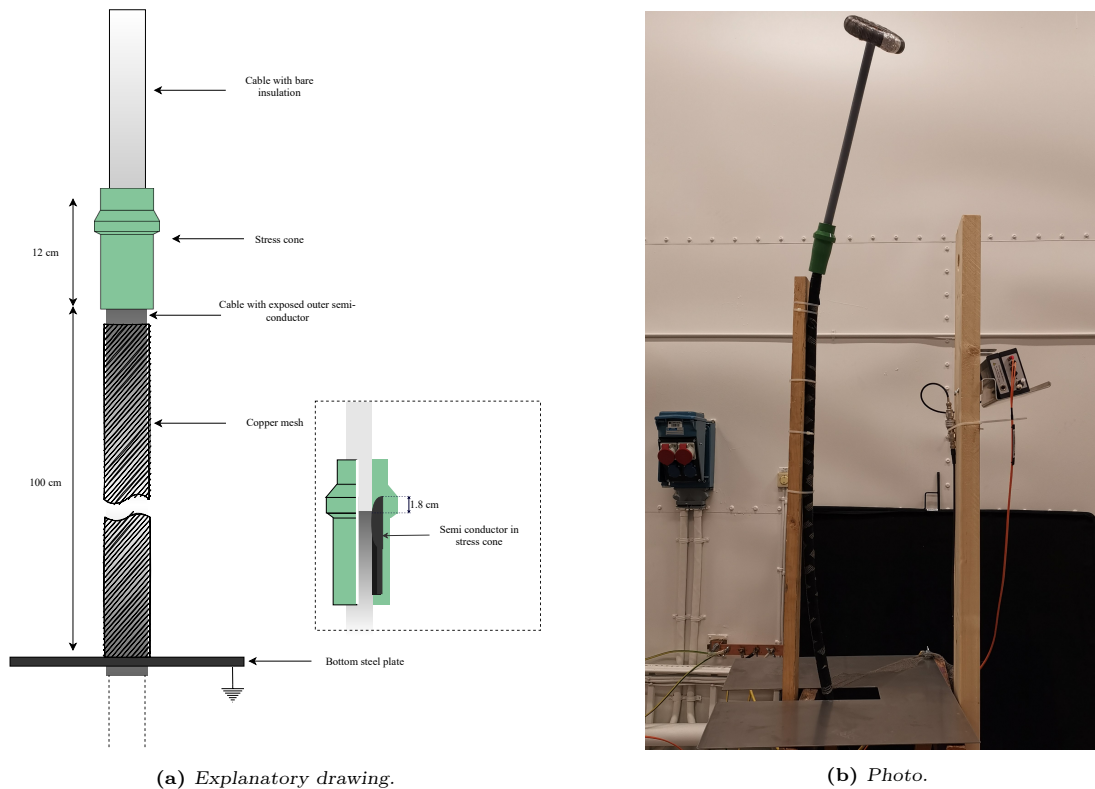
(b) *Photo.*

Figure 3.4: *Termination test setup with explanation drawing and a photo of the actual setup. A corona ring is fastened at the top of the cable to avoid corona discharges.*

A reference PD test of the cable with the slip-on cone at one end and a termination made with termination tape at the other was conducted, which showed that the circuit setup was PD free up to 30 kV$_{rms}$. The test was conducted in accordance with the IEC 60720, using the conventional PD measuring circuit, following the circuit presented in section 2.3.1, with equipment provided by Omicron MPD 600. A bandwidth of 400±325 kHz was applied for the measuring system, and the voltage was increased step-wise by 1 kV per minute until PD activity was observed. Information and details about the Omicron MPD 600 system are given in Appendix A.1.

3.2 Sensor proposals

Based on the termination design and available space inside the termination, capacitive and inductive coupling can be good alternatives for on-line partial discharge measurement. A capacitive coupler can be constructed by utilising grounding copper mesh. By this approach, the sensor will only, to a small degree, interfere with the design of the termination. Five copper mesh coupling proposals will be presented, further explained as cases 1-5. The five setups can be compared to high-pass filters having a RC-circuit as a basis.

The copper mesh has been installed on the lower part of the stress cone, acting as an electrode for all the cases. The copper mesh electrode is installed at this position as the intersection between the semi-conducting layers of the cable, and the stress cone is the area most vulnerable to defects (thereby PD). The idea is to measure PD activity directly over the source, thereby minimising the potential problems of PD signal attenuation. In addition, this location will not affect the field grading of the stress cone. It is important to mention that the characteristic impedance, Z_0, of the cable is not accounted for in the presented sensor proposals. The impedance is assumed to have a negligible effect on the sensor performance as further analysis are conducted over a small cable segment.

3.2.1   Case 1 - Copper mesh electrode with mesh screen break.

Figure 3.5 illustrate the first sensor proposal. The copper mesh on the stress cone acts as the sensor electrode, having an open circuit towards the earthing mesh. Electromagnetic waves from a PD will induce an electric signal in the copper mesh electrode. This signal is measured over the open circuit of the mesh by a measuring impedance, Z_m. The Z_m can further be connected to an oscilloscope or a PD measuring system.
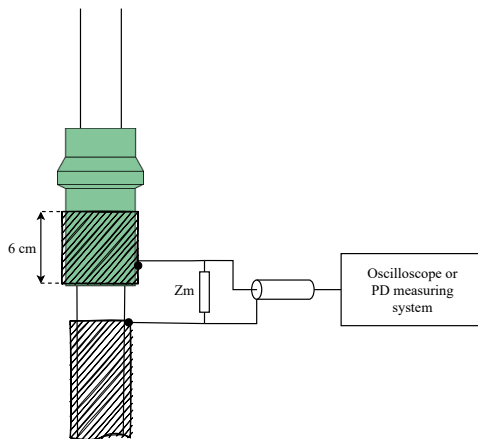
Figure 3.5: *Case 1 - capacitive coupling of PD signals with the use of a copper mesh electrode installed at the lower part of the stress cone. Electrical signals incepted from PD are measured over the mesh screen break by a measuring impedance Z_m.*

The equivalent circuit of this sensor principle can be seen in Figure 3.6 where C_{iso} is the capacitance of the insulation of the cable and C_{con} is the capacitance of the insulation of the stress cone. R_s is the stray resistance of the semi-conductor, and C_s is the stray capacitance of the copper mesh gap. Z_m is the measuring impedance, having a value of 50 Ω.
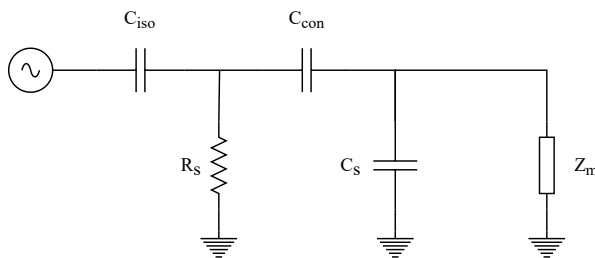
Figure 3.6: *The equivalent circuit of case 1 - copper mesh electrode with mesh screen break as illustrated in Figure 3.5. C_{iso}=cable insulation capacitance, C_{con}=capacitance of the stress cone insulation, R_s=stray resistance of the semi-conductor, C_s=stray capacitance of the copper mesh screen break, Z_m=measuring impedance.*

A photo of the copper mesh connections can be seen in Figure 3.7. A nylon bolt and a nylon nut connect the banana wires in both connection points on the copper mesh. Aluminium spacers were used between the connection points to increase the contact surface. The banana wire from the ground copper mesh is connected to the earth screen of the coax, while the wire from the copper mesh sensor is connected to the coax conductor. The distance between the connection points is 4 cm, while the copper mesh gap is approximately 2 cm. Tape was fastened around the copper mesh to avoid threads and the copper mesh from pointing out.
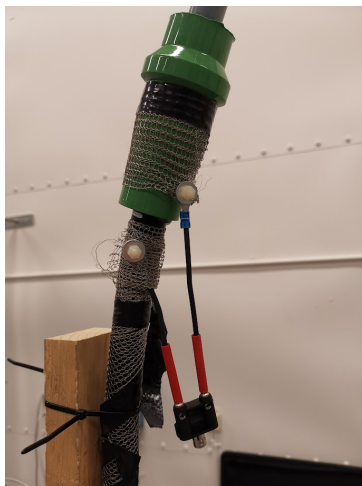
Figure 3.7: *The copper mesh connections. Nylon bolts and nuts connects the banana wires to the coax cable.*

This type of capacitive PD measurement differs from the capacitive coupler explained in section 2.3.3 in terms of design and coupling electrode. The measuring circuit will introduce an additional capacitance due to the insulation in the stress cone. The electrode differs as most of the earlier research and testing on capacitive couplers have used a copper foil strip. The measuring principle is, however, similar. Case 1 will be the base case for further connection principles.

3.2.2   Case 2 - Coil inserted in the mesh screen break

The same setup as case 1 applies for the second principle, only that a coil of 10 mH has been inserted in the copper mesh screen break. The principle is illustrated in Figure 3.8. The purpose of the inserted coil is to prevent the relatively high 50 Hz current from flowing through the measuring equipment. This current can create problems related to superimposition of discharge signals. The output signals are measured in the measuring impedance, Z_m, parallel with the coil, L.
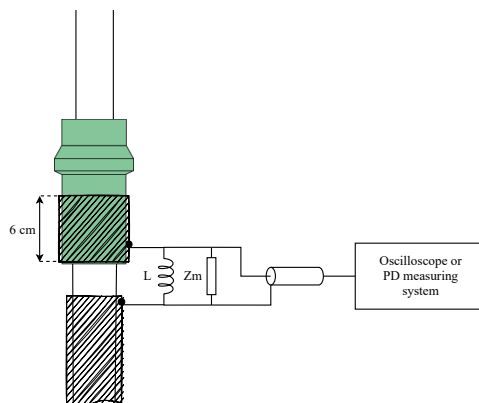
Figure 3.8: *Case 2 - capacitive coupling of PD signals with the use of a copper mesh electrode and a coil, L, in the copper mesh screen break. Such a topology will prevent the relatively high 50 Hz current from flowing through the measuring equipment.*

The equivalent circuit for case 2 can be seen in Figure 3.9. A coil, L, of 10 mH have been inserted in the mesh screen break.
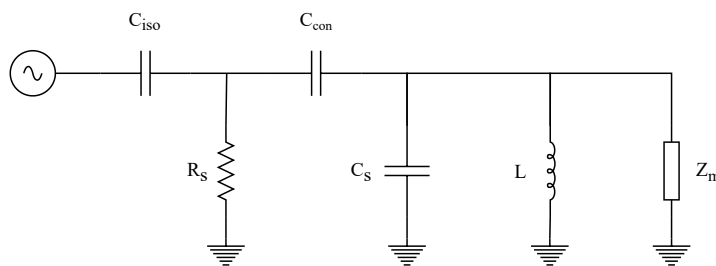
Figure 3.9: *The equivalent circuit of case 2 - coil, L, inserted in copper mesh screen break as illustrated in Figure 3.8. C_{iso}=cable insulation capacitance, C_{con}=capacitance of the stress cone insulation, R_s=stray resistance of the semi-conductor, C_s=stray capacitance of the copper mesh screen break, Z_m=measuring impedance.*

3.2.3   Case 3 - Transformer in mesh screen break

An isolating transformer with a 1:1 ratio has been inserted in the mesh screen break for the third case. The isolating transformer forms electric isolation between the mesh electrode and the earthing copper mesh. This principle is illustrated in Figure 3.10. The intention of the transformer is to suppress noise signals induced in the earthing network. The measuring impedance, Z_m, measures signals over the isolating transformer.
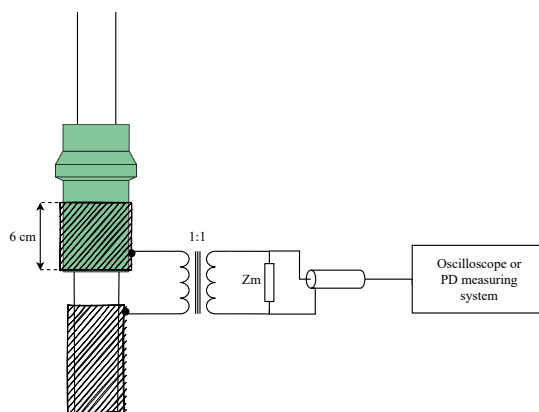
Figure 3.10: *Case 3 - capacitive coupling of PD with the use of a copper mesh electrode and a isolating transformer. The transformer has a 1:1 ratio, and will suppress noise signals induced in the earthing network.*

The equivalent circuit for sensor principle 3 can be seen in Figure 3.11. A small transformer with a 1:1 ratio have been inserted in the mesh screen break.
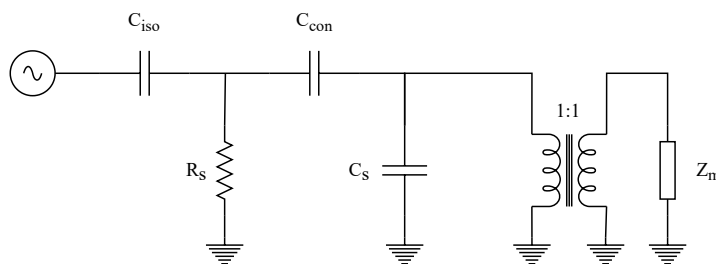
Figure 3.11: *Equivalent circuit of case 3 - a 1:1 transformer inserted in the mesh screen break as illustrated in Figure 3.10. C_{iso}=cable insulation capacitance, C_{con}=capacitance of the stress cone insulation, R_s=stray resistance of the semi-conductor, C_s=stray capacitance of the copper mesh screen break, Z_m=measuring impedance.*

3.2.4 Case 4 - Copper foil electrodes

The fourth proposal uses copper foil strips to measure the output signals over the copper mesh screen break. This principle might strengthen the signals by allowing a more precise measurement according to the geometry of the stress cone and a larger contact surface. The principle is illustrated in Figure 3.12. One strip of copper foil was fitted around the stress cone and another around the cable. Both strips have a width of 2 cm. The upper strip is used as the measuring electrode, and the bottom is used for grounding. The copper strips are connected to the measuring impedance, Z_m, which measures the induced electrical signals.
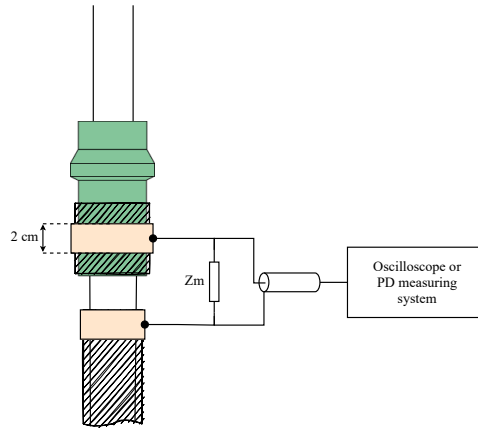
Figure 3.12: *Case 4 - capacitive coupling of PD signals with the use of copper strips. The purpose of this measuring principle is to strengthen the output signals.*

The equivalent circuit for case 4 can be seen in Figure 3.13. This equivalent is the same as the equivalent for case 1.
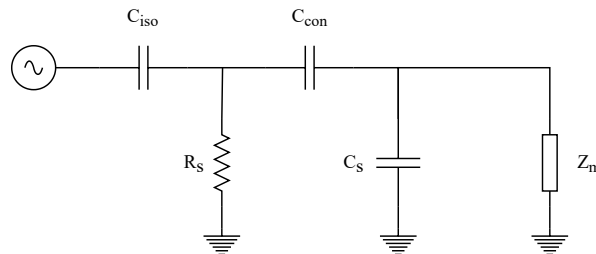
Figure 3.13: *Equivalent circuit of case 4 - copper foil electrodes as illustrated in Figure 3.12. This equivalent will be equal to the equivalent for sensor case 1. C_{iso}=cable insulation capacitance, C_{con}=capacitance of the stress cone insulation, R_s=stray resistance of the semi-conductor, C_s=stray capacitance of the copper mesh screen break, Z_m=measuring impedance.*

3.2.5 Case 5 - Inductive coupling of the signals induced in the copper mesh

Figure 3.14 illustrates the fifth principle where the whole copper mesh is used as the sensor electrode. For this proposal, there is no copper mesh screen break. Instead of the screen break, an inductive coupler (HFCT) is clamped around the ground connection (copper mesh) of the termination to measure the output signals. The electrical signals induced from a PD in the copper mesh will induce a time-varying magnetic field in the HFCT, which generates a voltage across the measuring impedance. This method will be beneficial as it does not require any connection to live parts in the termination.
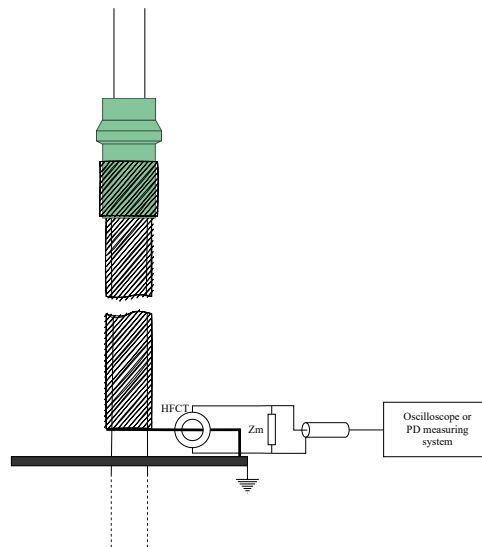
Figure 3.14: *Case 5 - inductive coupling of signals induced in the copper mesh. The copper mesh is pulled all the way up over the stress cone and a HFCT is clamped around the ground connection.*

The equivalent circuit of this measuring principle can be seen in Figure 3.15 where a HFCT is clamped around the grounding copper mesh further connected to the measuring impedance, Z_m. For further analysis regarding this sensor proposal, the current probe from TEGAM will be utilized. Information about this sensor is given in Appendix A.2.
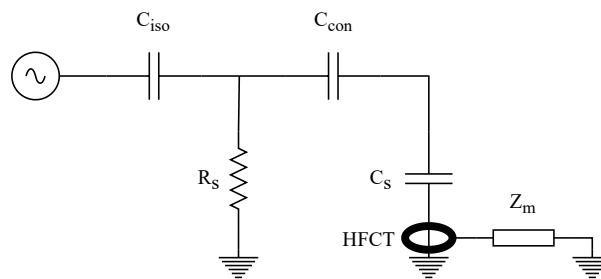
Figure 3.15: *Equivalent circuit of sensor case 5 - inductive coupling of the signals in the copper mesh as illustrated in Figure 3.14. C_{iso}=cable insulation capacitance, C_{con}=capacitance of the stress cone insulation, R_s=stray resistance of the semi-conductor, C_s=stray capacitance of the copper mesh screen break, Z_m=measuring impedance.*

3.3 Frequency response and sensitivity analysis

The following chapter will explain the procedure of conducting a frequency response analysis (FRA) for the sensor proposals and sensitivity analysis. FRA measurements were performed for the five sensor proposals to analyse the gain. Based on results from this analysis, it was decided to only continue with sensor case 1 - copper mesh screen break, hereafter called the copper mesh sensor. Analysis in LtSpice for the copper mesh sensor will be explained, succeed by the procedure for the sensitivity analysis.

3.3.1 Frequency response with Aglient E5061B Network Analyzer

A network analyser was utilised to measure the frequency response of the five sensor setups. The frequency response was conducted by performing a 50 Ω S-parameter measurement using the Agilent E5061B Network Analyzer (VNA). A simplified sketch of the S-parameter measurement can be seen in Figure 3.16. The device under test, DUT, is connected to ports 1 and 2 of the VNA. The DUT consists of the cable with the slip-on termination and copper mesh sensor connections. Port 1 of the VNA was connected to the cable conductor, whereas port 2 was connected to the copper mesh electrode and the HFCT for case 5. One test was conducted for each of the five sensor proposals to identify how the different sensor connections influence the gain. A frequency span of 1 kHz to 100 MHz was used for the analysis.
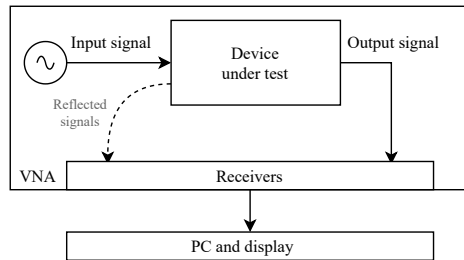
Figure 3.16: *Simplified sketch of the S-parameter measurement conducted with a Network Analyser.*

3.3.2 Analysis in LtSpice

The circuit of the copper mesh sensor was modelled in LtSpice to examine how the value of the stray capacitance, C_s, and the stray resistance, R_S, affect the gain of the copper mesh sensor. LtSpice is a high-performance SPICE (Simulation Program with Integrated Circuit Emphasis) simulator software, including a graphical schematic capture interface[34]. Analysis with the frequency ranging from 1 Hz to 1 GHz was conducted by first varying the C_s and then R_s. C_{iso} and C_{con} were calculated, utilising the principles of cylinder capacitors, to 15.26 pF and 26.60 pF, respectively and inserted into the parameters. More details regarding these calculations can be seen in Appendix B. R_m (Z_m) was sat to 50Ω. The circuit modelled in LtSpice can be seen in Figure 3.17.
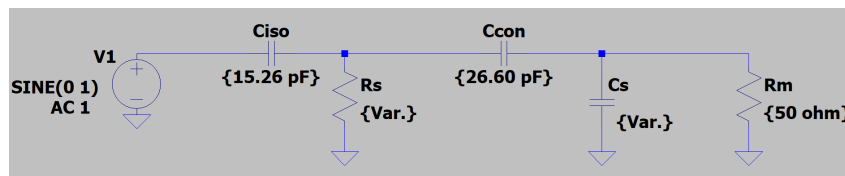
Figure 3.17: *The circuit of sensor case 1 modelled in LtSpice with calculated values of C_{iso} and C_{con}. The analysis was performed to examine how different values of C_s and R_s affects the coupler output. Var. = variable.*

3.3.3 Sensitivity analysis by charge injection

The sensitivity (or the lowest measurable apparent charge value) of the copper mesh sensor was performed by injecting charges of known values into the cable test object. Charge values ranging from 1 - 100 pC were injected into the top of the cable test object, approximately 0.6 m from the copper mesh electrode. The signal from the copper mesh sensor was measured in the time domain and compared to the conventional measuring technique. This test will indicate the sensitivity of the copper mesh sensor.

The bandwidth of the copper mesh sensor was sat to 16±0.75 MHZ for the analysis, adjusted according to the noise level. At this bandwidth, the noise-level was relatively low (∼ 1.5 pC). The charge injection test circuit is illustrated in Figure 3.18. The charge was injected by utilising a standard CAL1A calibrator from Power Diagnostix. The copper mesh connections are connected to MPD 600, having an internal measuring impedance, Z_m, of 50 Ω.
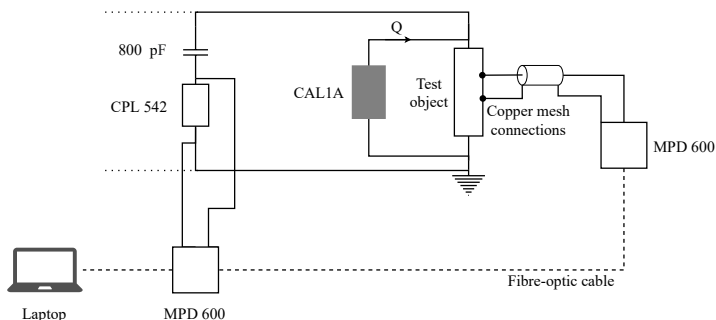
Figure 3.18: *Sensitivity analysis of the copper mesh sensor was performed by injecting charge values, Q, of known values to quantify the lowest measurable apparent charge value. The conventional measuring technique, provided by Omicron, was used simultaneously to have a basis of comparison.*

3.4 Generation of spherical cavity defect

Internal discharges such as voids inside solid dielectrics are considered the most harmful for dielectric elements and lead to insulation failures. Therefore, an attempt to generate an artificial void inside the cable insulation was conducted to test the sensitivity of the sensor principle. Several approaches of void generation were evaluated with the primary goal of creating a void defect that generates similar and reproducible PD signals without interfering too much with the insulation system. Reproducible PD signals can be obtained using materials that do not change due to discharges. One approach considered generating a flat air-filled mica cavity. However, this was not pursued due to difficulties implementing the defect inside the cable insulation. The procedure and calculations regarding this defect are, however, given in Appendix C.

3.4.1 Microscope examination of micro-glass spheres

It was chosen to utilise micro glass spheres to simulate spherical air-filled cavities. Such spheres are hollow microscopic balls made of glass (quartz). Glass, in general, has high dielectric strength and is, therefore, a suitable material for creating an artificial void defect. The micro-glass spheres were examined under a microscope, and the outer diameter was measured to be in the interval from 0.1 mm to 0.6 mm. Figure 3.19 illustrates the micro glass spheres under a microscope enlarged a 100 times.
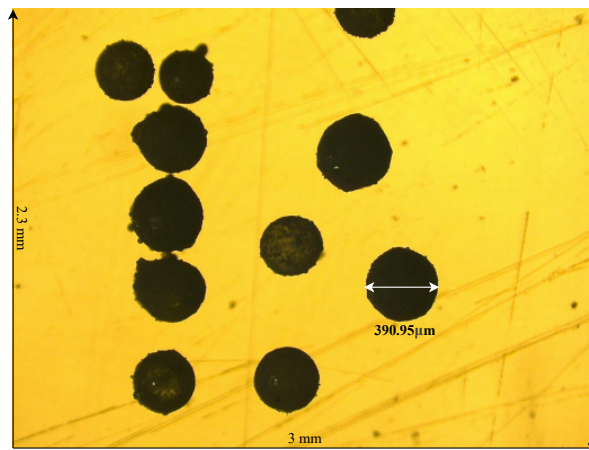
Figure 3.19: *Micro-glass spheres were examined under a microscope to measure the mean diameter of the spheres. The spheres are black due to the lighting of the microscope, but are in fact white in color.*

Some spheres were cast in epoxy to obtain the inner radius of the spheres. Approximately 2 grams of spheres were mixed in 50 grams of epoxy resin and 6 grams of hardener. The mixture was placed in a vacuum chamber to extract air trapped inside the epoxy before it was retracted into syringes. The syringes acted as the mould, and the epoxy mixture was left to cure inside them for 12 hours. The finished objects were then polished such that the cross-section of the micro-glass spheres became visible, thereby examining the cavity walls of the spheres. Approximately 20 spheres were examined, and the cavity wall was measured and registered for each one. An average thickness of 0.015 mm was calculated and used for further simulations. Figure 3.20 illustrate a microscope photo of the cross-section of micro-glass spheres in a polished epoxy object.
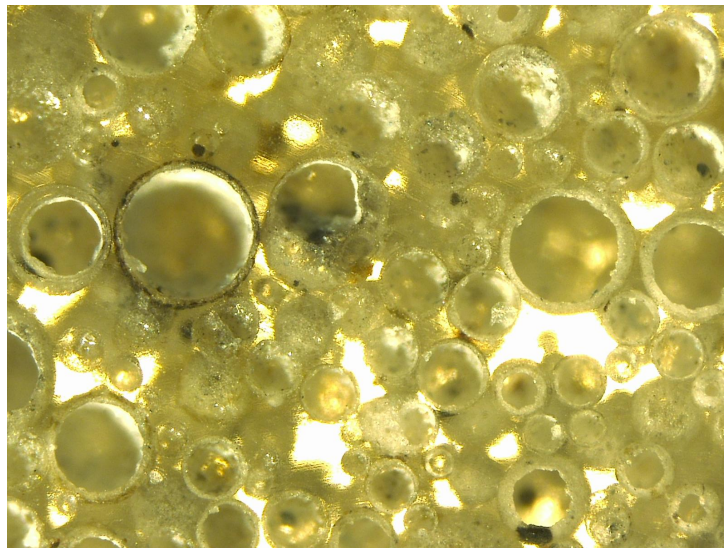
Figure 3.20: *Micro-glass spheres were cast in epoxy to examine the thickness of the glass-wall. The epoxy object was polished such that the cross section of the micro-glass spheres became visible under a microscope. The micro-glass wall of 20 spheres were measured, and an average thickness of 0.015 mm was calculated.*

3.4.2 Inception voltage calculations of one micro-glass sphere in silicone rubber

Simple calculations were performed to find the inception voltage of discharges in the spherical cavities of different diameters. The calculation assumes that only one cavity is present in the dielectric of silicone rubber. A figure of one cavity with a diameter of d_c inside a dielectric (silicone rubber) is illustrated in Figure 3.21.
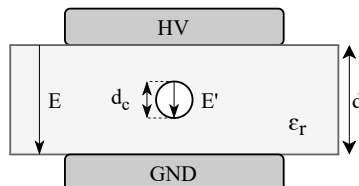
Figure 3.21: *Model of a spherical cavity in a dielectric material between a electrode-configuration.*

Parameters utilised to calculate the PDIV of the spherical void are given in Table 3.2. It was assumed that the pressure inside the spherical cavity was homogeneous. Therefore the approximation to Paschen's curve, as given in Equation 2.1, was used to find the withstand strength, U_s. U_s was then divided by the d_c to obtain the maximum electric stress in the cavity, E'. Equation 2.2 was used to calculate the electric stress in the solid dielectric, E. PDIV was obtained by multiplying E with the dielectric thickness, d. These calculations do not account for the glass wall of the sphere. It is assumed that the wall has a small impact on the PDIV.

Table 3.2: *Parameters used to calculate the inception voltage of one micro glass sphere enclosed in dielectric material (silicone rubber).*

Parameter	Value
p	1 bar
ε_r	2.8
d_c	0.1 - 0.6 mm
d	2 mm

3.4.3 Inception voltage test of the micro-glass spheres

The inception voltage of the micro-glass spheres was measured by performing PD measurements on spheres cast in silicone rubber. The purpose of this is to obtain the breakdown field strength of the micro-glass spheres, which will be helpful for subsequent experiments.

Making the test objects

Four test objects were constructed. Spheres were moulded in liquid silicone rubber (Elastosil LR 3003/60 A/B) in a circular form with a diameter of 10 cm and a width of 2 mm. An illustration of the test object is given in Figure 3.22. Two test objects without micro-glass spheres were also constructed to have a reference. More details about the cast and curing procedure are given in Appendix D.
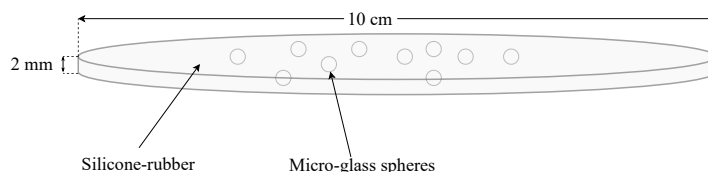
Figure 3.22: *Micro-glass spheres were cast in a circular silicone rubber mold to test PDIV. The figure is not to scale, only an illustration of the principle.*

Conventional PD-measurements to find the PDIV

The inception voltage of the micro-glass spheres was tested by performing a conventional PD measurement with equipment provided by Omicron MPD 600. As illustrated in Figure 3.23, the silicone rubber test objects were submerged and tested one by one in an insulated tank filled with synthetic ester (MIDEL 7131) pressed between a potential electrode (HV) and a ground electrode (GND). It was assured that no air bubbles were trapped when the test object was submerged to avoid unwanted discharges.
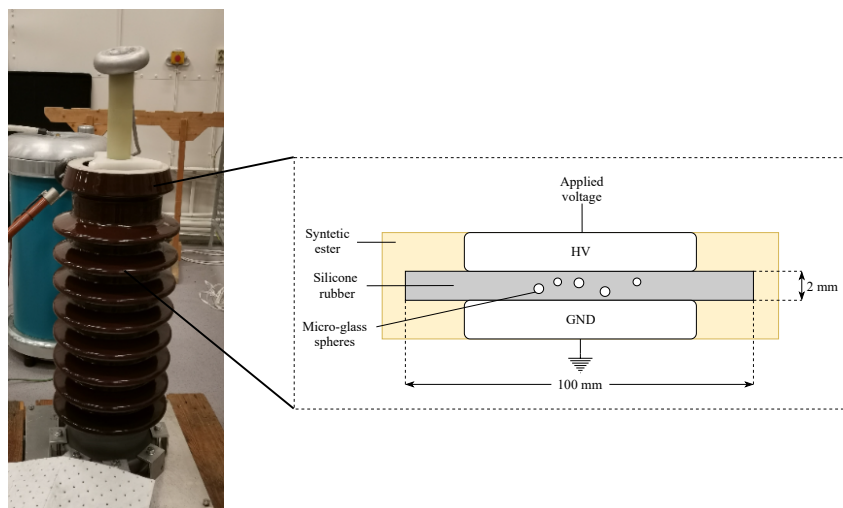
Figure 3.23: *The test object for the PDIV test of the silicone rubber objects. The silicone rubber object was placed in-between a potential electrode (HV) and a ground electrode (GND) submerged in synthetic ester enclosed in an insulator tank (not to scale).*

The insulated tank with electrodes was further connected to a coupling capacitor and the CPL. The setup is illustrated in Figure 3.24. A reference test was conducted by testing the test objects without micro-glass spheres. For this test, the voltage was increased by 1 kV each minute up to ~15 kV. Each of the four test objects with micro-glass spheres was then tested and compared to the reference test. For this test, the voltage was step-wise increased by ~500 V each minute until PD-activity was observed. The PD measurements were done in compliance with the IEC 60270, utilising a bandwidth of 400±325 kHz. All measurements were recorded, and data from the measurements were exported for further analysis.
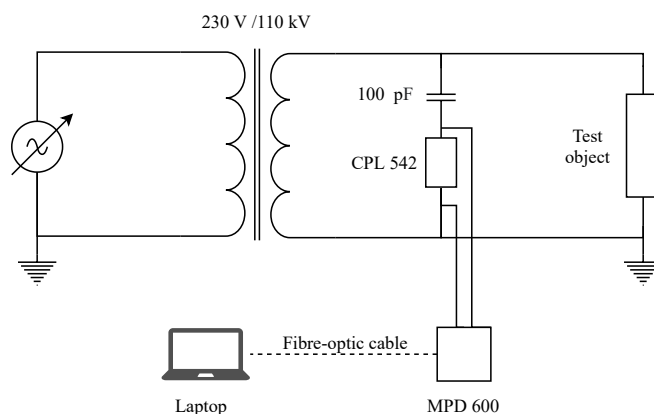
Figure 3.24: *Conventional PD measurements circuit for the PDIV test of the micro-glass spheres. Conventional PD measuring equipment was used to find the inception voltage.*

3.4.4   Field simulations of one micro-glass sphere in silicone rubber

Field simulations were conducted to analyse how the field inside one micro-glass sphere will behave with induced voltage. The simulations were conducted in Comsol by creating a 2D rotationally symmetrical model. A geometry consisting of a spherical air-filled cavity with a diameter of 0.3 mm encapsulated by a 0.015 mm thick glass (quartz) wall in silicone rubber was made, as illustrated in Figure 3.25a. The mesh structure of the geometry is illustrated in Figure 3.25b.

<div align="center">(a) The geometry of the cavity in silicone rubber.   (b) The mesh structure of the analysis.</div>
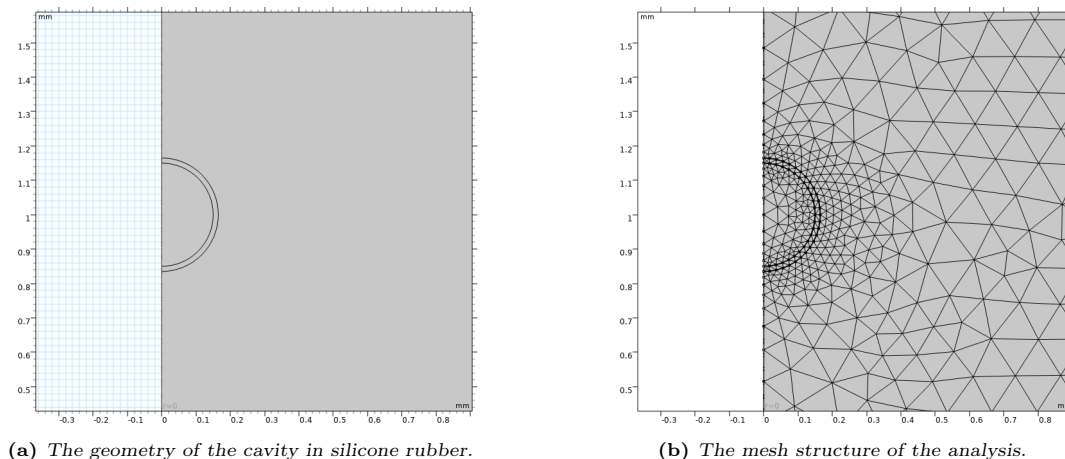
Figure 3.25: *Field simulations was conducted in Comsol were a 2D axissymmetric model of a cavity in silicone rubber was made.*

3.4.5   Micro-glass sphere implementation in cable insulation

Several proposals for micro-glass sphere implementation were evaluated to examine the sensitivity of the copper mesh sensor relative to void discharges. The evaluation and details regarding preliminary defect implementation experiments can be read in Appendix E. Based on preliminary defect implementation experiments results, it was decided to cast a micro-glass sphere in epoxy directly into the cable insulation. The principle is illustrated in Figure 3.26.

Figure 3.26: *Principle of defect implementation of a micro-glass sphere in the cable insulation sealed by silicon or epoxy.*

The AIN-slip-on termination was removed, and a hole of a diameter of 2 mm was drilled 0.5 mm down into the insulation. The hole was drilled as close to the inner semi-conductor of the cable as possible. Twenty-five grams of EpoFix Resin was mixed with 3 grams of Resin hardener. EpoFix Resin is a low viscosity epoxy cold mounting system which cures at room temperature in about 12 hours. It has no shrinkage, which is beneficial for avoiding gaps between the insulation and the epoxy.

The epoxy mixture was placed in a vacuum chamber for about an hour to extract trapped air bubbles before being retracted into a syringe. One micro glass sphere was cast into the insulation hole in epoxy by ejecting the epoxy from the syringe and utilising a pair of tweezers to place the micro-glass sphere. The epoxy cast was left curing for 12 hours and studied under a microscope before the AIN-slip-on termination was fitted back onto the cable.

3.4.6 Expected PDIV of the implemented micro-glass sphere

Based on the PDIV measurement results and the field simulations, the expected PDIV of one micro-glass sphere cast inside the cable insulation was calculated. The breakdown field of the sphere was found by calculating the field inside the silicone rubber and using the field correlation of spherical gas-filled cavities in a dielectric (Equation 2.2) to find the breakdown field of the micro-glass spheres. The expected PDIV value (the voltage that needs to be applied to the cable for PD inception) of the implemented micro-glass sphere was calculated using Equation 2.5 for cylindrical conductors.

3.5 Sensor testing - partial discharges

Based on the FRA-measurements, as mentioned, case 1 - copper mesh electrode with mesh screen break was chosen for further experiments. The sensor testing involved testing the sensor sensitivity relative to defects compared to the conventional measuring technique. PD measurements of both corona and the implemented micro-glass sphere were performed. These measurements were also conducted to identify the behaviour of the micro-glass sphere, including PDIV and PRPD-patterns.

Corona discharges incepts typically from sharp edges and points into air. Therefore, corona was generated by letting a copper wire point out of the cable conductor into air. Figure 3.27 illustrate the copper wire around the bare cable conductor. Note, the corona test was performed before defect implementation to only test one PD source at the time.
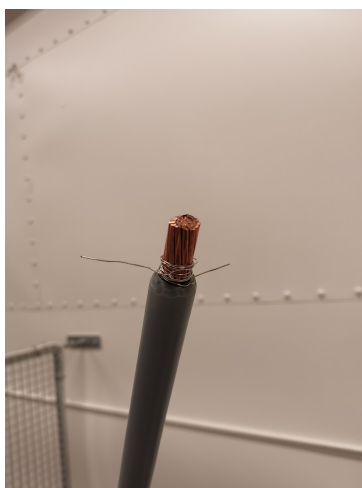
Figure 3.27: *Corona was generated by a copper wire fasten around the bare cable conductor for the PD sensor test. The corona test was performed before defect implementation.*

The test circuit with both the conventional measurement setup and the copper mesh setup (case 1) is illustrated in Figure 3.28. The MPD 600 from Omicron was utilised as the measuring impedance for the copper mesh setup. The voltage was increased step-wise by ~500 V until PD-activity was observed. The copper mesh connections are the same as the one presented in Figure 3.7.
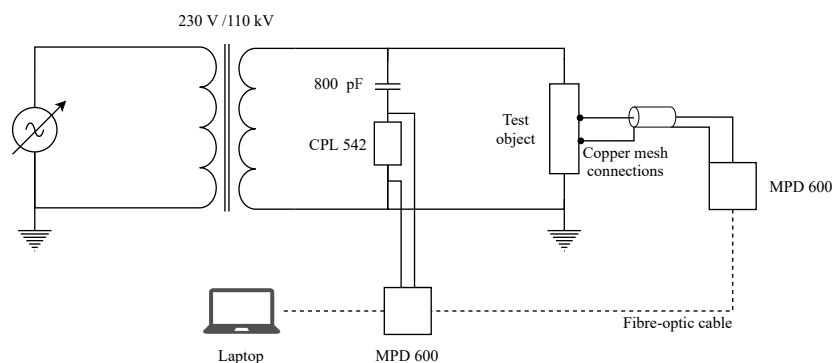
Figure 3.28: *PD sensor test circuit setup utilising both the conventional measuring technique provided from Omicron and the principles of sensor case 1 - copper mesh gap. The conventional technique is used simultaneously to obtain a basis for comparison.*

The PD threshold was sat based on the noise floor for the conventional measuring technique and the copper mesh sensor. This avoids actual discharge values getting "drowned" by noise signals. The bandwidth of the conventional measuring technique was sat to 400kHz±325 kHz, which is in accordance with the IEC 60270 standard for PD measurements. The bandwidth of the copper mesh sensor was chosen by examining the FFT (Fast Fourier Transform) in the Omicron software, and adjusted to a bandwidth with relatively low noise signals to avoid a high PD threshold. Calibration of the measuring circuit was performed by injecting a charge of 10 pC by a calibrator to the test object (same procedure as explained in the sensitivity analysis in section 3.3.3).

Data from each test was recorded in the Omicron software, and data (sampling time, pulse repetition rate, voltage etc.) from the recording was exported to excel. To analyse the performance of the copper mesh sensor, the sampled pulse repetition rate of the copper mesh sensor was compared to the pulse repetition rate of the conventional measuring technique. The resulting PRPD patterns were analysed for defect recognition.

3.6   Field simulations of cavity in cable insulation

Based on the obtained results from the PD sensor test, considering the void defect, field simulations of the slip-on stress cone with a spherical cavity inside the cable insulation was conducted. A 3D model with axis-symmetric geometry of the cable and stress cone was made in Comsol. The purpose of this simulation is to see how the micro-glass sphere affects the field in the cable with stress cone, and to examine the field strength inside the micro-glass sphere at expected PDIV.

Figure 3.29 illustrates the geometry and an enlarged photo of the area with the cavity, marked as a red rectangle in Figure 3.29a. The cavity location is the same as the location of the micro-glass sphere placed inside the cable insulation. Information of the dimensions of the stress-cone is given in Appendix F. The cable is modelled based on the dimensions given in subsection 3.1 (Table 3.1).
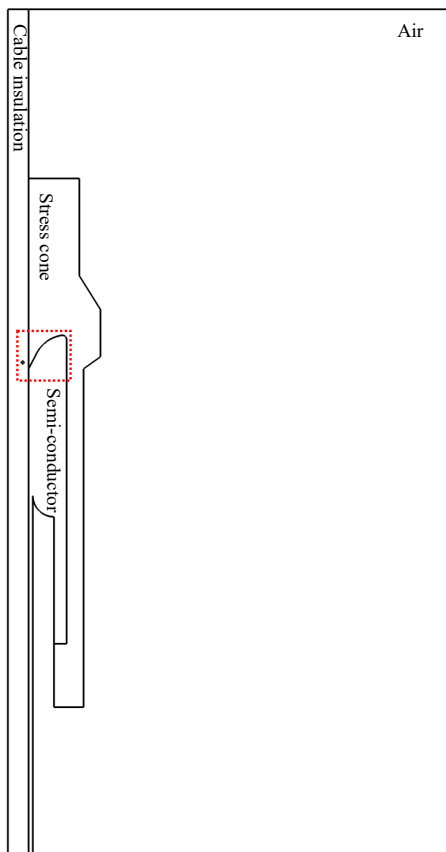
(a) *The geometry of the cavity in the cable insulation.*
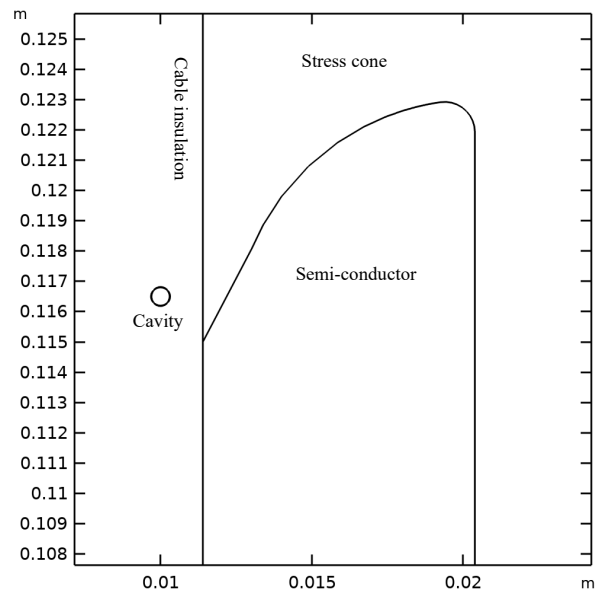
(b) *Cavity in insulation.*

Figure 3.29: *Field simulations was conducted in Comsol of 3D axissymmetric model of the stress cone around the cable with a cavity embedded inside the cable insulation.*

Figure 3.30 illustrates the finished 3D-model of the stress-cone around the cable. The air domain around the stress-cone is 0.2x0.2 m and is assumed to have a small influence on the field of the stress cone.
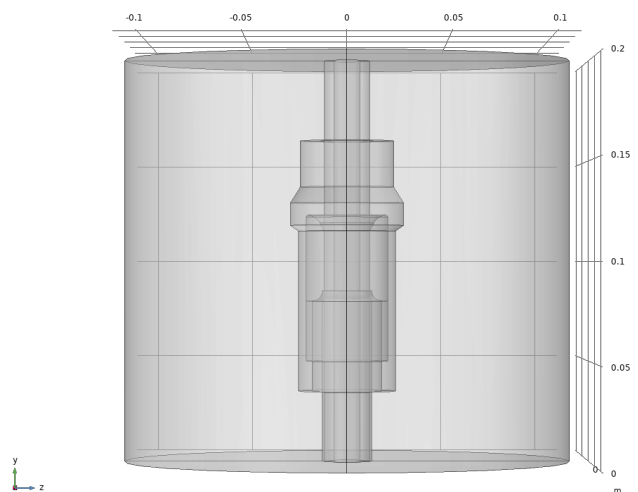
Figure 3.30: *The 3D-model of the stress cone around the cable with a cavity embedded inside the cable insulation.*

4   Results

In the following section the results from the experimental part of the thesis will be presented. The results are sorted according to the order of the method chapter, thereby first presenting the results from the FRA- and sensitivity analysis, secondly the generation of the spherical cavity, and lastly the PD sensor test and the field simulations of the stress cone.

4.1   Frequency response and sensitivity analysis

The results of the frequency response analysis and sensitivity analysis will be presented in this section. Results regarding the FRA with the network analyser compares the 5 different sensor proposals in terms of frequency response plots. The FRA conducted in LtSpice evaluates the frequency response of sensor case 1 with increasing values of C_s and R_s. An indication of the lowest measurable charge value for sensor case 1 is given in the sensitivity analysis.

4.1.1   FRA with network analyser

The gain of the five sensor proposals was found by performing a standard S-parameter measurement. Figure 4.1 illustrates the S_{21}-parameter for the five different sensor proposals in the frequency range 1 kHz to 100 MHz.
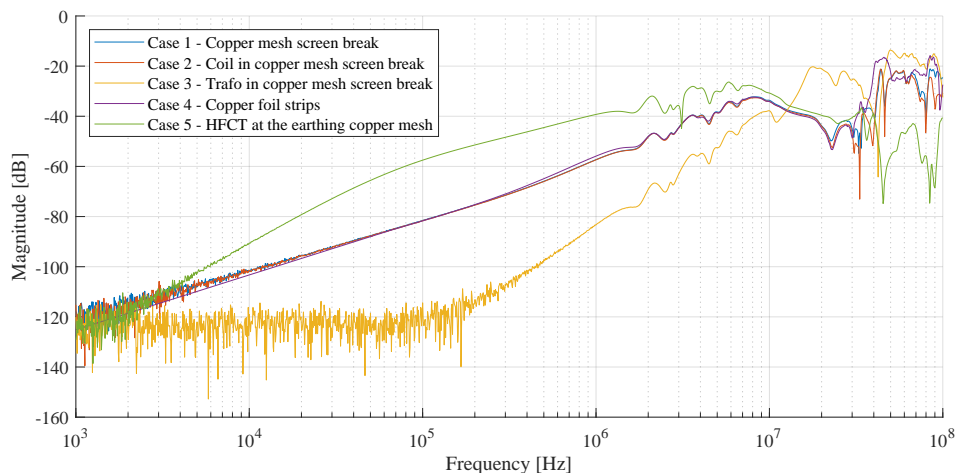
Figure 4.1: *Measured $S_2 1$-parameter between input and output for the five different sensor proposals in the frequency range from 1 kHz to 100 MHz.*

It can be seen in the frequency response characteristics of the sensor proposals that the frequency response gain increases with increasing frequency. Highest gain for all proposals, besides case 5, is achieved at frequencies from 10 MHz to 100 MHz. Sensor case 5 have the highest gain in the frequency range: 1 MHz to 10 MHz. Therefore, the design of the sensor detection frequency band in the 1~100 MHz range could be a good alternative for PD detection.

Case 1, 2 and 4 have somewhat similar frequency response. Sensor case 5 perform better at frequencies lower than the other proposals, but have a higher attenuation at frequencies over 100 MHz, compared to the other proposals. Sensor case 4 - copper foil strips, is the only proposal not subjected to noise signals at the lowest frequency ranges, while sensor case 3 - trafo in copper mesh screen break, is subjected to noise signals at frequencies ranging from 1 kHz to above 0.1 MHz.

It was decided to only continue with sensor case 1 after the FRA analysis. As can be seen from the results, the difference in the gain at the highest frequency ranges for the different sensor proposals is low. Case 1, 2 and 4 have almost the same output signal, while case 5 have a higher attenuation of the signal and case 3 is subjected to noise signals. In addition, case 1 is the simplest as it does not require considerable changes to the design of a high voltage termination.

4.1.2   Analysis in LtSpice

To analyse how the value of the stray capacitance, C_s, and the stray resistance, R_s, affects the copper mesh sensor output (sensor case 1), simulations was conducted in LtSpice. The model utilised in LtSpice can be seen in Figure 3.17. Figure 4.2 illustrates the results from the analysis. Figure 4.2a illustrate the FRA of the copper mesh sensor with changing stray capacitance, C_s, values. For these analysis R_s was sat to 100 Ω. Figure 4.2b illustrates the FRA with changing stray resistance, R_s. In this analysis the stray capacitance was sat to 5 pF.

(a) *Variable value of C_s.*   **(b)** *Variable value of R_s.*
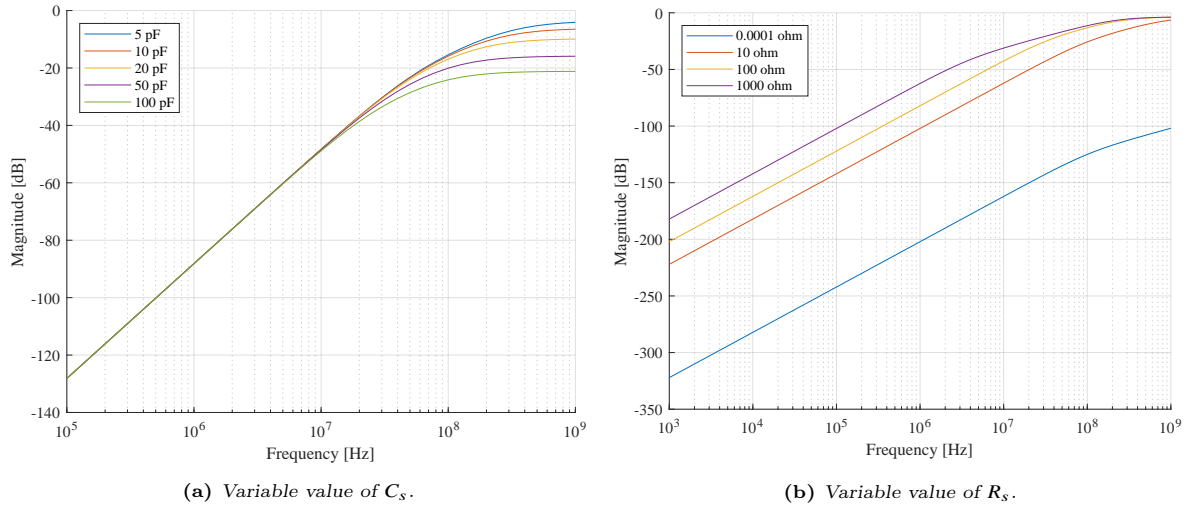
Figure 4.2: *Frequency response analysis of sensor case 1 with different values of C_s and R_s.*

The results indicates that C_s should be as low as possible, and R_s as high as possible. Similar to the FRA measurements conducted with the network analyser, the gain of the sensor increases with increasing frequency (independent of the variable values of C_s and R_s). The curves level out at frequency values over 100 MHz with changing C_s values. There is none or minimal difference in the attenuation for R_s equal to 10, 100 and 1000 Ω for frequencies above 100 MHz, while a R_s close to 0 has an attenuation of 100 dB or higher at the same frequency level.

4.1.3   Sensitivity analysis

The sensitivity of the copper mesh sensor was analysed in terms of injecting known charge values into the test circuit (cable conductor). It is important to mention that injected charges will differ from signals stemming from a defect, however this will give an indication of the sensitivity of the copper mesh sensor. A comparison of the measured apparent charge values for the conventional measuring technique and the copper mesh sensor at injected charges is given in Table 4.1. Both the conventional measuring technique and the copper mesh sensor was calibrated at 100 pC before the injected charge value was reduced step-wise to 50, 20, 10, 5 and 2 pC.

Table 4.1: *Injected charge, charge measured by the conventional technique and charge measured by the copper mesh sensor. The copper mesh sensor is able to measure charge values down to 5 pC. At lower charge values the detection is affected by noise signals.*

Injected charge, [pC]	100	50	20	10	5	2
Conventional, 400±325 kHz, [pC]	99.54	49.64	19.83	9.85	5.07	2.44
Copper mesh, 16±0.75 MHz, [pC]	99.78	47.11	19.83	7.71	3.73	1.79

The copper mesh sensor was able to measure charge values down to 5 pC. It measures approximately 2 to 3 pC lower charge values than the conventional measuring technique at injected charges of 5, 10 and 50 pC. At the lowest charge values, the measurements were affected by noise signals ranging from 1.5 pC to 2.5 pC. This was both observed during the sensitivity analysis and interpreted from the measurement data. It is therefore assumed that measured signals below 5 pC are due to noise signals.

4.2   Generation of spherical cavity

The results regarding the generation of the spherical cavity will be explained in the following subsections. This includes PDIV calculations and testing, the field simulations of one sphere in silicone rubber, and defect implementation with the resulting expected PDIV.

4.2.1   PDIV calculations of micro-glass spheres in silicone rubber

The results of the calculated PDIV of one sphere at different cavity diameters, in silicone rubber with an ε_r of 2.8, can be seen in Figure 4.3. The PDIV values varies from 10.63 kV to 6.09 kV according to the diameter. The calculated PDIV corresponds to the applied voltage over the 2 mm thick silicone rubber test object, with an assumed pressure of 1 bar inside the glass sphere.
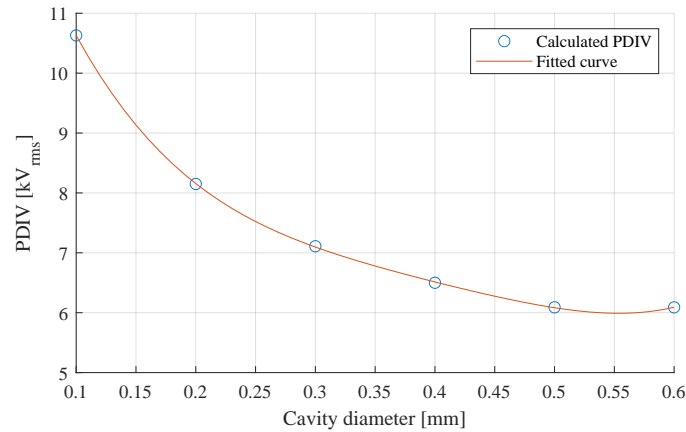
Figure 4.3: *Calculated PDIV for an air-filled spherical cavity and fitted curve, for one sphere in silicone rubber with an ε_r of 2.8, of varying diameters assuming a pressure inside the cavity equal to 1 bar.*

4.2.2   PDIV measurements of micro-glass spheres in silicone rubber

PDIV measurements of the micro-glass spheres were found by conducting a conventional PD measurement of the silicone rubber test objects. The measured PDIV, calculated breakdown field, E_{bd} of the micro-glass spheres and measured mean diameter, d, for 20 micro-glass spheres inside the silicone rubber test objects can be seen in Table 4.2. The PDIV varies from 4.66 kV to 8.60 kV, with a mean PDIV at 6.27 kV. The E_{bd} varies according to the PDIVs, with a mean E_{bd} equal to 5.64 kV/mm. This breakdown field was used for further calculations regarding the expected PDIV. The mean diameter of the micro-glass spheres was found by measuring the diameter of 20 spheres in each test object. A distance of 0.015 mm was deducted to consider the glass sphere wall.

Table 4.2: *PDIV results for the silicone rubber test objects and calculated breakdown field, E_{bd} of the micro-glass spheres for the four silicone rubber tests. The table includes the measured mean diameter, d, of the micro-glass spheres, found by examine the micro-glass spheres in the silicone rubber objects under a microscope.*

Test object	Measured PDIV [kV$_{rms}$]	E_{bd} [kV/mm]	d [mm]
1	5.44	4.89	0.25
2	4.66	4.19	0.30
3	8.60	7.74	0.22
4	6.37	5.73	0.25
Mean values	**6.27**	**5.64**	**0.26**

Figure 4.4 illustrates the resulting PRPD plot of test object 1. The PRPD plot is generated by sampling for 51 seconds, at a voltage of 5.54 kV. The measuring bandwidth was sat to 400±325 kHz. Symmetrical patterns have emerged at the increasing part of the voltage in both half cycles. More details about the test result, PRPD plots from each measurement at PDIV including the reference tests can be seen in Appendix G.
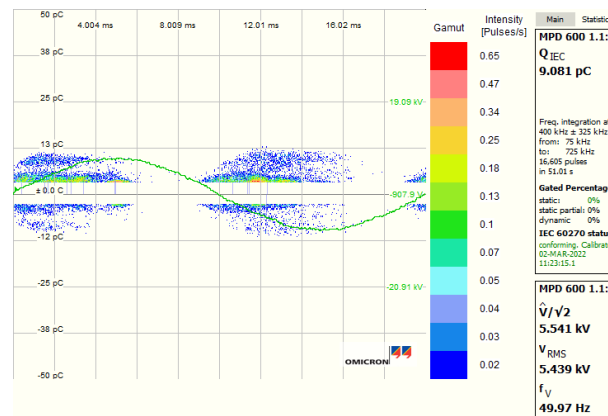
Figure 4.4: *PRPD plot of silicone rubber test object 1 generated by sampling for 51 seconds, at voltage of 5.54 kV. A bandwidth of 400±650 kHz was utilised for the measurement. Symmetrical patterns have emerged in the increasing part of the voltage in both half cycles indicating void discharges.*

4.2.3   Field simulations of a micro-glass sphere in silicone rubber

On the basis of the measured PDIV, field simulations of a spherical glass cavity was conducted in Comsol. An electric potential of 8.87 kV was applied to the test object, corresponding to the peak value of the mean PDIV (6.27 kV$_{rms}$) from the silicone rubber tests. The results of the field simulations of one micro-glass sphere in silicone rubber are illustrated in Figure 4.5. The electric field is plotted as a function of the length from point A to point B. The field inside the micro-glass sphere is 5.29 kV/mm which corresponds well to the calculated mean breakdown field in section 4.2.2.

(a) The electric field in a micro sphere in silicone rubber.

(b) The electric field as a function of length from point A to B.
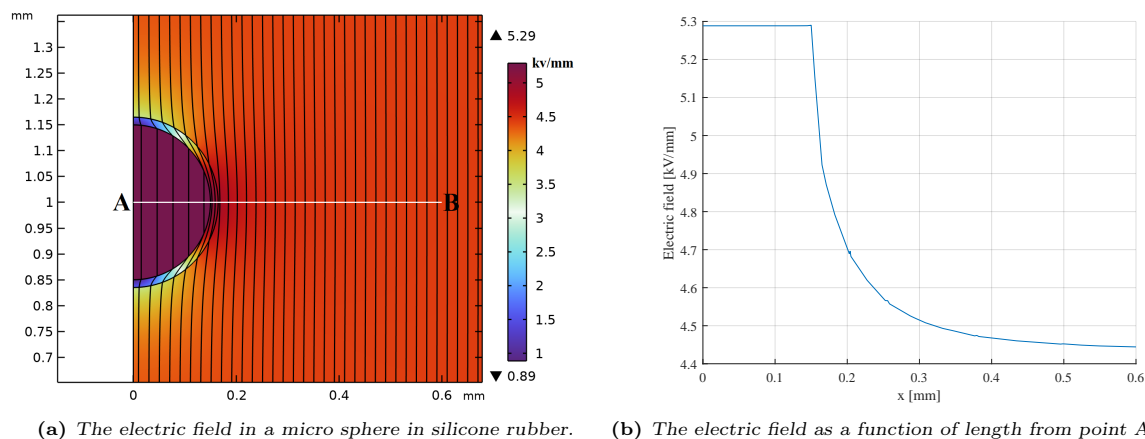
Figure 4.5: *Electric field in an air-filled glass sphere inside a silicone rubber, and the plotted electric field as a function of length (point A to B) applying an electric potential of 8.87 kV.*

4.2.4   Micro-glass sphere implementation in cable insulation

Figure 4.6 illustrate the result of one micro glass sphere that have been cast in epoxy down in the cable insulation. The area with the micro glass sphere have been examined utilising a microscope with a magnifying of 100, which can be seen in Figure 4.6a. The outer diameter of the sphere was measured to be 0.3 mm. This corresponds to an air-filled cavity with a diameter of 0.285 mm if the thickness of the glass wall is deducted. An air bubble has formed in the epoxy having a diameter of 0.17 mm. A photo of the area with the implemented sphere is shown in Figure 4.6b.

(a) Sphere in the insulation through a microscope.

(b) The location of the implemented sphere.
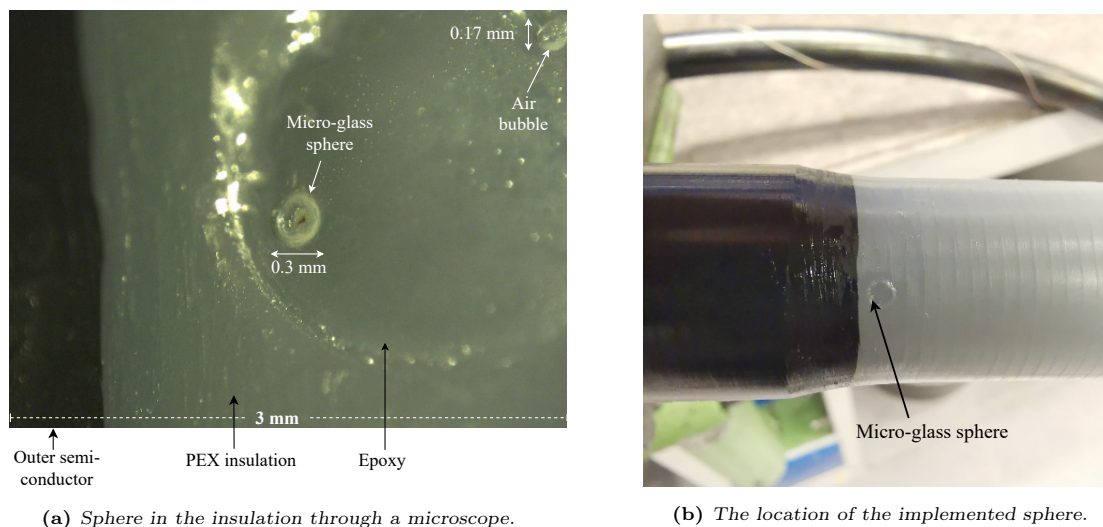
Figure 4.6: *A micro-glass sphere with an outer diameter of 0.3 mm was implemented into the cable insulation using epoxy. An air bubble with an diameter of 0.17 mm have formed during casting. The photo is generated by examine the cable from above with a microscope. Blurriness in the picture is due to movement in the cable while examined under the microscope.*

4.2.5   Expected PDIV of the implemented micro-glass sphere

Based on the calculated breakdown field of 5.64 kV/mm from the silicone rubber tests, the expected PDIV for the one sphere inside the cable insulation was calculated. The calculations resulted in an expected PDIV of 15.46 kV_{rms} for the micro-glass sphere inside the cable insulation. The cavity diameter, the breakdown field and the expected PDIV are summarised in Table 4.3. The calculations and the procedure to find the expected PDIV are described in Appendix H. It is important to emphasise that the calculated PDIV corresponds to the voltage that needs to be applied to the test object (the cable) for PD inception.

Table 4.3: *Expected PDIV of the 0.285 mm micro-glass sphere embedded inside the cable insulation assuming a breakdown field of 5.64 kV/mm. It is important to emphasise that the calculated PDIV corresponds to the voltage that needs to be applied to the test object (cable) for PD inception.*

Cavity diameter [mm]	Breakdown field [kV/mm]	Expected PDIV [kV$_{rms}$]
0.285	5.64	**15.46**

4.3   Sensor test - Partial discharge

To quantify the performance of the copper mesh sensor PD measurements was conducted, first by creating a corona source, and then with the micro-glass sphere embedded into the cable insulation. The results will first and foremost compare the copper mesh sensor to the conventional measuring technique in terms of captured partial discharge activity. In addition, the results will indicate if the PD signals from the micro-glass sphere are reproducible. It is important to highlight that noise signals during the tests complicated the calibration of the copper mesh sensor, thereby the copper mesh sensor is not calibrated at the applied measuring bandwidth. As a consequence, the magnitude of the measured discharges of the conventional measuring technique and the copper mesh sensor differs.

4.3.1   Corona discharges

Two corona tests were conducted. The generated PRPD plots of corona test 1 for the conventional measuring technique and the copper mesh sensor can be seen in Figure 4.7. The PRPD plots was generated for 2 minutes, at a voltage of 3.50 kV. A bandwidth of 400±325 kHz and 4±0.75 MHz was used for the conventional measuring technique and the copper mesh sensor respectively. The conventional measuring technique captured on average almost 5 times more apparent charges than the copper mesh sensor. Analysis data, details regarding the corona test and PRPD plots of both measurements can be seen in Appendix I.1.

(a) *Test 1 - conventional*   **(b)** *Test 1 - copper mesh*
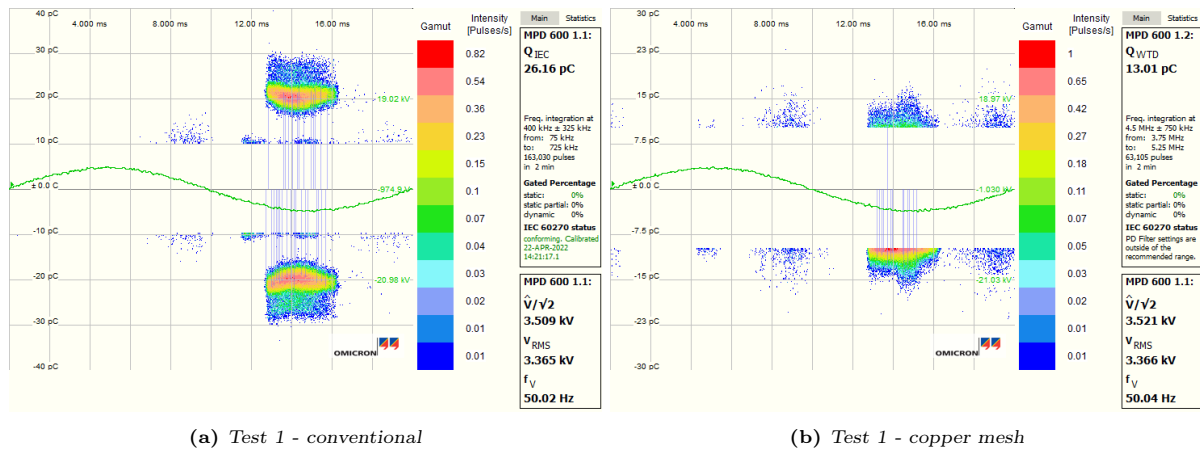
Figure 4.7: *PRPD plots at a voltage of 3.50 kV of the corona measurement conducted simultaneously with the conventional measuring technique and the copper mesh sensor. The PRPD patterns are generated for 2 minutes, at a bandwidth of 400±325 kHz and 4±0.75 MHz for the conventional measuring technique and the copper mesh sensor respectively.*

The PRPD plots from both measuring techniques show discharges of a high amplitude appearing at the voltage crest. A high level of noise signals was observed during the test. Therefore, the PD threshold for both measuring techniques was sat to 10 pC during the analysis. Despite this, additional noise discharges have been captured which can be seen as additional patterns at the voltage increase for both measuring methods.

4.3.2   Void discharges

In total, four successful sensor tests were conducted for the void defect. The resulting PDIV for all measurements can be seen in Table 4.4. The measured PD-activity incepted at a lower voltage value than the expected PDIV at 15.46 kV_{rms}. Test parameters and PRPD plots from each test can be seen in Appendix I.2.

Table 4.4: *Measured PDIV for the four PD sensor tests of the micro-glass sphere.*

Test	PDIV [kV_{rms}]
1	6.96
2	6.83
3	6.46
4	6.12

The PRPD plots from test 4 can be seen in Figure 4.8. The plots are generated by sampling for 6 minutes at 7.58 kV, utilising a bandwidth of the conventional measuring technique at 400±325 kHz, and a bandwidth of the copper mesh sensor of 4±0.75 MHz. A PD threshold of 4 pC and 15 pC was used for the conventional and the copper mesh sensor, respectively. The measured apparent charge magnitude for the two measuring principles differs as the copper mesh sensor was not calibrated at the applied bandwidth. Two unsymmetrical patterns have emerged at the voltage crest for both the conventional and the copper mesh sensor. The discharges incepted simultaneously in both half periods, and the magnitude of the measured discharges increased with increased voltage. The results of the comparison of the pulse repetition rate shows that the copper mesh sensor on average captured 2.84 % more discharges than the conventional measuring technique.

(a) *Conventional*   (b) *Copper mesh sensor*
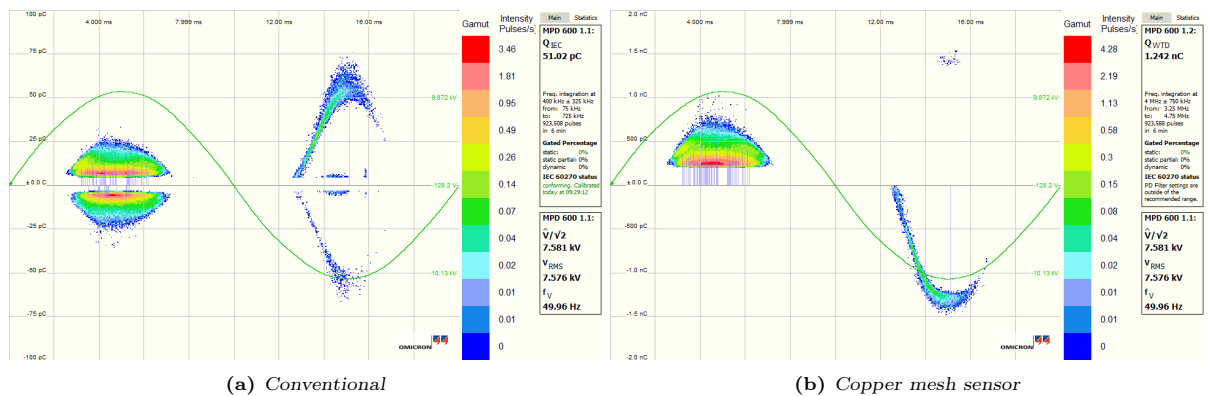
Figure 4.8: *PRPD plots at a voltage of 7.58 kV of the void defect measured with the conventional measuring technique and the copper mesh sensor. The PRPD plots are generated for 6 minutes, at a bandwidth of 400±650kHz and 4±1.5 MHz for the conventional measuring technique and the copper mesh sensor, respectively.*

The obtained results was only captured utilising the conventional measuring technique simultaneously as the copper mesh sensor. Several experiments, besides from the PD sensor test, was conducted. Before the PD sensor test, preliminary measurements utilising only the conventional measuring technique were performed to analyse how the system behaved. No discharges (except noise signals) was captured during these tests, although the voltage was increased to above the expected PDIV, and up to 30 kV. The same applied for conventional PD measurements conducted after the PD sensor test. These tests were performed to examine if the obtained signals were reproducible or not.

4.4   Field simulations of the stress cone

To analyse how the micro-glass sphere affects the field inside the test object and to examine the field inside the micro-glass sphere, field simulations in Comsol was conducted. An electric potential of 21.86 kV was applied to the geometry in the simulation, which corresponds to the peak value of the expected PDIV of 15.46 kV$_{rms}$. Figure 4.10 illustrate the results of the field simulations of the stress cone and cable with the micro-glass sphere embedded inside the insulation. The red box marks the segment which was used for closer analysis.
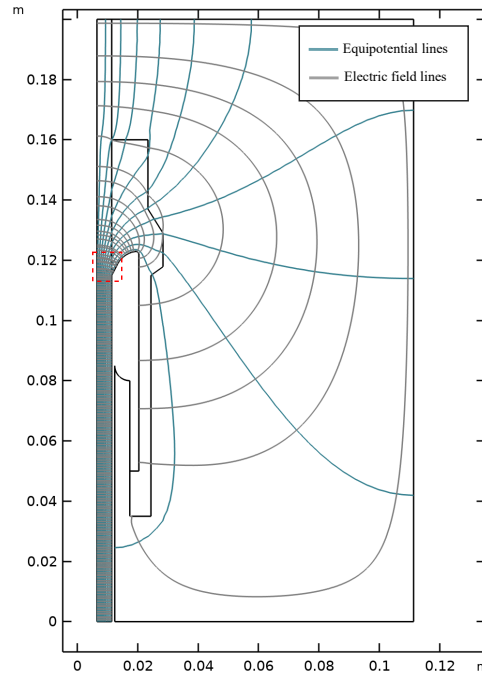
Figure 4.9: *Field lines (grey) and equipotential lines (blue) inside the stress cone and the cable with a micro-glass sphere embedded inside the cable insulation. The red box marks the segment used for closer field analysis which can be seen in Figure 4.10.*

Simulated electric field (streamlines) in the stress cone can be seen in Figure 4.10. The field has been plotted along a streamline, right through the spherical cavity, to the beginning of the semi-conducting layer inside the stress cone. The start point and end point is marked with A and B respectively in Figure 4.10a. The comparison of the field with and without the void defect, as illustrated in Figure 4.10b, illustrate a distinct strengthening of the field in the x-parameter which correspond to the location of the void (0.0097 - 0.0103 m) with the void present inside the insulation. The field inside the micro-glass sphere in this region is 4.55 kV/mm and decreases linearly to 4.40 kV/mm. Two drops in the field strength right before and after the air-filled void are due to the glass-wall of the cavity.

(a) *The field was plotted along the streamline from A to B.*

(b) *Electric field as a function of length.*
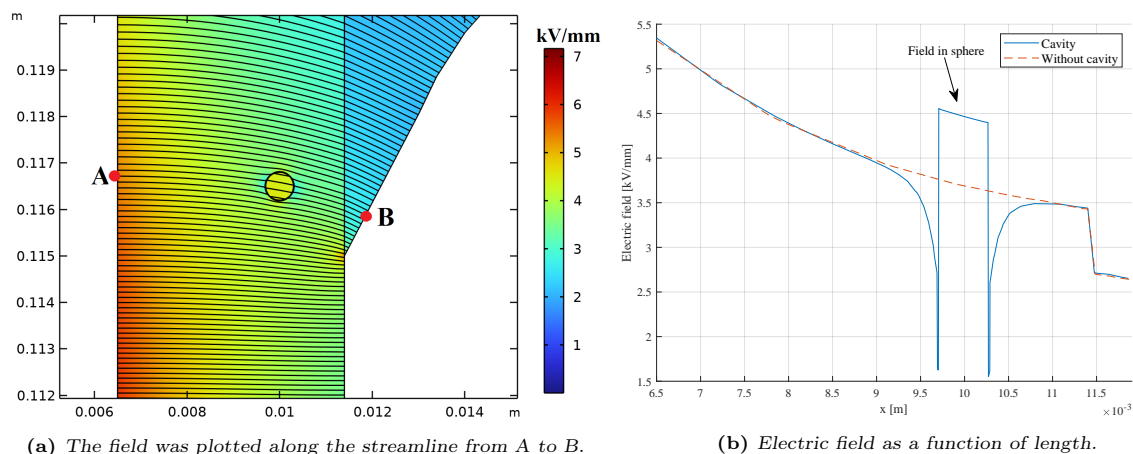
Figure 4.10: *Field analysis of the micro-glass sphere inside the cable insulation. An electric potential of 21.86 kV was applied to the model in Comsol. The field has been plotted along a streamline from the cable insulation (point A) to the beginning of the semi-conductor of the stress cone (point B).*

The field inside the micro-glass sphere is lower than the calculated breakdown field of 5.64 kV/mm. By increasing the electric potential by 1 kV the field inside the sphere increases by 0.2 kV/mm. To obtain a field inside the micro-glass sphere equal to or above the breakdown field, an electric potential of 29 - 30 kV (20.5 - 21.21 kV_{rms}) must be applied to the geometry.

5 Discussion

The most important aspects of the presented results will be discussed in coherence with the provided theory in the following section. The section is divided into five parts. The performance of the copper mesh sensor will be discussed in terms of putting the FRA-measurements in context with the PD sensor test, including a comparison of the five sensor proposals, detection sensitivity, the effect of C_s and R_s, and the performance of the copper mesh sensor compared to the conventional measuring technique. Further, the generation of the spherical void defect will be evaluated. This evaluation includes an assessment of the silicone rubber tests, the defect implementation procedure, and the measured void discharges from the PD sensor test. The field simulations of the spherical void inside the cable insulation will also be discussed in coherence with the artificial void defect. Lastly, general aspects of the procedure, laboratory mistakes, and errors will be evaluated.

5.1 Sensor performance

As can be seen from the results of the FRA measurements in Figure 4.1, the frequency response for all sensor proposals (except case 5) increases with increasing frequency. It is uncertain how the systems will behave at frequencies above 10^8 Hz. A better response may be obtained, or the gain may decrease due to higher frequencies. To obtain a more comprehensive FRA, the sensor proposals could have been tested at different frequency domains than at the one tested (1 kHz to 100 MHz). For instance, begin at a higher start frequency than 1 kHz and end at a frequency above 10^8 Hz. By that, an optimal bandwidth range, and perhaps a more accurate one, for the sensor proposals could have been achieved.

The bandwidth of the copper mesh sensor utilised during the PD sensor test is not in accordance with the *optimal* bandwidth found in the FRA measurements, or in other words, the frequency range with the highest gain. As mentioned in theory, the attenuation of the output signals should be as low as possible to obtain a good response of the system. A closer look at the FRA measurements of case 1 is given in Figure 5.1. The bandwidth of the copper mesh sensor (4±0.75 MHz) utilised during the PD sensor test is marked in blue. Based on these measurements, the sat bandwidth during the PD sensor test is not in the range where the signal output is at its highest. A better sensitivity of the copper mesh sensor than the one obtained (compared to the conventional measuring technique) could have been achieved by utilising a higher centre frequency for the PD sensor test.
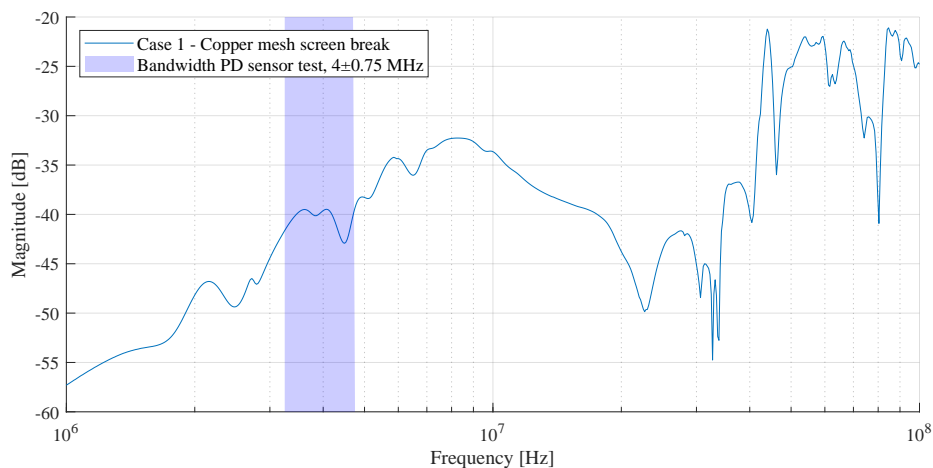
Figure 5.1: *A closer look at the FRA measurement of sensor case 1. The bandwidth utilised for during the PD sensor test (4±0.75 MHz) is marked in blue. The plot is based on the same data as the FRA plot given in Figure 4.1.*

Meanwhile, higher measuring frequencies may complicate PD measurements. As mentioned in theory, a typical PD pulse has a rise time less than one nanosecond and a pulse width of several nanoseconds, which implies a frequency-domain of MHz. In addition, according to IEC a bandwidth in the kHz range is recommended for PD measurements, which is a bandwidth based on thorough PD measurements and analysis. As the frequency increases, the attenuation of PD signals with distance becomes more serious. If the PD signal has to travel far, the signal can be damped and thereby not detected by the sensor. Higher measuring bandwidths may therefore fail to couple the energy of the PD signals. Attenuation of PD-signals has not been accounted for in this thesis but may be further examined to design an optimal sensor-system. On the other hand, the idea of the copper mesh electrode is to measure directly over the most probable location of a defect inside a termination. By that, the problem of signal attenuation may be limited.

The bandwidth of the copper mesh sensor was chosen based on the relatively high noise level during the PD sensor test. The bandwidth was adjusted to the frequency range with the lowest noise level to avoid utilising a high PD threshold for the copper mesh sensor. A high PD threshold may affect the results in terms of truncating actual PD-signals. It is also worth mentioning that the limitations in Omicron, constrain the applicable bandwidth. As a consequence, a higher measuring bandwidth may not be possible.

The results of the PD sensor test could have been different if choosing to focus on one of the other sensor principles than sensor case 1. For instance, noise signals during the PD sensor test could have been reduced by applying a coil or a transformer in the copper mesh gap as described in sensor case 2 and case 3, respectively. Thereby, a higher sensitivity of the copper mesh sensor could have been achieved. Sensor case 4 may also be a good alternative to reduce noise as this was the only proposal not subjected to noise during the FRA measurements. Sensor proposal number 5 is interesting because the gain of this sensor is higher than the four other proposals at lower frequencies. In addition, the highest gain of this sensor proposal is in the frequency area corresponding to the utilised bandwidth during the PD sensor test.

Nevertheless, sensor case 1 may be the best alternative for the proposed sensor accounting for the planned position of the PD sensor inside the termination. Both case 2 and case 3 may not be suited as it requires changes to the design of the high-voltage termination in terms of inserting new components. The same applies for sensor case 4. Sensor case 1 requires minimal changes to the design and may therefore be well suited for the PD sensor system. Sensor case 5 may not require any changes to the design by excluding the copper mesh around the stress cone and measuring PD activity outside of the termination. However, as the stress cone area is the most vulnerable to failure, case 5 may fail to measure discharges directly over the source if there is no copper mesh coupling in this area.

5.2 Effect of stray capacitance and -resistance

The results of the analysis of both the stray capacitance, C_s, and stray resistance, R_s are in coherence with the provided theory. As illustrated in the results from the analysis in LtSpice (section 4.1.2), the stray capacitance, C_s, should be as small as possible to obtain the lowest attenuation. Capacitances, in general, are proportional to the electrode surface and the permittivity in the medium surrounding it and inverse proportional to the distance between the electrodes. The stray capacitance can be reduced by having a long distance to earth and reducing the size of the sensor electrode. However, this will affect the copper mesh measuring circuit, and it will not be easy to obtain this without adjusting other parameters. Another possibility, is to reduce the permittivity of the surrounding material. However, this will not be possible as it will be the same as changing the permittivity of air (or silicone oil).

In contrast to the C_s, the stray resistance should be as high as possible. R_s is, among other factors, determined by the gap distance of the copper mesh electrode and the ground copper mesh at the cable. The results of varying R_s can thereby help determine the gap length of the electrode and the ground screen. In these analysis, it is assumed that R_s is independent of frequency. However, in practice, it is likely that R_s increases with frequency because of skin effect, meaning that the copper mesh sensor may perform better at higher frequencies.

C_s and R_s could be measured to gain a better understanding of how the system is affected by these parameters. However, the results indicate that the value of R_s does not have a considerable significance at high frequency levels as the curves for R_s equal to 10, 100, and 1000 Ω appear to level out, as illustrated in Figure 4.2b. On the other hand, if R_s is closer to zero, it may have a significant impact on the output signals. The opposite applies to changing values of C_s. The curves have the same amplitude for frequencies ranging from 0.1 MHz to almost 10.2 MHz, which can be seen in Figure 4.2a. The same amplitudes imply that the performance of the copper mesh sensor may not be strongly affected by the value of C_s in this frequency range.

5.3 Detection sensitivity

The sensitivity analysis results illustrate that the copper mesh sensor can measure apparent charges down to 5 pC. This value is higher than the obtained sensitivity of 3 pC of the capacitive copper strip sensor presented in Section 2.3.3. However, the sensitivity may be difficult to quantify accurately. As mentioned in theory, the sensitivity of a PD measuring system depends on the signal amplitude and the noise level. This dependency was observed during the sensitivity analysis, as noise signals superimposed the lowest injected charge signals. In addition, the noise signals limited the utilised bandwidth of the copper mesh sensor. Thereby the analysis was only conducted at one constant bandwidth. The sensor may measure lower apparent charge values at increased or decreased bandwidths. The measured noise are probably due to induced noise in the earthing network or noise from other experiments in progress nearby. Noise-reducing actions could have been performed to measure the actual sensitivity more accurately.

The copper mesh sensor measures injected charges of a 2 to 3 pC lower magnitude than the conventional technique for injected charge values of 5, 10 and 50 pC as given in Table 4.1. The difference may be due to alternation of the pulse in the cable. In a high voltage dielectric cable, the characteristics of a charge pulse depend on the distance from the source and the measuring point. The injected signal may have been damped through the cable as a consequence of the frequency loss in such a cable. However, the pulse from the calibrator is injected at the same spot for all magnitudes, and the copper mesh sensor was placed at the same location during the entire sensitivity analysis, which indicates that the measured pulse should change. Therefore, the difference in the measured charge may be due to the bandwidth utilised for the copper mesh sensor during the sensitivity analysis (16±0.75 MHz), which is outside the recommended range stated by the IEC. Additional sensitivity analysis could have been performed utilising different bandwidths of the copper mesh sensor to obtain a basis of comparison. and perhaps an explanation as to why the copper mesh sensor measures lower injected charge values.

As illustrated in Figure 4.8, there is a difference in the magnitude of the measured discharges for the conventional measuring technique and the copper mesh sensor during the PD sensor test. The difference in measured magnitude is because the copper mesh sensor was not calibrated at the applied bandwidth. As mentioned in theory, calibration is an essential part of the PD measurements, determining the scale factor of the PD measuring system. Accurate PD magnitude is necessary as it can indicate the rate of dielectric deterioration. Similar magnitudes could have been obtained if the copper mesh sensor had been calibrated at the applied bandwidth. A similar charge magnitude could also be achieved by calculating, for instance, correlations factors between the two measuring techniques. However, noise signals during the PD sensor test complicated the calibration procedure, as the calibration pulse was superimposed by fluctuating noise signals. Superimposition is a good example of how noise can be a limiting factor in PD measurements. Noise reduction actions could have been considered to obtain similar discharge magnitudes.

There is a difference in the captured apparent charge comparison for the corona defect test and the void defect. The copper mesh sensor measured five times less apparent charge than the conventional measuring technique for the corona test. One reason to explain this can be the attenuation of the corona signals through the cable. The high difference in the detection sensitivity may also be due to noise signals of a higher magnitude than the PD threshold captured by the conventional measuring method.

Meanwhile, the copper mesh sensor measured on average 2.84% more apparent charge for the void defect. For the void defect, the copper mesh sensor measured PD activity more locally than the conventional measuring technique, which may explain the higher sensitivity. This sensitivity is obtained even though the PD threshold of the copper mesh sensor was relatively high compared to the conventional measuring technique. However, the PD threshold is assumed not to be of importance as the magnitude of the measured discharges differs between the two measuring methods.

5.4 PDIV testing of silicone rubber

The measured PDIVs of the spheres in silicone rubber deviate from the calculated PDIVs, taking the measured mean diameter of the micro-glass spheres into consideration. According to the calculated PDIV as plotted in Figure 4.3, the PDIV should be between ~7 kV and ~8 kV for all test objects according to the measured mean diameter. However, none of the test objects resulted in a PDIV in this range, as seen in Table 4.2. There may be several reasons to explain this. For instance, the pressure inside the micro-glass spheres is uncertain. In the PDIV calculations, a pressure of 1 bar was assumed. The pressure inside the micro-glass spheres may be lower than that, and therefore the calculations of the PDIV at different cavity diameters may not be valid.

There is also an uncertainty in the measurement of the mean diameter. The diameter of a random sample consisting of 20 micro-glass spheres was measured under a microscope. This sample may not represent the actual mean diameter of micro-glass spheres in the silicone rubber moulds. In addition, the mean diameter may not be representative of the micro-glass spheres under the electrode area. Hence the PDIV measurements may have been conducted over spheres with a higher or lower mean diameter. The spheres could have been filtered into different sizes before being cast into the silicone rubber to obtain an overview of the cavity diameter. By that, greater accordance between the calculated and the measured PDIV could have been achieved.

The measured PD activity from the silicone rubber tests may not originate from the micro-glass spheres. First and foremost, the measured PDIV deviates from test object to test object, even though the measured mean diameter is relatively similar. However, this might be due to the uncertainties of the measured diameter, as discussed above. Secondly, the utilised silicone rubber was somewhat viscous. Consequently, the A and B components of the silicone rubber may not have been adequately mixed, and voids inside the silicone rubber can have been created. The measured PD activity might stem from such voids. Although, if voids have been formed in the silicone rubber, PD activity could have been expected from the reference test as the same silicone rubber mixture was used to create these objects.

5.5 Evaluation of defect implementation

One air bubble formed in the epoxy during casting, as can be seen in the results of the defect implementation in Figure 4.6a. Air bubbles were attempted to be avoided as the epoxy mixture was sat in a vacuum chamber before being injected into the insulation hole. It is assumed that the air bubble formed during the casting process when the micro-glass sphere was placed in the epoxy. The casting process could have been more carefully performed. For instance, a section of the cable could have been put in a vacuum during the curing time. By that, air bubbles would have been retracted from the cast, and other defects which may lead to PD can be excluded.

It is also uncertain that more than one air bubble formed during the casting process. The test object (the cable) was examined under a microscope, but because of the size of the cable, it was difficult to hold it still and examine the epoxy hole from different angles. The preliminary experiments for defect implementations showed that several air bubbles had formed during casting, strengthening the possibility of more than one air bubble in the test object. However, the air bubbles formed during the preliminary experiments had a smaller diameter than the micro-glass sphere, which is also the case for the air bubble formed in the test object during defect implementation. Therefore, and according to theory, it can be assumed that the air bubbles have a higher inception voltage than the micro-glass sphere, thereby not affecting the PD results.

Additional PD activity due to the air bubble was expected during the PD measurements. However, PD-activity at high voltage levels was not measured. One reason to explain this can be that the air bubble was open towards the exterior and filled with silicone grease when refitting the stress cone over the cable. As mentioned, a clear microscope picture of the air bubble was not obtained. If the cable was examined from different angles, it could reveal if the location of the air bubble was close to the surface and if the sphere was exposed to the exterior.

Micro-glass spheres may not be suited to create an artificial void defect. First and foremost, the spheres are microscopic and difficult to control, thereby challenging to implement inside the cable insulation. Secondly, the spheres may break when exposed to pressure. Several spheres broke when picked up by the pair of tweezers. However, glass has the benefit of having a high dielectric strength. Therefore, in theory, a suitable material for creating an artificial void defect.

Other alternatives of creating an artificial defect to obtain reproducible PD signals could have yielded more control of the artificial defect. For instance, other procedures, such as the mica defect, could have been a better option for a "stable" cavity defect. This defect might have yielded better control during the defect implementation because the object to be handled is bigger than the micro-glass sphere. In addition, more control of the cavity size could have been achieved. However, this defect requires a larger drilled hole in the cable insulation, which may cause additional discharges if not sealed properly.

5.6 Assessment of the measured void discharges

The source of the measured PD activity from the PD sensor test may not stem from the implemented micro-glass sphere. There are several reasons which underline this statement. First and foremost, the measured PDIV of the void defect was lower than expected. An expected PDIV of 15.46 kV was calculated based on the silicone-rubber tests. However, the PD sensor test resulted in a PDIV ranging from 6.12 to 6.96 kV. Secondly, the phase position of the measured discharges deviates from typical PRPD patterns for void defects. The obtained pattern should be shifted to the left towards the zero crossing to correspond to the theory. In addition to the phase position, the measured signals have no phase symmetry, which was expected as the embedded micro-glass sphere is spherical. Lastly, the obtained PD-activity is not reproducible. PD-activity was only obtained during the four PD sensor tests when the micro-glass sphere was embedded inside the cable insulation. When measuring with the conventional measuring technique alone, both before and after the PD-sensor test, no activity was obtained.

PD-activity is measured with a known defect inside the cable, but, as mentioned, there is reason to believe that the measured activity stems from another source. The high amplitude of the measured discharges may correspond to surface discharges. However, the PRPD pattern and the continuous occurrence of the discharge activity deviate from generally intermittent surface discharges. Another source of the measured discharges can be the boundary surface of the cable and stress cone. If the semi-conductor of the cable was not carefully peeled, voids might have formed in this intersection. A third source can be discharges occurring towards the electrode. The discharges may also be due to unknown defects inside the cable or cable termination. However, the test setup system was measured PD free up to 30 kV in advance of the defect implementation, which makes unknown defects to be unlikely.

Another theory is that the semi-conductor inside the AIN slip-on stress cone was damaged due to the stress cone removal and re-installation. Voids or slits may have formed due to the removal and refitting, which may be the reason for the measured discharges. However, this is not likely as more PD activity could have been expected, assuming the slit or void has a much larger size than the micro-glass sphere. In addition, it is assumed that the stress cone was exposed to minor damage as generous amounts of silicone grease were applied to the cable surface during the procedure.

Voids in the silicone grease in-between the cable and the slip-on stress cone may explain the measured discharges. A void in the silicone grease may correspond well to the behaviour of the measured discharges and could have been formed as a consequence of test setup changes, for instance, when installing the copper mesh sensor around the stress cone. If the formed void is relatively large compared to the micro-glass sphere, it may explain why the PDIV is lower than expected. In addition, the void formed by the silicone grease may be none uniform which may explain the unsymmetrical PRPD patterns. The silicone-

grease void may have collapsed or changed due to alternations to the test setup after the PD sensor test. Changes of the void due to alternations can explain why the obtained signals were not reproducible. Nevertheless, it is important to mention that the discharge magnitude increased with increased voltage. Such behaviour is typical for void defects, and an argument that the measured PD-activity stem from a void defect inside the system.
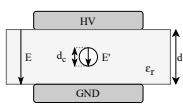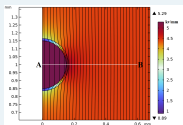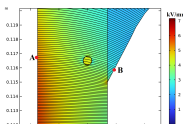
5.7 Failed inception of the micro-glass sphere

Several reasons can explain why the micro-glass sphere did not incept during the PD sensor test. One theory is that the sphere was damage during the epoxy casting procedure. As mentioned before, it was difficult to examine the micro-glass sphere embedded inside the cable under the microscope, so it is uncertain that the sphere is utterly intact inside the epoxy. If there was a crack in the sphere, the void might got filled with epoxy, eliminating the air-filled cavity.

Another reason can be that the pressure inside the sphere is lower than the assumed pressure of 1 bar. As mentioned in theory, and as illustrated in Figure 2.7, the Paschen's curve is characterised by high breakdown voltages at very low (and very high) $p \cdot d$ values. If the pressure inside the sphere is low, the PDIV may be higher than assumed. The pressure may also be close to vacuum, which indicates an even higher breakdown voltage. Consequently, the applied voltage has to be very high to obtain void discharges. A very high voltage might yield the break out of other types of discharges such as surface.

The expected PDIV of the spherical void may be higher than calculated. An overview of the calculated field and simulated fields are given in Table 5.1. The values in this table are the same presented in the result section. Based on the PDIV test of micro-glass spheres cast in silicone rubber, with a mean PDIV of 8.60 kV_{peak}, the breakdown field of the spheres was calculated to 5.64 kV/mm. Applying the mean PDIV as the electric potential in Comsol for the silicone rubber geometry resulted in a field that corresponded well to the calculated breakdown field, as seen in section 4.2.3. An expected PDIV of 15.46 kV_{rms} (21.86 kV_{peak}) for the micro-glass sphere embedded in the cable insulation was calculated based on the calculated breakdown field. However, when applying an electric potential equal to the expected PDIV in Comsol for the stress cone simulations, the field inside the void is lower than the calculated breakdown field.

Table 5.1: *Summarised field calculation and simulations with the utilised applied voltage. Applied voltage relates to the voltage utilised for the calculations and for the simulations in Comsol. The values are the same as given in the results section.*

	E [kV/mm]	Applied voltage [kV$_{peak}$]
PDIV test of the silicone rubber objects	5.64	8.60
Field simulation of one sphere in silicone rubber	5.29	8.60
Field simulation of one sphere in insulation	~4.50	21.86

The expected PDIV calculations do not account for the slip-on stress cone, which may explain why the simulated field is lower than the breakdown field. As explained in theory, the stress cone operates as a field grading component and will influence the field in the region where the micro-glass sphere is localised. This field grading is well illustrated in the resulting field simulations of the stress cone in Figure 4.9. As a consequence, the field of the sphere may not have reached the breakdown field during the PD sensor test. Additional analysis in Comsol of the stress cone geometry indicated that the field inside the sphere increases by 0.2 kV/mm for each 1 kV increase in the electric potential. Based on this, an electric potential of 29-30 kV (20.5 - 21.21 kV$_{rms}$) must be applied to the geometry/test object to obtain a field equal to or above the breakdown field. Consequently, the expected PDIV may be higher than the one calculated. However, no PD activity was captured outside the PD sensor test even though the voltage was increased up to 30 kV$_{rms}$.

Four measurements with somewhat similar PDIVs and PRPD patterns was obtained during the PD sensor test, and the stochastic nature of PD might explain why the micro-glass sphere only incepted during these tests. As mentioned in theory, PDs are stochastic variables. The probability that PD signals from one source appear similar independent of the test procedure is low, which might explain why discharge results from the void were only obtained when performing the copper mesh sensor test. Changes due to alternations or switching of measuring procedure may have affected the PD source, thereby affecting the obtained results.

The probability of measuring void discharges could have been increased if more than one micro-glass sphere had been cast into the cable insulation. The PD sensor test for the artificial void depended on only one micro-glass sphere, which was randomly chosen from the number of spheres available. More than one micro-glass sphere can be cast into the cable insulation for similar defect implementation procedures. In this way, the probability of obtaining void discharges might increase, as there is a higher chance of inception as more voids are present. However, in this way, there is less control over which sphere that incepts, and the PD characteristics of the defect may not be reproducible which was the goal of the generation of the spherical void.

5.8   General

The focus of the thesis has been slightly shifted throughout the project. More analysis and optimisations of the copper mesh sensor could have been performed in terms of detection sensitivity, localisation of sensor electrode, or connection principles. However, such analysis was not carried out because of the failed defect generation. The focus was shifted towards the spherical void to find explanations as to why the sphere did not incept. If the micro-glass sphere functioned as a void defect with reproducible PD characteristics, a more thorough analysis of the copper mesh sensor could have been obtained.

A weakness of the conducted experiments is the manually adjusted voltage. A variac was utilised to manually increase the voltage step-wise during the PD tests (silicone rubber tests and the PD sensor test). It is difficult to increase the voltage with even intervals with this approach. Consequently, the experiments considering PD measurements have not been performed equally for the different tests or test objects. For similar experiments, automatic voltage adjustment could be applied to gain more similar voltage curves for each experiment.

It is unknown how the copper mesh sensor will behave at higher voltage levels than tested in this thesis. A model with a 12 kV cable was made in the conducted experiments. It is uncertain whether the experiments conducted in this thesis are directly transferable to higher voltage levels or oil-filled 420 kV cable terminations. The sensor principle is only tested up to ∼ 30 kV in an air-insulated environment. Higher voltage levels and an oil-insulated system may affect both the design of the sensor and the behaviour of the measured signals (PD). However, field regulation is similar at higher voltage levels, and it is assumed that the air-insulated model does not deviate to a large extent from oil-insulated systems. Therefore, this work can be used as a basis for further analysis and a proof of concept. Nevertheless, additional testing and optimisation of the sensor proposal are necessary to obtain a system that can be utilised in an oil-filled termination.

This master thesis is primarily experimental, which has affected the results. It is crucial to consider unplanned mistakes and laboratory errors when planning an experiment. Noise problems in Omicron and delays regarding test equipment or setup could have been more carefully considered. However, it is not easy to control everything that may occur during a laboratory experiment.

6   Conclusion

Based on both the FRA measurement and sensor design, sensor case 1 is the most suited sensor proposal for the proposed PD sensor. This PD measuring principle requires minimal changes to the design of the high voltage termination, and the frequency response of the sensor deviates to a small degree from the other measuring proposals. A bandwidth in the range from 1 MHz to 10 MHz should be chosen for the sensor based on measurements conducted in this thesis. Higher measuring bandwidths may complicate PD measurement because of signal attenuation.

C_s should be as low as possible, and R_s as high as possible to obtain the highest gain of the copper mesh sensor. These variables should be measured to gain a better understanding of how the system is affected by these parameters. The copper mesh sensor is able to measure apparent charge values down to 5 pC. Simultaneously, the sensitivity analysis was affected by noise signals, and it is reason to believe that the copper mesh sensor can measure charge values of a lower magnitude in a noise-free environment.

The copper mesh sensor have proven to be efficient when measuring locally and directly over the location of the defect. As illustrated in the results, it measured more apparent charge values for the void defect than the conventional measuring technique. The performance of the sensor is, however, dependent on the source of PD. The sensitivity of the sensor, compared to the conventional measuring technique, decreased drastically when measuring corona discharges.

The measured PD activity in the silicone rubber tests are due to the micro-glass spheres. The calculated breakdown field corresponds well to the simulated field in Comsol. Simultaneously, the measured PDIV in the silicone rubber tests do not correspond to the measured mean diameter of the micro-glass spheres embedded inside the silicone rubber. Thereby, the measured mean diameters are not representative of the spheres causing PD. The spheres could have been sorted according to size before casting to obtain control of the diameter of the spheres cast in each of the silicone rubber moulds.

Even though the spheres incepted during the silicone rubber tests, the PD activity in the PD sensor test for the void do not originate from the implemented micro-glass sphere. An unsymmetrical PRPD pattern, the phase position of the measured discharges, and the low inception voltages explains why. In addition, the measured discharges was not reproducible. Several reasons can explain why the micro-glass sphere did not incept. One potential reason is that the pressure inside the micro-glass sphere is lower than the assumed 1 bar. As a consequence, the generation of a spherical void with reproducible PD characteristics was not successful. The measured discharges during the PD sensor test is probably due to an unsymmetrical void formed in the silicone grease during test setup alternations.

Thorough field simulations of the stress cone with a micro-glass sphere embedded inside the cable insulation was successfully conducted. These simulations illustrates that the expected PDIV of the micro-glass sphere is higher than the one calculated. The reason for this is that the calculations for the expected PDIV did not consider the effect of the slip-on stress cone. The voltage was, however, increased above the expected PDIV and up to 30 kV without any discharge activity taking place (except during the PD sensor test).

The copper mesh sensor have proven to be a good alternative to PD measurements, and the concept works. However, the proposed sensor is only at a preliminary stage, and this thesis can be utilised as a proof of concept of the PD measuring principle. Several tests and experiments are necessary to obtain a full-functioning PD sensor that can be implemented inside a 420 kV oil-filled termination.

This thesis can be used as a basis for creating an artificial void defect. Other procedure for defect implementation should be evaluated if similar experiments are to be executed. Although, it is important to emphasise that micro-glass spheres may not be completely excluded, as discharge activity stemming from the spheres was obtain during the silicone rubber tests. More consideration in terms of size and shape of the sphere should be stressed if the procedure is to be repeated.

7   Further work

Based on the experiments conducted in this thesis, proposals for further work will be presented. First and foremost, the sensor proposal can be more thoroughly tested in terms of FRA and sensitivity analysis. Changing the position or the shape of the copper mesh electrode, in addition to connection principles may influence both the frequency response and the sensitivity of the sensor. Noise reducing actions should be further investigated to create a system that is able to filter noise signals. The sensitivity of a PD measuring system depends on the signal amplitude and the noise level. Therefore, to design a system for maximum sensitivity, the bandwidth for optimum signal-to-noise ratio can be further investigated.

The functionality of the copper mesh sensor may be completely different at higher voltage levels. The sensor may therefore be tested in a full scale termination model for more accuracy compared to the 12 kV model in this thesis. In addition, as the sensor is to be placed inside an oil-filled termination, the behaviour and characteristics of PD in silicone-oil should be thoroughly examined.

The sensitivity of the copper mesh sensor, relative to other defects than void discharges, can be examined. By that, an overall sensitivity of the sensor can be achieved. Extended laboratory tests can be conducted to obtain data for potential machine learning of the proposed sensor. By this, a database of defect recognition can be implemented. However, to do so, automatic control of the variac in the test circuit should be implemented to obtain even voltage intervals.

Other aspects in addition to sensitivity relevant to defects are of importance when designing a PD sensor. This includes the ability to withstand service stresses such as lightning and switching impulses. Thorough withstand testing can be exploited to optimise the design of the sensor. The design, in addition to optimal positioning, of the sensor can also be further investigated which may provide suitable means for sensitivity analysis. Another possibility is to test the system until breakdown by creating a serious defect and examine how the system behaves.

References

[1]   Forskningsrådet. *Smart On-Line Health Assessment of Cable Terminations*. URL: `https://prosje ktbanken.forskningsradet.no/project/FORISS/318007?Kilde=FORISS&distribution=Ar&ch art=bar&calcType=funding&Sprak=no&sortBy=date&sortOrder=desc&resultCount=30&offse t=210&TemaEmne.1=FNs+B\%C3\%A6rekraftsm\%C3\%A5l` (visited on 01/30/2022).

[2]   D. Denissov et al. *On-Line Partial Discharge Diagnostics for Cable Terminations*. Jan. 2007. URL: `https://www.researchgate.net/publication/228447666` (visited on 02/05/2022).

[3]   SINTEF. *SmartACT - Smart On-Line Health Assessment of Cable Terminations*. Apr. 26, 2021. URL: `https://www.sintef.no/en/projects/2021/smartact-smart-on-line-health-assessm ent-of-cable-terminations/` (visited on 01/30/2022).

[4]   CIGRE Study Committee B1: Insulated Cables. *Accessories for HV and EHV Extruded Cables, Volume 1: Components*. 2021. URL: `https://link.springer.com/referencework/10.1007/978- 3-030-39466-0#about` (visited on 03/15/2022).

[5]   CIGRE Working Group B1.10. *Update of Service Experience of HV Underground and Submarine Cable Systems*. Apr. 2009.

[6]   B.T. Phung, T.R. Blackburn, and Z.Liu. *Acoustic Measurements of Partial Discharges Signals*. May 10, 2014.

[7]   Lars Lundgaard. *Measurement of Partial Discharges, NTNU-kurs*. Aug. 2020.

[8]   V. Fuster A. Rodrigo P. Llovera and A. Quijano. *High Performance Broadband Capacitive Coupler for Partial Discharge Cable Tests*. Apr. 13, 2013. URL: `https://ieeexplore.ieee.org/document /6508750` (visited on 04/18/2022).

[9]   Erling Ildstad. *ELK-30, Seminar 2, Destructive tests and laboratory sample analysis*. Sept. 2, 2021.

[10] INMR. *Condition Assessment of High Voltage Cable Terminations*. Mar. 4, 2022. URL: `https://w ww.inmr.com/condition-assessment-of-high-voltage-cable-terminations-3/` (visited on 03/15/2022).

[11] Elise Tajet Høigård. "On-line Condition Assessment of 420 kV Terminations - design and develop- ment of PD sensors, Specialisation project in TET4510". Dec. 21, 2021.

[12] Erling Ildstad. *TET4160 Insulating Materials for High Voltage Applications*. Aug. 2020.

[13] Andreas Küchler. *High Voltage Engineering*. 2018.

[14] Erling Ildstad. *Compendium in TET4195 - High Voltage Equipment, Cable part*. 2021.

[15] H. Borsi I. Fofana and E. Gockenbach. *Fundamental Investigations on Some Transformer Liquids under Various Outdoor Conditions*. Dec. 2001. URL: `https://ieeexplore.ieee.org/stamp/stam p.jsp?arnumber=971463` (visited on 03/03/2022).

[16] Espen H. Doedens. *Topographical Impact on Space Charge Injection, Accumulation and Breakdown in Polymeric HVDC Cable Interfaces*. 2020. URL: `https://research.chalmers.se/en/publicat ion/519873` (visited on 02/22/2022).

[17] NEK. *IEC 60270, High-voltage test techniques, Partial discharge measurements*. Nov. 2015.

[18] Torstein Grav Aakre. *Partial Discharges in Voids at Variable Voltage Frequency and Temperature*. 2020. URL: `https://ntnuopen.ntnu.no/ntnu-xmlui/handle/11250/2651660` (visited on 03/08/2022).

[19] Sverre Hvidsten and SINTEF Energy Research. *ELK-30 "Condition assessment of high voltage apparatus", Power cables, Partial discharge measurements*.

[20] Hans Kristian Hygen Meyer. *Frekvensinnhold i partielle utladninger i transformatorgjennomføringer*. Apr. 20, 2020.

[21] OMICRON. *How to measure partial discharge*. 2020. URL: `https://www.omicronenergy.com/en /application/offline-testing/partial-discharge-measurement-and-monitoring/` (visited on 01/22/2022).

[22] Guillermo Robles et al. *Antenna Parametrization for the Detection of Partial Discharges*. May 5, 2013. URL: `https://ieeexplore.ieee.org/stamp/stamp.jsp?tp=&arnumber=6338298` (visited on 04/13/2022).

[23] Frenando Garnacho and Javier Ortego. *Application of HFCT and UHF Sensors in On-Line Partial Discharge Measurements for Insulation Diagnosis of High Voltage Equipment*. Apr. 2015. URL: `https://www.researchgate.net/publication/274258611_Application_of_HFCT_and_UHF_Se`

nsors_in_On-Line_Partial_Discharge_Measurements_for_Insulation_Diagnosis_of_High
_Voltage_Equipment (visited on 02/06/2022).

[24] Wojciech Sikorski et al. *On-Line Partial Discharge Monitoring System for Power Transformers Based on the Simultaneous Detection of High Frequency, Ultra-High Frequency, and Acoustic Emission Signals.* June 22, 2020. URL: `https://www.mdpi.com/1996-1073/13/12/3271` (visited on 03/03/2022).

[25] Douglas Aguiar do Nascimento et al. *Evaluation of Partial Discharge Signatures Using Inductive Coupling at On-Site Measuring for Instrument Transformers.* 2018. URL: `https://www.researchgate.net/publication/322549435_Evaluation_of_Partial_Discharge_Signatures_Using_Inductive_Coupling_at_On-Site_Measuring_for_Instrument_Transformers` (visited on 04/21/2022).

[26] Michael Kunicki. *Comparison of capacitive and inductive sensors designed for partial discharges measurements in electrical power apparatus.* 2017. URL: `https://www.researchgate.net/publication/320572151_Comparison_of_capacitive_and_inductive_sensors_designed_for_partial_discharges_measurements_in_electrical_power_apparatus` (visited on 03/05/2022).

[27] Zhong et al. *Use of Capacitive Couplers for Partial Discharge Measurements in Power Cables and Joints.* June 25, 2001. URL: `https://ieeexplore.ieee.org/document/955677` (visited on 02/05/2022).

[28] Y. Tian et al. *Partial Discharge Detection in Cables Using VHF Capacitive Couplers.* Apr. 2003. URL: `https://ieeexplore.ieee.org/document/1194121` (visited on 04/29/2022).

[29] Steven A. Boggs. *Partial Discharge - Part 11: Detection Sensitivity.* 1990. URL: `https://ieeexplore.ieee.org/abstract/document/63081` (visited on 03/22/2022).

[30] J. Havunen and J. Hällström. *Precision Calibration System for Partial Discharge Calibrators.* 2019. URL: `https://www.ntnu.no/ojs/index.php/nordis/article/download/3264/3145/13192` (visited on 05/20/2022).

[31] S.M. Strachen et al. *Knowledge-Based Diagnosis of Partial Discharges in Power Transformers.* Feb. 2008. URL: `https://ieeexplore.ieee.org/document/4446759` (visited on 03/03/2022).

[32] Hans-Petter Halvorsen. *Reguleringsteknikk med LabVIEW og MathScript eksempler.* Oct. 26, 2016. URL: `https://www.halvorsen.blog/documents/automation/resources/Reguleringsteknikk\%20med\%20eksempler.pdf?list=PLdb-TcK6Aqj0qo8bGea_2FOYEUOIBeiXO` (visited on 03/22/2022).

[33] Nexans. *AIN - Indoor slip-on termination, silicone, up to 42 kV.* May 2021. URL: `https://www.nexans.de/.rest/catalog/v1/family/pdf/27625/AIN-Indoor-slip-on-termination-silicone-up-to-42-kV` (visited on 04/20/2022).

[34] Analog Devices. *LtSpice.* 2022. URL: `https://www.analog.com/en/design-center/design-tools-and-calculators/ltspice-simulator.html` (visited on 05/02/2022).

[35] OMICRON. *MPD 600, High-end partial discharge measurement and analysis system.* Mar. 2019. URL: `https://www.omicronenergy.com/en/products/mpd-600/` (visited on 04/21/2022).

[36] ETS LINDGREN. *Current probes, User Manual.* 2008. URL: `https://www.manualshelf.com/manual/ets-lindgren/94606-6-current-probe/instruction-manual-english.html` (visited on 05/06/2022).

[37] *Eaton 93686-1L Injection Probe.* URL: `https://www.emchire.co.uk/product/eaton-936861l-injection-probe--20hz--30mhz-241` (visited on 05/06/2022).

Appendices

A   Equipment

Table A.1 lists the equipment utilised for the laboratory experiments separated into categories according to application. The test object category is the equipment related to the test object used for experiments, while the test circuit category is related to equipment needed to conduct the different experiments. The sensor technology category relates to equipment utilised for the PD measuring techniques, separated into Omicron MPD 600, inductive coupling and capacitive coupling. More details about the PD measuring system provided by Omicron MPD 600 and the HFCT from TEGAM are given in subsection A.1 and subsection A.2 respectively. The generation of void defect lists the equipment utilised to generate an artificial void defect.

Table A.1: *Laboratory equipment categorised according to application.*

Category	Equipment
Test object	12 kV PEX cable
	AIN-slip-on termination, 42 kV
	Silicone grease
	Field control pad
	Field control tape
	Cable peeler
Test circuit	Transformer 230 V/110 kV
	Coupling capacitor 100 pF
	Corona rings
	Variac
	Charge calibrator device
	Coax cables
Sensor technology	Omicron MPD 600
	- PD detector, MPD 600
	- Battery, MPP 600
	- Coupling device, CPL 542
	- Duplex fiber optical cable
	Inductive coupling
	- HFCT, TEGAM 93686-1L
	- Minicircuits 10 x amplifier, 50 ohm, 0.5 - 500 MHz
	Capacitive coupling
	- Copper mesh, copper foil
	- Transformer, 1:1
	- Coil, 10 mH
Generation of void defect	Micro-glass spheres (Micro-glass balloons, Biltema)
	EpoFix Resin
	Liquid silicone rubber, Elastosil LR 3003/60 A/B
	Casting moulds, D = 10 cm, h = 2 mm
	Vacuum chamber
	Heating cabinet

A.1   OMICRON MPD 600

The MPD 600 system is a high-end measurement and analysis system for partial discharges. It can be utilised for many different PD testing applications on electrical equipment. The system enables both single- and multi-channel PD measurements, and all measurement signals are recorded, analysed, and displayed simultaneously. The system also provides advanced noise suppression and source separation techniques which ensure that only PD pulses from the test object are analysed[35].

A challenge when analysing PD is detecting and evaluating discharges in the range of pico-coulombs (pC) while dealing with test voltages of up to several hundred kilovolts (kV). External interference or noise from nearby equipment caused by corona or other radio frequency sources can complicate the measurements. In such cases, the MPD 600 system can be used to provide accurate, reliable, and reproducible measurements[35].

The MPD 600 system setup includes software for PD analysis, a fiber optical bus controller (MCU 520), duplex fiber optical cable, partial discharge detector (MPD 600) and chargeable lithium-ion battery (MPP 600). The MPD 600 is compatible with various accessories. An illustration of the system setup is given in Figure A.1. For conventional detection of PD, an external measuring impedance (CPL 542) is utilised[35].
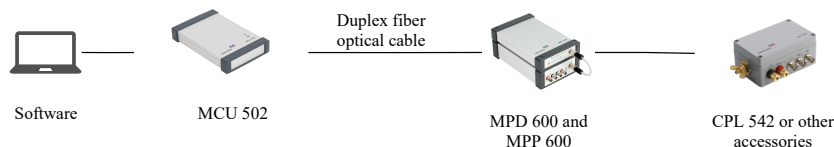
Figure A.1: *The Omicron MPD 600 PD measuring system[35].*

A.2   HFCT sensor, Current probe 93686-1L

TEGAM 93686-1L is a clamp radio frequency transformer that can be used to determine the intensity of radio frequency current present in an electrical conductor or group of conductors. The probe can be used with receiver instrumentation having a 50 Ω input impedance. The sensor has a bandwidth of 20 Hz to 30 MHz[36].
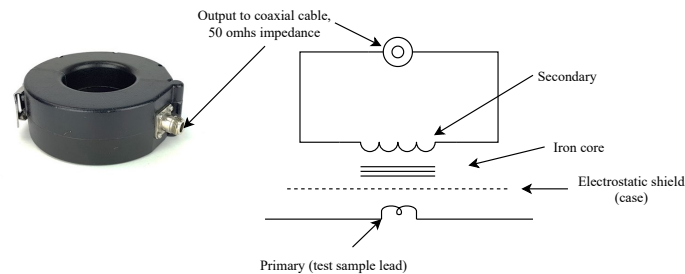
Figure A.2: *Current probe 93686-1L is a radio frequency transformer that can be clamped around a conductor to accurately measure radio frequency current present in the circuit. The circuit of the probe is given to the right.[36, 37]*

The probe provides a way to accurately measure net radio frequency current flowing in a wire or bundle of wires without requiring a direct connection to the conductor(s) of interest. The test object becomes a one-turn primary winding by clamping the probe around it. By doing so, the probe forms the core and secondary winding of a radio frequency transformer. Measurements can be made on single-conductor and multi-conductor cables, grounding and bonding straps, outer conductors of shielding and coaxial cables[36].

B   Calculation of capacitances

The following appendix will describe the procedure of how the cable capacitance, C_{iso}, and the stress cone capacitance, C_{con} was found, utilised for the analysis in LtSpice. Both the cable and the stress cone was assumed to be cylindrical capacitances. A cylindrical capacitance can be modeled as illustrated in Figure B.1 with an outer radius r_y and an inner radius, r_i.
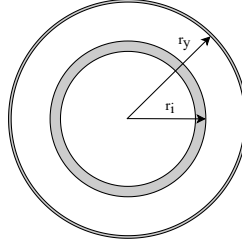
Figure B.1: *The model of a cylindrical capacitance with an outer and inner radius.*

Based on this model the capacitance, C, can be calculated as given in Equation B.1[12].

$$C = \frac{2\pi\varepsilon_r\varepsilon_0 l}{ln\frac{r_y}{r_i}}$$

(B.1)

Table B.1 gives the parameters for both the cable and the stress cone used in the calculations and the resulting capacitances. It is assumed that the stress cone has an uniform thickness of 1 cm. The capacitances are only calculated for the area covered with the copper-mesh electrode which is equal to a length of 6 cm.

Table B.1: *Parameters utilised to calculate the cable and stress cone capacitances with the resulting capacitance value.*

Parameter	Cable insulation	Stress cone
ε_r	2.3	2.9
ε_0	8.85 pF	8.85 pF
r_y	12.4 mm	16.4 mm
r_i	7.5 mm	11.4 mm
l	6 cm	6 cm
C	15.26 pF	26.60 pF

C   Generation of flat air-filled cavity defect

Circular samples with a diameter of 8.5 mm and a thickness of 0.20 mm (before curing) were produced from a resin-rich mica tape containing 45% mica, 43% epoxy resin and 12% glass fibre, by weight percent. Four different test objects were made by pressing three circular samples together with a drilled hole in the middle layer simulating a void. One test object was made with a void diameter, D, equal to 1 mm and one test objects with D equal to 2 mm. The height, d_c, was 0.15 mm (after curing). The samples were cured at 160°C in a heating cabinet under pressure from a 200 g weight for one hour, before being cooled to room temperature. A schematic drawing of the test object with an embedded void is given in Figure C.1. There is a difference in the total thickness of the mica-tape before and after curing.
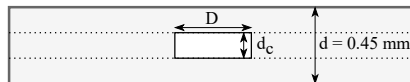
Figure C.1: *Schematic drawing of the cross section of the mica test objects with an embedded void.*

Inception voltage calculations

Simple calculations were performed to calculate the inception voltage of PD in the flat mica cavity. Figure C.2 was used as the basis for calculations, where *HV* and *GND* are the high voltage electrode and the ground electrode respectively, *E* is the electric field in the dielectric material with a relative permittivity, ε_r, of 2.3 of a thickness, *d*, equal to 0.45 mm. The cavity size, d_c, equals 0.15 mm, and the electric field in the cavity is annotated as E'.
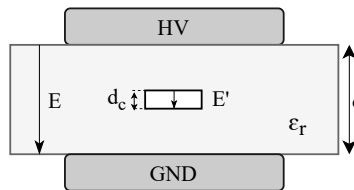
Figure C.2: *Model of a flat air-filled cavity in a dielectric between an electrode configuration.*

Utilising p=1 bar, the Paschen's law approximation given in Equation 2.1 and the relation between *E* and E' in a flat gas-filled cavity, given in Equation 2.3, the calculations given in Table C.1 was obtained.

Table C.1: *Calculations on PDIV for the air-filled flat cavity at a pressure of 1 bar inside the avity.*

Flat air-filled cavity		Unit
p	1	bar
d_c	0.15	mm
E' (From Paschen)	8.15	kV/mm
ε_r	2.30	
d	0.45	mm
E	3.54	kV/mm
$PDIV_{peak}$	**1.59**	**kV**
$PDIV_{rms}$	**1.13**	**kV**

Finished mica-object

Figure C.3 illustrate the finished mica-object with a diameter of the mica-void of 2 mm.

(a) *Finished mica-object*
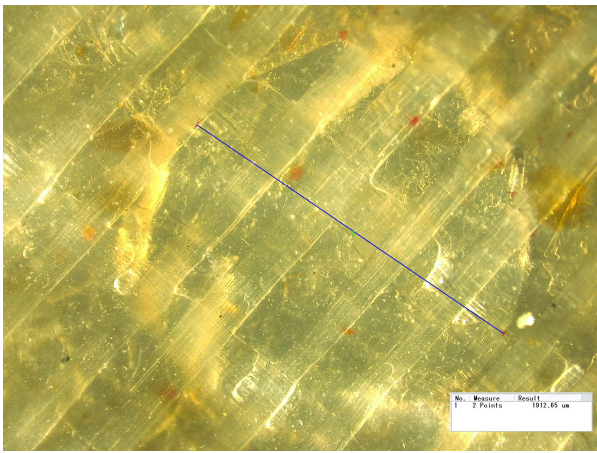
(b) *Inspection by a microscope of the finished mica-object.*

Figure C.3: *The finished mica-object for a flat air-filled cavity.*

D   Silicone rubber casting

The following appendix describes the procedure of casting micro-glass spheres in liquid silicone rubber. Elastosil LR 3003/60 A/B was utilised. The mixing ratio of the silicone rubber is 1:1, and 50 grams of substance A was mixed with 50 grams of substance B. The mixture was sat in a vacuum chamber for approximately one hour to eliminate air trapped inside the silicone rubber. The mixture was then distributed onto four circular moulds with a diameter of 10 cm and a thickness of 2 mm. Twenty grams of the mixture were applied to each mould, and approximately 20 to 40 micro glass balloons were evenly spread into each mould. In addition, two more moulds without micro-glass balloons were cast to have a reference PDIV test. The same procedure was followed to make these moulds.

The moulds were cured in a hydraulic press with heated plates at 165°C, applying low pressure for 20 seconds and high pressure for 9 minutes. The press distributes the silicone rubber evenly in the moulds. The test objects were further cured in an incubator at 200°C for four hours. Moulds with silicone rubber before casting are illustrated in Figure D.1a. PET-film was used in-between to prevent the silicone rubber from sticking to the cast lid. Finished test objects after casting are illustrated in Figure D.1b.
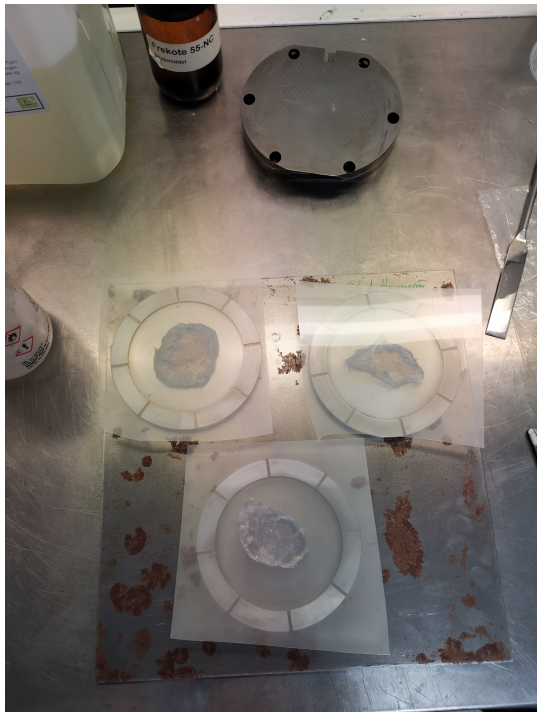
(a) Circular moulds with silicone rubber before casting.
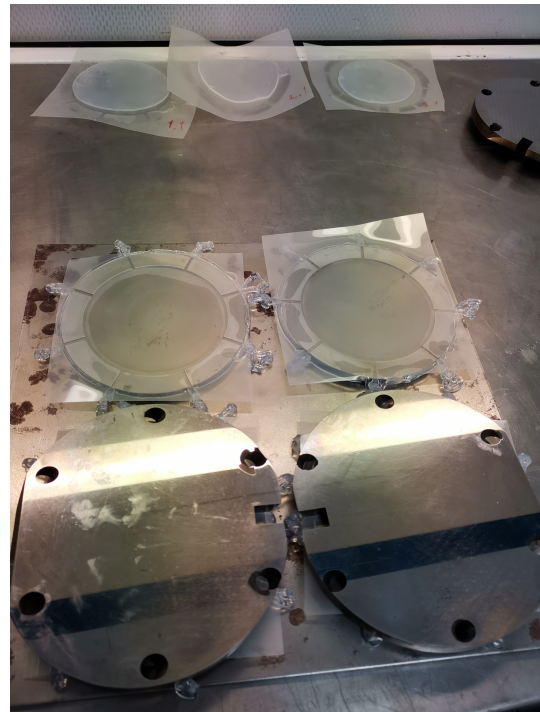
(b) Finished casting.

Figure D.1: Casting procedure of the silicone rubber objects. Micro glass balloons were cast in silicone rubber in circular moulds.

E   Defect implementation evaluation and preliminary attempts

Several techniques to implement the defect into the cable insulation was evaluate. The different techniques are listed below.

1. Drilling a small hole in the slip on cable termination and implement a micro-glass sphere by a glass pole.

2. Cast a micro-glass sphere in epoxy and then implement it into the insulation of the termination,

3. Drilling holes directly into the cable insulation and placing one defect at a time inside the hole and seal with silicone grease.

4. Drilling a hole in the cable insulation and cast one micro-glass sphere in epoxy in the hole.

Procedure 1 could be a good alternative considering that PD could be measured from the actual termination insulation. However, this proposal will likely not work as additional defects and cavities are hard to exclude in the drilled hole. Proposal 2 is a good alternative to having a larger defect object to handle, however, it would require that a relatively large hole had to be drilled into the insulation. Proposals 3 and 4 do not demand a large hole into the insulation. The easiest procedure would be to drill a small hole into the cable insulation, place the defect and seal it with silicone grease or epoxy. However, precautions must be taken to prevent air bubbles from forming in the sealing process.

Both proposals 3 and 4 were tested on a cable specimen. The silicone grease and epoxy were vacuumed before being applied to the hole with the micro-glass sphere. For the epoxy casting, EpoFix Resin was used. This low viscosity epoxy cold mounting system cures at room temperature in about 12 hours. It has no shrinkage, which is beneficial for avoiding gaps between the insulation and the epoxy. The test sample was examined under a microscope to see how the sealing turned out. The result for both the silicone sample and the epoxy sample can be seen in Figure E.1. Both the silicone and epoxy test are victims of air bubbles trapped inside the material.

(a) *Silicone*   **(b)** *Epoxy*

Figure E.1: *Attempts on defect implementation. One micro-glass sphere were placed in the hole in the cable insulation and sealed with silicone grease and epoxy-resin. Additional air bubbles are hard to avoid which these two tests are clear examples on.*

It was decided to continue with the epoxy casting to provide more control of the micro-glass sphere when fitting the stress cone back in place. As the stress cone is fastened tightly around the cable, movement of the sphere could happen due to stress-cone refitting if the insulation hole was sealed with silicone grease.

Excavations of a diameter of 1 to 3 mm were drilled 0.5 mm into the insulation of a test cable specimen. One micro-glass sphere was cast in epoxy in each of the holes. These attempts aimed to create a hole in the insulation with a small as possible impact on the cable insulation while simultaneously having control of the micro-glass sphere. Preferably, the hole should be as small as possible, but the smaller the hole, the harder it is to control both the epoxy and the micro-glass sphere.

Figure E.2 illustrate the attempt of casting one micro-glass sphere into the hole of D=1 mm. As can be seen the epoxy has filled the hole in the insulation, but an excavation have formed during the curing process.

(a) *1 mm*   **(b)** *Excavation in the epoxy.*

Figure E.2: *Attempts on defect implementation. One micro-glass sphere were placed in a 1 mm hole 0.5 mm into the cable insulation and sealed with epoxy-resin.*

For the hole of a diameter of 2 mm, as can be seen in Figure E.3 the hole is completely filled with epoxy, and the micro-glass sphere is completely submerged. However, small gas bubbles have formed on the surface of the epoxy. These gas bubbles are, however, much smaller than the micro-glass sphere and are assumed to have a higher PDIV than the sphere.
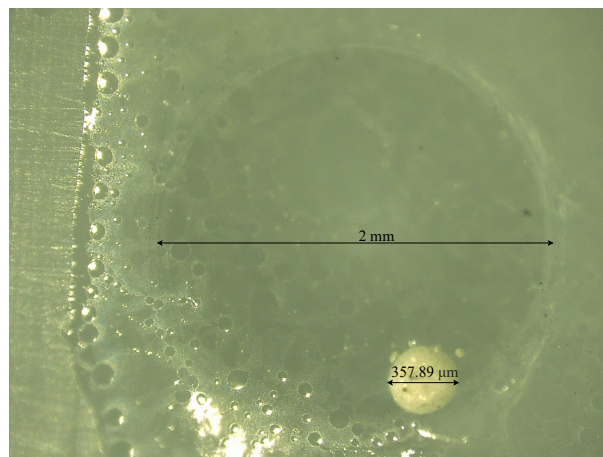
Figure E.3: *Attempts on defect implementation. One micro-glass sphere were placed in a 2 mm hole 0.5 mm into the cable insulation and sealed with epoxy-resin. Air bubbles have formed on the surface of the epoxy-resin.*

In the cast where the diameter of the hole was 3 mm, additional gas bubbles have formed. This can be seen in Figure E.4.
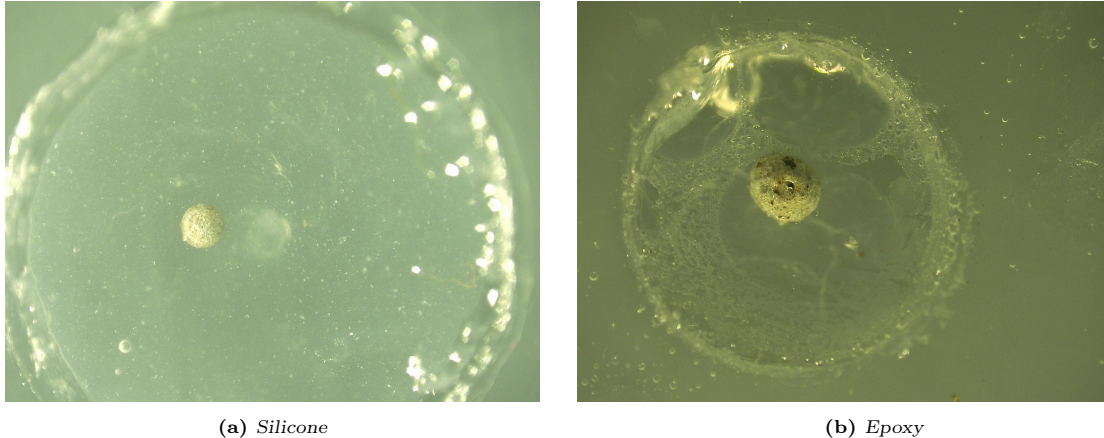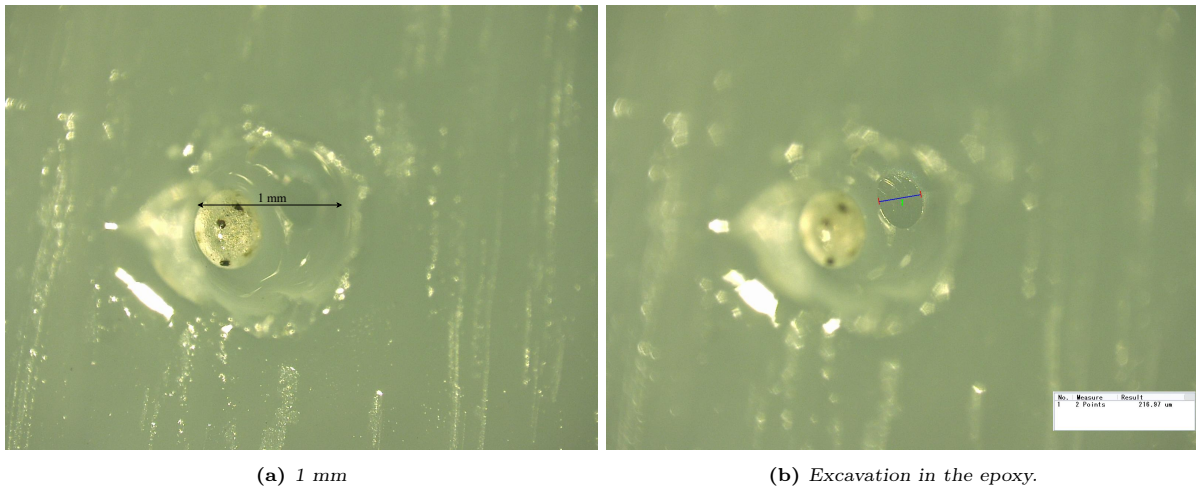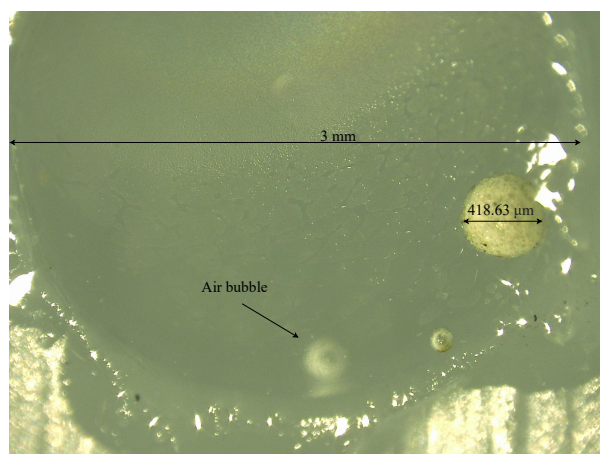
Figure E.4: *Attempts on defect implementation. One micro-glass sphere were placed in a 3 mm hole 0.5 mm into the cable insulation and sealed with epoxy-resin. One additional micro-glass sphere have by accident been cast into the epoxy. In addition, an air bubble have formed in the*

For the actual defect implementation it was decided to continue with a hole in the cable insulation of 2 mm. A hole of this size provided acceptable control of the epoxy and the placement of the micro-glass sphere.

F   Dimensions slip-on stress cone

Figure F.1: *Dimensions of the 3D model of the stress cone in Comsol.*

G   Test parameters and PRPD plots for the silicone rubber tests

The test results from the PDIV test of the silicone rubber objects with micro glass balloons can be seen in Table G.1. This includes the purpose of the test, PD threshold, bandwidth and resulting PDIV. Details about the reference test conducted ahead of the PDIV tests of the micro-glass balloons are included. The reference test uncovered some noise up to 4 pC, and it was therefore decided to increase the PD threshold to 3 pC when performing the PDIV tests.

Table G.1: *PDIV test results for micro glass balloons cast in silicone rubber molds.*

Test object	Purpose	$PD_{threshold}[pC]$	f_c [kHz]	Δf [kHz]	$PDIV_{rms}$ [V]
Ref	Reference	2	400	650	-
1	PDIV	3	400	650	5437.88
2	PDIV	3	400	650	4662.83
3	PDIV	3	400	650	8604.22
4	PDIV	3	400	650	6368.64

Figure G.1 illustrate the PD-test for the reference object of silicone rubber at 15.25 kV recorded for almost 5 minutes. As can be seen, a symmetrical pattern of discharges has emerged in the rising part of the AC voltage both in the negative and positive half cycle. It is assumed that these discharges are owing to background noise. Some individual discharges have also emerged near the peak of the voltage.

Figure G.1: *PRPD plot of the reference silicone rubber mold.*

The resulting PRPD plots of the four silicone rubber test objects can be seen in Figure G.2. The PRPD plots are generated around the PDIV for the different test objects. As the purpose of this test was to measure the PDIV, the sampling time for the PRPD plots varies according to the test object. Symmetrical patterns have emerged around the zero crossing of the voltage for each test, typical phase position of cavity defects.

(a) *Test object 1*

(b) *Test object 2*

(c) *Test object 3*

(d) *Test object 4*

Figure G.2: *PRPD patterns for the silicone rubber tests.*

H   Calculations of expected PDIV

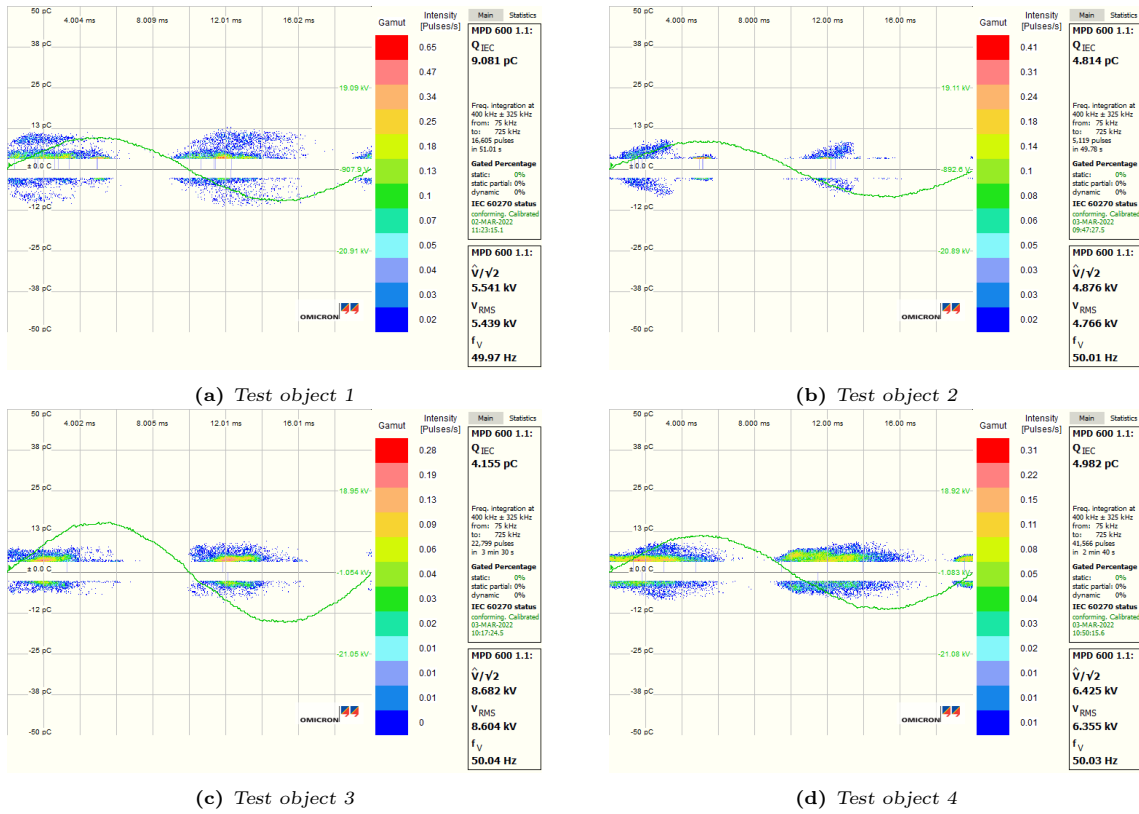The silicone rubber tests resulted in a mean PDIV of 6.27 kV_{rms}. This corresponds to a a PDIV peak value of 8.87 kV. The field inside the silicone rubber object can be calculated as given in Equation H.1.

$$E = \frac{PDIV_{peak}}{d} = \frac{8.87[kV]}{2[mm]} = 4.44[kV/mm] \tag{H.1}$$

The breakdown field of the micro-glass spheres, E', can be calculated as given in Equation H.2, where ε_r correspond to the relative permittivity of silicone rubber, equal to 2.8.

$$E' = \frac{3\varepsilon_r}{1 + 2\varepsilon_r} \cdot E = \frac{3 \cdot 2.8}{1 + 2 \cdot 2.8} \cdot 4.44[kv/mm] = 5.64[kV/mm] \tag{H.2}$$

Assuming that this field is the breakdown field of the micro-glass spheres, needed for PD inception, the field inside the cable can be calculated. On the basis of an ε_r of PEX equal to 2.3 the field inside the cable, E_{cable}, can be calculated as given in

$$E_{cable} = \frac{1 + 2\varepsilon_{r,PEX}}{3\varepsilon_{r,PEX}} \cdot E' = \frac{1 + 2 \cdot 2.3}{3 \cdot 2.3} \cdot 5.64[kV/mm] = 4.58[kV/mm] \tag{H.3}$$

The voltage that needs to be applied to the cable to obtain this field can be calculated on the basis of E_{cable} assuming a cylindrical conductor, where $r = r_y$. This is given in Equation H.4.

$$U = E_{cable} \cdot r_y \cdot \ln \frac{r_y}{r_i} = 2.3 \cdot 11.4[mm] \cdot 7.5[mm] \cdot \ln \frac{11.4[mm]}{7.5[mm]} = 21.86[kV] = \underline{15.46[kV_{rms}]} \tag{H.4}$$

Based on these calculations it can be expected a PDIV of the micro-glass sphere inside the cable insulation of 15.46 [kV_{rms}]. The results are summarised in Table H.1.

Table H.1: *Summarised results of the expected PDIV calculations.*

	PDIV	PDIV$_{peak}$	E	E'
	kV$_{rms}$	kV	kV/mm	kV/mm
Silicone rubber	6.27	8.86	4.44	5.64
XLPE	15.46	21.86	4.58	5.64

I Analysis data and PRPD plots for PD sensor testing

I.1 Corona defect

Table I.1 gives the PD threshold, bandwidth, mean pulse repetition rate and voltage used for the pulse repetition rate analysis for the corona defect. The table is divided according to test number and which type of measuring technique is utilised.

Table I.1: *PD threshold, bandwidth, mean pulse repetition rate and voltage in the sampling interval for corona discharges for the conventional measuring technique and the copper mesh sensor.*

Test	Measuring tech.	PD threshold [pC]	Bandwidth f_c	Δf	Mean pulse repetition rate [$pulses/s$]	Voltage [kV_{rms}]
1	Conventional	10	400 kHz	650 kHz	1346.76	
	Copper mesh	10	4 MHz	1.5 MHz	527.29	∼ 3.50
2	Conventional	5	400 kHz	650 kHz	20715.80	
	Copper mesh	5	4 MHz	1.5 MHz	2915.79	∼ 3.73

PRPD plots for the two corona tests for both the conventional measuring technique and the copper mesh sensor can be seen in Figure I.1.

(a) *Test 1 - conventional*

(b) *Test 1 - copper mesh*

(c) *Test 2 - conventional*
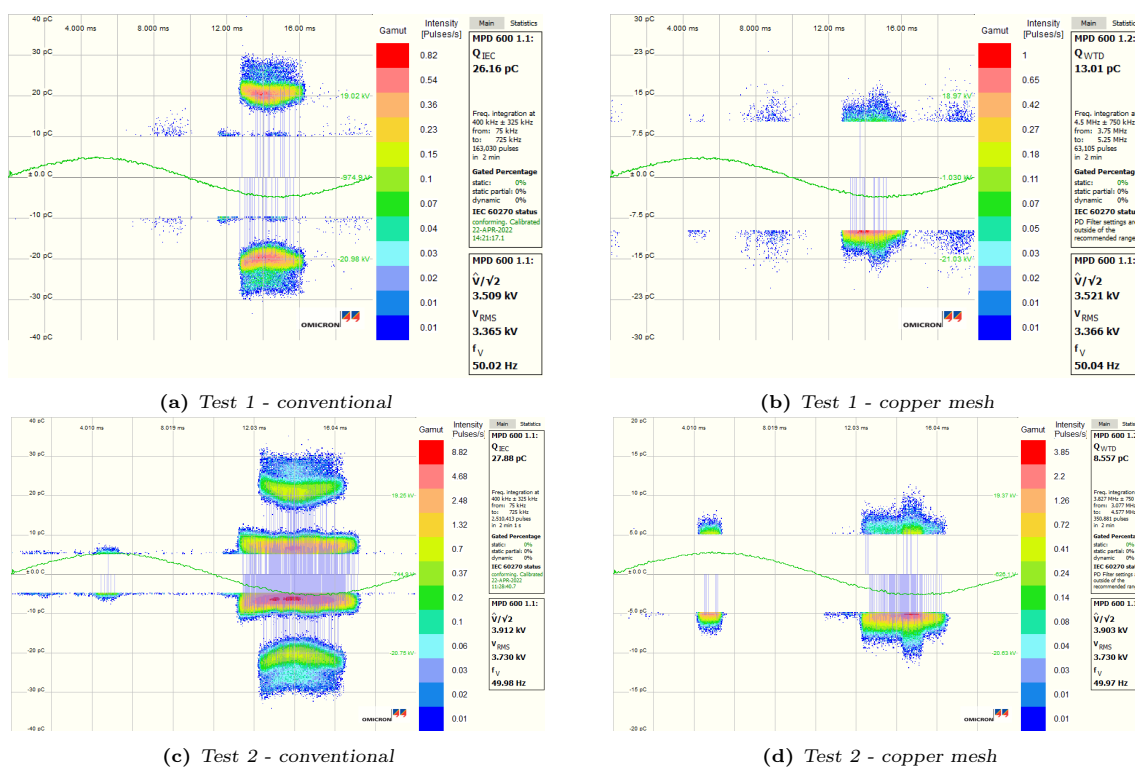

(d) *Test 2 - copper mesh*

Figure I.1: *PRPD plots for the two corona-discharge tests.*

I.2 Void defect

Table I.2 gives the PD threshold, bandwidth, mean pulse repetition rate and voltage used for the pulse repetition rate analysis. The table is divided according to test number and which type of measuring technique is used. The sat PD threshold is increased to 20 pC for the copper mesh sensor at test number 2 to filter noise high noise signals that occurred during that test.

Table I.2: *PD threshold, bandwidth, mean pulse repetition rate and voltage in the sampling interval for void discharges for the conventional measuring technique and the copper mesh sensor.*

Test	Measuring tech.	PD threshold [pC]	Bandwidth f_c	Δf	Mean pulse repetition rate [pulses/s]	Voltage [kV$_{rms}$]
1	Conventional	4	400 kHz	650 kHz	405.80	
	Copper mesh	15	4 MHz	1.5 MHz	431.85	∼ 7.50
2	Conventional	4	400 kHz	650 kHz	942.23	
	Copper mesh	20	4 MHz	1.5 MHz	944.80	∼ 7.10
3	Conventional	4	400 kHz	650 kHz	607.12	
	Copper mesh	15	4 MHz	1.5 MHz	635.50	∼ 7.00
4	Conventional	4	400 kHz	650 kHz	2561.97	
	Copper mesh	15	4 MHz	1.5 MHz	2562.21	∼ 7.50

Figure I.2 illustrates the PRPD plots for all four void-discharge sensor tests. The PRPD plots are generated by sampling the discharges for six minutes at 7 to 7.5 kV. The PRPD plots are sorted according test number, where one row corresponds to one test.
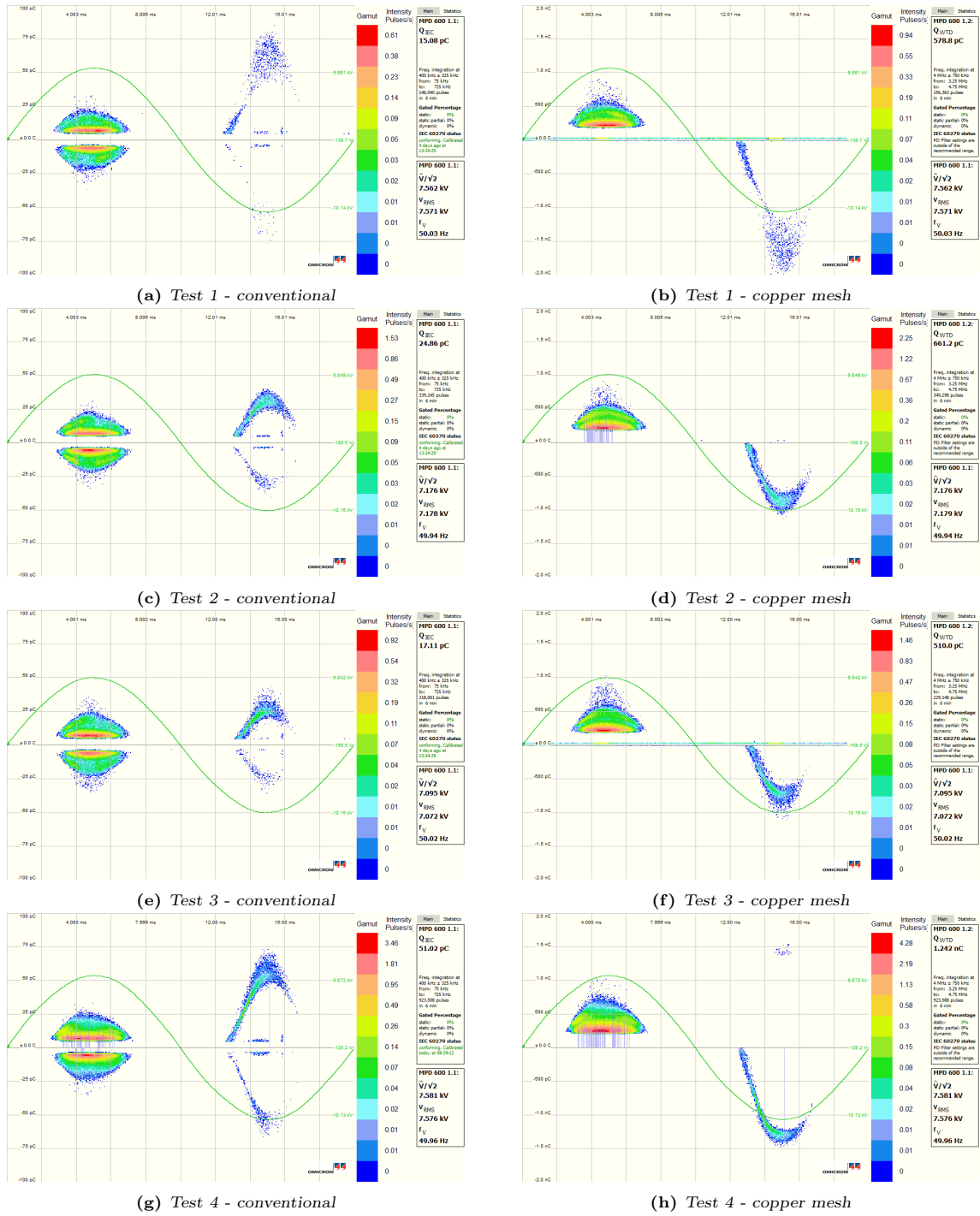
(a) *Test 1 - conventional*

(b) *Test 1 - copper mesh*

(c) *Test 2 - conventional*

(d) *Test 2 - copper mesh*

(e) *Test 3 - conventional*

(f) *Test 3 - copper mesh*

(g) *Test 4 - conventional*

(h) *Test 4 - copper mesh*

Figure I.2: *PRPD plots for the 4 void-discharge tests.*